

Kondo physics and thermodynamics of the Anderson impurity model by distributional exact diagonalization

Dissertation

zur Erlangung des Doktorgrades der Naturwissenschaften
(Dr. rer. nat.)

der

Naturwissenschaftlichen Fakultät II
Chemie, Physik und Mathematik

der Martin-Luther-Universität
Halle-Wittenberg

vorgelegt von

Frau Sareh Motahari
geb. am 11.06.1982 in Saveh (Iran)

Datum der Verteidigung:

04.08.2017

Gutachter:

Prof. Dr. E. K. U. Gross (Betreuer), Prof. Dr. Jamal Berakdar, Prof. Dr. Stefan Kurth

Contents

1	Introduction	5
2	Background	9
2.1	Kondo effect and Anderson impurity model	9
2.2	Green's function	12
2.2.1	Lehmann representation	14
2.2.2	Spectral density	15
2.3	Green's function for the Anderson model	15
2.4	Local moment formation in the Hartree-Fock Approximation	17
3	Method	21
3.1	Exact Diagonalization	21
3.1.1	Two-site Anderson model	22
3.1.2	Some implementation details of the exact diagonalization procedure	25
3.2	The distributional exact diagonalization Algorithm	27
3.3	Role of the constraint	29
4	Zero temperature results	35
4.1	Symmetric Anderson model	35
4.2	Asymmetric Anderson model	37
4.3	Σ_0 determination	41
4.4	DED statistics	42
5	DED for finite temperatures	44
5.1	Straightforward generalization to finite temperatures	44
5.2	Relaxation of the constraint	48
5.3	Finite temperature results	51
5.4	Discussion	53
6	Towards multi-orbital Kondo physics in real systems	56
6.1	The two-orbital Anderson model	56
6.2	DED for the multi-orbital model	57
6.3	Two-orbital Anderson model without Hund's rule coupling	59
6.4	Two-orbital Anderson model with Hund's rule coupling: the fully screened case	62
6.5	Two-orbital Anderson model with Hund's rule coupling: the underscreened case	65
6.6	Discussion	66
7	Conclusions and perspectives	68
A	Derivation of Hund's rule coupling	70

Abbreviations

DED	Distributional Exact Diagonalization
NRG	Numerical Renormalization Group
AIM	Anderson Impurity Model
DMFT	Dynamical Mean Field Theory
NCA	Non-Crossing Approximation
OCA	One-Crossing Approximation
ED	Exact Diagonalization
CTQMC	Continuous-time Quantum Monte Carlo
GF	Green's Function
HF	Hartree Fock
ph	particle hole
QP	Quasi Particle
tot	total
acc	accepted
ENS	Ensemble average
FSR	Friedel's Sum Rule
DOS	Density Of States
imp	impurity

1 Introduction

In solid state physics the physical properties of numerous materials, such as simple metals, some semiconductors and insulators can be explained easily in terms of an effective single non-interacting electrons. But materials with open d and f shells have properties that are harder to explain. In these materials, e.g. transition metals such as vanadium, iron, and their oxides, rare-earth and actinide elements, electrons occupy narrow orbitals. Due to the confinement of the electrons in these narrow d or f orbitals, electrons feel strong Coulombic repulsion (for review see¹⁻³). The small size of the d and f orbitals enhance interaction effects and decrease overlap with other orbitals, which is why the interactions are strong. This category of materials known as strongly correlated materials have the common feature that the electron-electron interaction is comparable to or larger than the kinetic energy.³ The interplay of the d and f electrons internal degrees of freedom—spin, charge, and orbital moment—can exhibit exotic ordering phenomena at low temperatures. This interplay makes strongly correlated electron systems extremely sensitive to small changes in external parameters, such as temperature, pressure, or doping.^{1,4} A wide variety of interesting phenomena can be attributed to electronic correlations, among them high-temperature superconductors,⁵⁻⁷ Kondo effect,^{8,9} and heavy-fermions.¹⁰

The discovery of a new type of copper-oxide based superconducting material, known as cuprates, by Bednorz and Müller in 1986,¹¹ with much higher transition temperatures T_c of $38K$ than normal superconductors (around $10K$), stimulated further research to find novel superconducting materials with high T_c 's.¹² The research in high- T_c superconductors has led to novel materials such as the pnictides with transition temperatures above $130K$.¹³ A common property of these novel high- T_c superconductors are the presence of strong electronic correlations due to partially filled d-bands.⁵⁻⁷ Although the exact mechanisms leading to high- T_c superconductivity are still a matter of debate, and may actually be quite different depending on the type of material, it has been argued that the strong correlations in the cuprates result in an effective electronic attraction, which is required in order to obtain superconductivity.^{12,14} The hope is that a detailed understanding of the mechanisms that lead to high- T_c superconductivity might lead to novel superconducting materials with even higher T_c 's.

Kondo's¹⁵ explanation of the logarithmic anomaly in the electrical resistivity of the diluted transition metal alloys based on the s-d exchange model, caused a great interest in investigation of the Kondo effect problem.¹⁶ A well-known many-body phenomenon, the Kondo effect, arises when a local magnetic moment is weakly coupled to a sea of non-interacting conduction electrons. Such a situation can be realized for example by a transition metal impurity in a metal host where the strongly interacting electrons within the open d- or f-shell of the impurity give rise to the formation of a local magnetic moment. Below a characteristic temperature, so-called Kondo temperature T_k , due to the formation of the unusual Kondo state,¹⁶ the magnetic moment of the impurity is quenched.

Opposed to the previous experiments where the Kondo effect had been observed merely in bulk systems of magnetic impurities embedded in metals,^{17,18} in 1998, Golhaber-Gordon *et al.* announced the observation of conductance signatures of the Kondo effect in a single-electron transistor.¹⁹ This was the first time that the Kondo effect was observed in a single, tunable quantum impurity. The manifestation of quantum dots systems with the impressive control and tunability possible for artificial atoms has generated a source of interest in Kondo and related nanoscale devices.²⁰ In this case, the physics of a quantum dot connected to leads becomes similar to the physics of magnetic impurities

coupled to the conduction electrons in a metal host, the Kondo effect.^{21–23} The Kondo effect reached molecular systems as well. Electronic transport through break junction systems with molecules has been measured.^{24,25}

The Kondo effect also plays an important role in a number of 4f and 5f compounds. Some of them i.e. heavy-fermion systems, Kondo lattices, exhibit anomalous electronic and magnetic properties.¹⁶ Heavy-fermion behaviour for the first time was observed in $CeAl_3$,²⁶ which revealed enormous magnitude of the linear specific heat term ($\gamma = 1.6 JK^{-2} mol^{-1}$).¹⁰ Generally, these materials are Ce and U based metallic compounds which show a strongly enhanced γ -coefficient of the specific heat.²⁷ Since γ is proportional to the effective mass in a simple effective Fermi-liquid theory, the name heavy fermions was assigned to this material class.²⁷ The huge intra-atomic Coulomb repulsion, makes the double occupancy of the 4f shells strictly prohibited, which implies that the state of motion of a given charge carrier completely depends on that of all the others. It is for this reason that such systems are frequently termed strongly correlated electron systems.¹⁰

According to all of these properties, the perspective of the investigation of the strongly correlated materials is very exciting. But as these phenomena are driven by a strong local interaction U , hence they are theoretically complicated to study. Perturbation theory breaks down and as each single electron has a complex influence on its neighbors, it cannot be treated independently, either. Moreover, one can no longer consider any electron in these material as being in a sea of the averaged motion of the others as in mean field theories. Since these materials consist of electrons that are neither fully itinerant which can be described as Bloch waves in the crystal nor, fully localized on their atomic sites, modeling is complicated as well. The dual particle–wave character of the electron forces the adoption of components of the real-space and momentum- space pictures.¹

Traditionally, the Hamiltonian is simplified to take into account only a few relevant degrees of freedom.¹ One of the simplest models that captures the essence of strongly correlated electrons in a solid, is the Hubbard Hamiltonian which was introduced in 1963.²⁸ Despite of its simplicity it cannot be solved exactly for more than $1D$.²⁹ Several method have been applied to calculate the ground state of the Hubbard Hamiltonian. An approximation to the ground state wave function of the Hamiltonian was given by Gutzwiller.³⁰ It is interesting that the Gutzwiller wave function together with the Gutzwiller approximation turns out to be a mean-field solution of the Hubbard Hamiltonian, if we write the latter in terms of so-called slave bosons.¹² Auxiliary fields like slave bosons were originally introduced to replace the two-particle Coulomb interaction term in the Hamiltonian by one bilinear in the field operators.¹²

The advent of the Dynamical mean field theory (DMFT)^{31–34} was a breakthrough in the understanding of strongly correlated materials. DMFT replaces the problem of many interacting electrons on a lattice, with a correlated impurity coupled to a bath of non-interacting electrons. The impurity self-energy is then determined via a self-consistent iterative procedure. Correlations between electrons on different atoms are small and hence can be neglected. Hence the main computational task in DMFT lies in the solution of the quantum impurity model.³⁵

Hence, the Anderson impurity model (AIM)³⁶ is one of the most important models, as it plays a central role in the understanding of the Kondo effect, as well as in DMFT. Although the AIM looks simple its solution is not trivial. For a single impurity, the model can be very efficiently treated using Wilson’s numerical renormalization group (NRG).³⁷ Since the numerical effort of NRG calculations

risers exponentially with the number of impurities, generically it is computationally very demanding and cannot be applied to systems with more than two impurities. In addition, it is unable to make use of the strongest form of parallelization.

A number of approximate methods for solving the Anderson model exists as well. The Non-Crossing Approximation (NCA)^{38,39} and One-Crossing Approximation (OCA),^{40,41} for example, consist in a diagrammatic expansion around the atomic limit, summing only a subset of diagrams to infinite order. Both NCA and OCA yield qualitatively correct spectra for not too low temperatures. While the simpler NCA strongly underestimates the width of the Kondo peak, the vertex corrections within OCA lead to a quantitatively correct estimate of the Kondo scale. At lower temperatures, both NCA and OCA show spurious non-Fermi liquid behavior, leading to artifacts in the spectra.^{42,43} Many other approximate schemes for solving the AIM exist,⁴⁴⁻⁴⁸ though all are burdened with some kind of limitation.

For multi-band materials and clusters involving several atoms the often used and versatile approaches are the Continuous-time Quantum Monte Carlo (CTQMC) algorithm,⁴⁹ and Exact diagonalization (ED).^{50,51} CTQMC can be viewed as another numerically exact method which can be parallelized efficiently, but the analytic continuation of the imaginary-time data to real frequencies leading to artifacts in the spectra. Another serious drawback of CTQMC is its restriction to relatively high temperatures, making this approach of limited use for the study of low-temperature phenomena such as the Kondo effect.

Conversely to the most approximation schemes which the solution to the infinite AIM consisting of an impurity level coupled to an infinite and continuous bath representing a conduction electron band, the key idea in ED is to discretize the continuum of the infinite conduction electron bath via a finite set of bath levels.³⁵ By replacing the infinite AIM by a finite one, which can be solved by exact diagonalization. Finite temperature ED combined with DMFT provides accurate results for various system properties but due to the rapid growth of the Hilbert space the size of the finite bath representing the infinite lattice is severely limited.³⁵ Due to the discrete nature of the conduction electron bath, ED faces with some artifacts in the spectral functions especially in the Kondo regime. In the zero bandwidth limit (one bath level at the Fermi energy) a precursor of the Kondo peak appears in the form of two strongly renormalized delta-peaks close to the Fermi level.⁸ Different strategies for improving direct diagonalization methods have been proposed recently. In one, a careful selection of basis states makes it possible to include a large number of bath levels.⁵² In another, the parameters of an effective finite Anderson model are variationally optimized.⁵³

Here, we focus on a novel method for solving the AIM which has been proposed by Granath and Strand, the Distributional Exact Diagonalization (DED) approach.⁵⁴ A big advantage of DED is that it overcomes the problem of discretization artifacts in ED. Another privilege of DED is that the energy resolution is the same on all energy scales, so that it can be exploited to resolve higher energy spectral features which would be difficult to resolve it with NRG.⁵⁵ In addition it is ideal for the large-scale parallelization. DED maps the infinite Anderson model onto an *ensemble* of finite Anderson models instead of a single effective finite Anderson model. The ensemble average of the self-energies of the finite Anderson models provides a smooth approximation to the self-energy of the original infinite Anderson model that is also free of finite-size artifacts.

This thesis is organized as follows: First, in Sec. 2, we review the Anderson impurity model and the theoretical background of the Kondo effect and the local moment formation. In Sec. 3, the

exact diagonalization is explained, then the DED approach as originally proposed by Granath and Strand is reviewed in detail. In addition, we elucidate the crucial role played by the constraint. In Sec. 4 we present the DED results which show an excellent description of the Anderson model inside and outside the Kondo regime, except for very strong correlations. The DED results further indicate that already for a very small number of 1-2 bath sites, the spectra are in good qualitative agreement with exact spectra calculated by NRG while for a moderate number of 5-7 bath sites the agreement becomes excellent. In order to generalize the DED approach to finite temperature situations, in Sec. 5 first we explain that the constraint should be relaxed in some way in order to achieve the correct impurity entropy (in comparison with NRG). Then, we propose a Boltzmann factor associated with an energy scale required to break the Kondo singlet. At the end of this chapter we calculate the impurity contribution to the entropy, and then we present the corresponding finite temperature results. In Sec. 6 we generalize DED to the case of multi-orbital Anderson models, in particular we discuss more that the constraint should be adapted to the multi-orbital case. Finally, in Sec. 7 we conclude the work with a discussion of the results and a perspective on using DED for more general types of Anderson impurity models.

2 Background

2.1 Kondo effect and Anderson impurity model

When a magnetic impurity is inserted in a nonmagnetic metal, it can give rise to a local moment if an electronic state on the impurity is singly occupied at least on the time scale of the experiment. Such a situation can be realized for example by a transition metal impurity with an open d or f shell in a metal host. Friedel⁵⁶ was the first to introduce a phenomenological model to explain the onset of local moments.⁵⁷ A local magnetic moment can form, however, in a bound or resonant state of the impurity potential near the Fermi level if the levels corresponding to up and down spins are non-degenerate.⁵⁷ He proposed that electrons scattering off transition metal atoms form virtual bound-state resonances.⁵⁸ Before Friedel, back in the 1940s, it had been argued by Rudolph Peierls and Neville Mott that a sufficiently strong Coulomb repulsion would block the passage of electrons.⁵⁸ Ultimately, in 1961 Anderson³⁶ combined the mentioned ideas and reinterpreted Friedel's idea of resonance formation in terms of a tunneling process between d or f orbitals and the metallic band. The single impurity Anderson model (AIM) is:

$$H = \epsilon_d n_d + U n_{d\uparrow} n_{d\downarrow} + \sum_{\sigma,k} \epsilon_k c_{k\sigma}^\dagger c_{k\sigma} + \sum_{\sigma,k} V_k (d_\sigma^\dagger c_{k\sigma} + c_{k\sigma}^\dagger d_\sigma) \quad (1)$$

with ϵ_d the bare energy cost for an electron to reside in the impurity with spin either up or down, d_σ (d_σ^\dagger) the annihilation (creation) operator for the impurity level d and spin σ , $c_{k\sigma}$ ($c_{k\sigma}^\dagger$), the annihilation (creation) operators for k states of the metallic band and spin σ , $n_{d\sigma} = d_\sigma^\dagger d_\sigma$, $n_d = \sum_\sigma n_{d\sigma}$, U the on-site Coulomb repulsion at the impurity and V_k the coupling between the impurity level d and conduction electron k .

In this model the metallic host, also often called bath, has a conduction band, which can be described by Bloch states, $|k\rangle$ with some energy dispersion ϵ_k . The impurity ion has only one state, which is spin-degenerate with energy dispersion ϵ_d . The impurity orbital can be either singly, or doubly occupied by two electrons of opposite spins. The crucial input, the correlation between electrons on the impurity ion, $U n_{d\uparrow} n_{d\downarrow}$, which is typically strong in the narrow d shell, has the effect of favoring single occupation of the impurity level. This term, which physically arises from the Coulomb repulsion between the electrons, turns out to be essential for the formation of a magnetic moment on the localized orbital. Note that the states forming the conduction band are usually s-type which are more expanded in space, so that interactions are less important for those. The final ingredient in the Anderson model is a spin-conserving coupling between the impurity level and the k states of the metallic band. The overlap of the d orbital and the conduction band leads to a hybridization between the d orbital with the Bloch waves of the conduction band and causes non-diagonal matrix elements of the Hamiltonian.

In order to understand how local moments come into existence, we consider the Anderson model in the atomic limit where an isolated impurity is described by:

$$H_{atomic} = \epsilon_d n_d + U n_{d\uparrow} n_{d\downarrow} \quad (2)$$

The four possible quantum states are:

$$\begin{aligned}
|\uparrow\downarrow\rangle \quad E(d^2) &= 2\epsilon_d + U \\
|0\rangle \quad E(d^0) &= 0 \\
|\uparrow\rangle, |\downarrow\rangle \quad E(d^1) &= \epsilon_d
\end{aligned} \tag{3}$$

The first two are non-magnetic, while the last two are magnetic. For ϵ_d negative and $U > |\epsilon_d|$, the ground state is a two-fold degenerate magnetic doublet. Inasmuch as only the spin degrees of freedom remain, the system behaves as a *local moment*. Adding or removing an electron from the magnetic ground state costs an energy of $\epsilon_d + U$ and $-\epsilon_d$, respectively, so that there are two resonances in the spectral density corresponding to the addition and removal energies $\epsilon_d + U$ and ϵ_d . When $\epsilon_d = -U/2$ the excitations are at $+U/2$ and $-U/2$. This is known as the symmetric Anderson model or the particle-hole symmetric regime.

Due to the coupling to the conduction band, the impurity level acquires some broadening Γ (a more detailed description will be given in Sec.2.3). In case of weak coupling, $\Gamma \ll |\epsilon_d - \epsilon_F|$ and $\Gamma \ll |\epsilon_d + U - \epsilon_F|$, the cost of doubly occupying the impurity level is much higher than the impurity energy ϵ_d and the broadening Γ . Generally it is assumed that the impurity level lies below the Fermi energy, $\epsilon_d < 0$. This state will be at least singly occupied. To put another electron on the impurity, the cost of $\epsilon_d + U$ is needed. So the cost of putting two electrons on the impurity level is $2\epsilon_d + U$. This energy $2\epsilon_d + U$ is far above the Fermi level. So the impurity level stays singly occupied and the Anderson model supports the formation of local moments.

Now, when a local magnetic moment forms, the weak coupling to a sea of non-interacting conduction electrons may induce the Kondo effect, named after the Japanese physicist Jun Kondo.¹⁵ At low temperatures the effective coupling between the magnetic moment and the conduction electrons becomes antiferromagnetic leading to the formation of a total singlet state $S = 0$.

To establish the origin of the antiferromagnetic interaction between the local moment and the conduction electrons, first we consider the Kondo model. The Kondo Hamiltonian describes the interaction of impurity spins, assumed to be $1/2$, with the spins of conduction electrons. The Kondo Hamiltonian with a band of mobile electrons is:

$$H_K = \sum_{k,\sigma} \epsilon_k n_{k\sigma} - \sum_{k,k'} J_{kk'} (\Psi_{k'}^\dagger S \Psi_k) \cdot (\Psi_d^\dagger S \Psi_d) \tag{4}$$

The interaction $J_{kk'}$ is the analog of the Heisenberg spin exchange interaction between the spin of a band electron and that of a localized electron.⁵⁷ A positive $J_{kk'}$ favors spin parallel alignment and thus describes a ferromagnetic coupling, while a negative $J_{kk'}$ favors antiparallel spin alignment and thus describes an antiferromagnetic coupling.

In the next step, we focus on the scattering of a conduction electron with a local moment, in the Anderson model. To do so, a simple Anderson impurity model including a single impurity level d plus a single conduction level k is considered. Now the weak coupling is considered as a perturbation to the rest of the Hamiltonian. More precisely, the unperturbed part without coupling to the bath is $H_0 = \epsilon_d n_d + U n_{d\uparrow} n_{d\downarrow} + \sum_{\sigma} \epsilon_k c_{k\sigma}^\dagger c_{k\sigma}$, while $H_1 = \sum_{\sigma} V_k (d_{\sigma}^\dagger c_{k\sigma} + c_{k\sigma}^\dagger d_{\sigma})$, which describes the coupling between impurity and the bath, is treated as a perturbation to the Hamiltonian. Hence the energy expression up to second order is given by

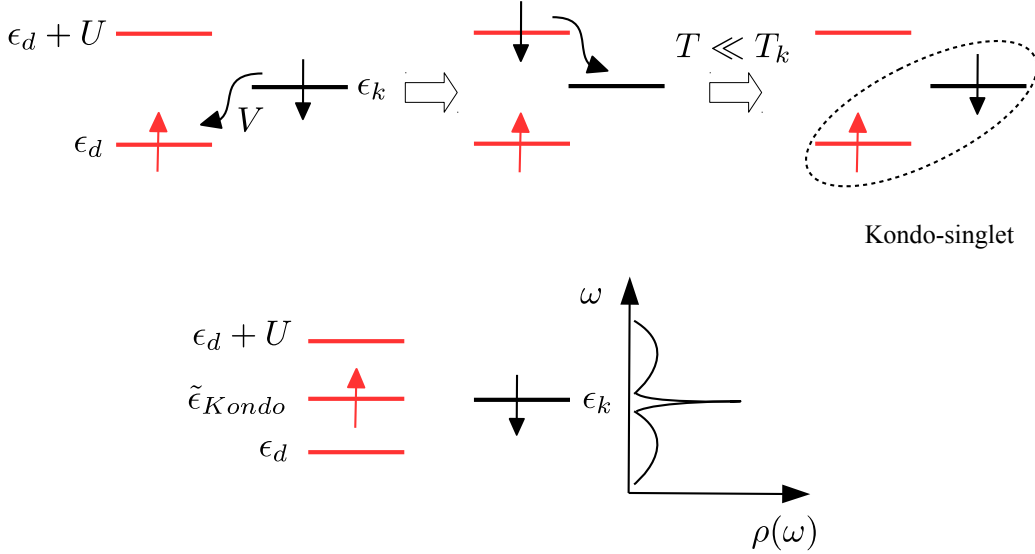


Figure 1: Schematic representation of the Kondo state formation by means of the two site Anderson model. The singly occupied impurity level (red), lies far below the Fermi level, $\epsilon_d < 0$ and the coupling V is weak compared to ϵ_d and U . Here we show one possible hopping process. As the conduction spin is antiparallel to the impurity, the charge fluctuations are possible. The conduction electron can hop to the impurity and stay there for a short time then hopes back to the conduction band. When temperature is low enough the impurity spin will be screened by the conduction electrons as the Kondo singlet forms. And the formation of the Kondo singlet state shows as a narrow peak at the Fermi level in the impurity density of states.

$$E = \epsilon_d - V^2 \left(\frac{1}{\epsilon_k - \epsilon_d - U} + \frac{1}{\epsilon_d - \epsilon_k} \right). \quad (5)$$

As H_1 does not conserve the d level occupancy, the first order contribution to the energy is zero. The second term in eq.(5) is due to the second order perturbation on the coupling. If we assume the conduction level is at the Fermi energy, i.e. $\epsilon_k = 0$ we get the following energy expression

$$E = \epsilon_d - V^2 \frac{U}{|\epsilon_d(U + \epsilon_d)|}, \quad (6)$$

where for the symmetric situation, $\epsilon_d = -U/2$ it becomes,

$$E = \epsilon_d - 4|V|^2/U. \quad (7)$$

It immediately becomes clear that minimising the kinetic energy occurs only in the case of the anti-ferromagnetic coupling, i.e. antiparallel alignment of the impurity spin and the spin of the conduction electron. Only in this situation the hopping between the impurity and the conduction band is allowed.

When electron hopping plays the main role in the exchange mechanism, we speak of kinetic exchange. The mechanism of creating a singlet-triplet splitting is called the kinetic exchange.⁵⁹ The kinetic exchange is driven by minimising kinetic energy, by allowing delocalization of electrons. This corresponds to using symmetric superpositions of wave functions, and so favours antisymmetric spins,

i.e. antiferromagnetic interactions. The estimated singlet-triplet splitting is proportional to J_{eff} (this will be further discussed in sec.3.1).

Another important point is that in the local moment limit, the Anderson model and Kondo model describe the same physics. A fundamental difference between the Anderson and Kondo model is that the Anderson model includes charge fluctuations, which determine the coupling, but they are absent in the Kondo model which includes only spin-spin interactions.⁵⁷ The interaction in the Kondo model is non-zero only in the case that we have a net spin on the impurity i.e. local moment regime. According to the above derivation, the effect of the charge fluctuations to second order on the coupling in the Anderson model, results in an antiferromagnetic interaction type in the Kondo model, namely,

$$J_{kk'} \propto J_{eff} = -V^2 \left(\frac{1}{\epsilon_k - \epsilon_d - U} + \frac{1}{\epsilon_d - \epsilon_k} \right) \quad (8)$$

(see eq.(5)). The complete derivation can be found in terms of the Schrieffer-Wolff transformations.⁵⁷

As we already discussed, the formation of a singlet state is favorable for the system. Due to the formation of this so-called Kondo singlet state the magnetic moment of the impurity is effectively screened or quenched by the interaction with the conduction electrons. In Fig. 1 we explain the schematic formation of the Kondo singlet state. In the density of states spectra, due to the formation of the Kondo singlet state, a new narrow resonance at the Fermi level appears. Alternatively, it can be argued that the singlet state emerges as a result of a new resonant level⁶⁰ which forms and stays pinned at the Fermi level. Hence the density of states, which for the case of the isolated impurity has a two peak structure, (at the corresponding energies, $-\epsilon_d$ and $\epsilon_d + U$) will turn into a three peak structure.

The width of the Kondo peak, which defines the hopping rate or tunneling rate, is proportional to the Kondo temperature T_k . The Kondo temperature known as a characteristic temperature below which the Kondo singlet forms. It sets the crossover between local moment behaviour where the spin is free and the low temperature physics, where the spin and conduction electrons are entangled to form a spin singlet.⁵⁸

It is also possible to have other situations, e.g. when the broadening Γ is no longer weak compared to U . In the regime which is called mixed valence regime, $\epsilon_d - \epsilon_F$ or $\epsilon_d - \epsilon_F + U$ becomes comparable with the coupling Γ . The charge fluctuations of the impurity become important and the Schrieffer-Wolf transformations to the Kondo model breaks down.⁸ Finally, there are two non magnetic regimes one, with no electrons called empty orbital, $|\epsilon_d - \epsilon_F| \gg \Gamma$ and the other in the state of double occupancy $|\epsilon_d + U - \epsilon_F| \ll \Gamma$.

2.2 Green's function

Green's functions or electronic propagators play a fundamental role in our treatment of many-particle systems. They refer to correlators of field operators. The detailed description can be found in many-body text books.^{57,61} It is common to adopt the Green's function and define new expressions, to obtain solutions to our arbitrary problems. Various types of single-particle Green's function exist, e.g. the retarded Green's function is defined as

$$G^R(r\sigma t, r'\sigma' t') = -i\theta(t - t') \langle \{ \Psi_\sigma(rt), \Psi_{\sigma'}^\dagger(r't') \} \rangle, \quad (9)$$

where

$$\{A, B\} = AB + BA \quad (10)$$

and the thermal average is given by,

$$\langle A \rangle = \frac{1}{Z} \sum_{\nu} \langle \nu | A | \nu \rangle e^{-\beta E_{\nu}}. \quad (11)$$

It is called retarded, because of the presence of the particle at r at time t depends on its position r' at an earlier time t' ($t > t'$). Similarly, the advanced Green's function is given by

$$G^A(r\sigma t, r'\sigma't') = i\theta(t' - t) \langle \{ \Psi_{\sigma}(rt), \Psi_{\sigma'}^{\dagger}(r't') \} \rangle. \quad (12)$$

Another two types of Green's functions which are called greater and lesser Green's functions:

$$G^{>}(r\sigma t, r'\sigma't') = -i \langle \Psi_{\sigma}(rt) \Psi_{\sigma'}^{\dagger}(r't') \rangle, \quad (13)$$

$$G^{<}(r\sigma t, r'\sigma't') = i \langle \Psi_{\sigma'}^{\dagger}(r't') \Psi_{\sigma}(rt) \rangle. \quad (14)$$

The greater Green's function corresponds to propagation of a particle and the lesser Green's function corresponds to propagation of a hole. The retarded and advanced Green's function can be expressed in terms of the greater and lesser Green's function:

$$G^R(r\sigma t, r'\sigma't') = \theta(t - t') [G^{>}(r\sigma t, r'\sigma't') - G^{<}(r\sigma t, r'\sigma't')], \quad (15)$$

$$G^A(r\sigma t, r'\sigma't') = \theta(t' - t) [G^{<}(r\sigma t, r'\sigma't') - G^{>}(r\sigma t, r'\sigma't')]. \quad (16)$$

Note that, even though we call this Green's function a *single-particle* Green's function they are truly many-body objects because they describe the propagation of single particles governed by the full many-body Hamiltonian. The point is that we can express many observables in terms of these powerful functions.⁶¹

In the next step, we will see that the Green's functions are indeed the solutions of equations of motion. The derivative with respect to the first time argument for the retarded Green's function is given by

$$i\partial_t G^R(rt, r't') = \delta(t - t')\delta(r - r') + (-i)\theta(t - t') \langle \{ i\partial_t \Psi(rt), \Psi^{\dagger}(r't') \} \rangle \quad (17)$$

Now assume a Hamiltonian which does not explicitly depend on time as

$$i\partial_t \Psi(rt) = -[H, \psi(r)](t). \quad (18)$$

$$H = H_0 + V_{int} \quad (19)$$

where H_0 stands for the quadratic part of the Hamiltonian, including both the kinetic energy contribution and the single particle potential energy, as they are both quadratic in creation and annihilation operators, and V_{int} contains all the interactions of the given problem. For the sake of convenience we introduce a basis set ν .

$$H_0 = \sum_{\nu\nu'} t_{\nu'\nu} a_{\nu'}^{\dagger} a_{\nu}, \quad (20)$$

with $t_{\nu\nu'} = \langle \nu | H_0 | \nu' \rangle$. After doing a bit of algebra we obtain the following:

$$\sum_{\nu''} (i\delta_{\nu\nu''} \partial_t - t_{\nu\nu''}) G^R(\nu''t, \nu't') = \delta(t - t')\delta_{\nu\nu'} + D^R(\nu t, \nu't'), \quad (21)$$

with $D^R(\nu t, \nu' t') = -i\theta(t - t')\langle[-[V_{int}, a_\nu](t), a_{\nu'}^\dagger(t')]\rangle$. Since the Hamiltonian does not explicitly depend on time, the Green's function can only depend on the time difference $t - t'$. Then it is useful to perform a Fourier transformation. Thus the equation of motion in the frequency domain can be found:

$$\sum_{\nu''}[(\delta_{\nu\nu''}(\omega + i\delta) - t_{\nu\nu''})G^R(\nu''\nu'; \omega) = \delta_{\nu\nu'} + D^R(\nu, \nu'; \omega), \quad (22)$$

where

$$D^R(\nu', \nu'; \omega) = -i \int_{-\infty}^{\infty} dt e^{i(\omega+i\delta)(t-t')} \theta(t - t') \langle[-[V_{int}, a_\nu](t), a_{\nu'}^\dagger(t')]\rangle. \quad (23)$$

To have proper convergence, the frequency of the retarded Green's function must carry a small positive imaginary part $i\delta$. recalling that H_0 includes the quadratic part of the Hamiltonian while V_{int} includes all the interactions. Differentiating the function in eq. (23) with respect to time would generate another function to be determined. Then the set of equations does not close. We will get back to the difficulties of this expression for the case of the Anderson impurity model later (see Sec. 2.3).

2.2.1 Lehmann representation

In order to derive the Lehmann representation or the spectral representation we use the set of eigenstates of the Hamiltonian H say, $\{|n\rangle\}$, as basis set. We also consider the diagonal Green's function,

$$\begin{aligned} G^>(\nu t, \nu' t') &= -i\langle c_\nu(t) c_\nu^\dagger(t') \rangle = -i \frac{1}{Z} \sum_n \langle n | e^{-\beta H} c_\nu(t) c_\nu^\dagger(t') | n \rangle \\ &= -i \frac{1}{Z} \sum_{nn'} e^{-\beta E_n} \langle n | c_\nu | n' \rangle \langle n' | c_\nu^\dagger | n \rangle e^{i(E_n - E_{n'})(t - t')}. \end{aligned} \quad (24)$$

In the frequency domain we obtain:

$$G^>(\nu; \omega) = \frac{-2\pi i}{Z} \sum_{nn'} e^{-\beta E_n} \langle n | c_\nu | n' \rangle \langle n' | c_\nu^\dagger | n \rangle \delta(E_n - E_{n'} + i\delta). \quad (25)$$

In the same way it can be proven that:

$$G^<(\nu; \omega) = -G^>(\nu; \omega) e^{-\beta\omega}. \quad (26)$$

Keep in mind that the retarded Green's function can be expressed in terms of lesser and greater Green's functions eq.(15). So the retarded Green's function can be expressed as

$$\begin{aligned} G^R(\nu, \omega) &= -i \int_0^\infty dt e^{i(\omega+i\delta)t} \frac{1}{Z} \sum_{nn'} e^{-\beta E_n} (\langle n | c_\nu | n' \rangle \langle n' | c_\nu^\dagger | n \rangle e^{i(E_n - E_{n'})t} \\ &\quad + \langle n | c_\nu | n' \rangle \langle n | c_\nu | n' \rangle e^{-i(E_n - E_{n'})t}) \\ &= \frac{1}{Z} \sum_{nn'} e^{-\beta E_n} \left(\frac{\langle n | c_\nu | n' \rangle \langle n' | c_\nu^\dagger | n \rangle}{\omega + E_n - E_{n'} + i\delta} + \frac{\langle n | c_\nu^\dagger | n' \rangle \langle n | c_\nu | n' \rangle}{\omega + E_n - E_{n'} + i\delta} \right) \\ &= \frac{1}{Z} \sum_{nn'} \frac{\langle n | c_\nu | n' \rangle \langle n' | c_\nu^\dagger | n \rangle}{\omega + E_n - E_{n'} + i\delta} (e^{-\beta E_n} + e^{-\beta E_{n'}}). \end{aligned} \quad (27)$$

The important point here is that the Lehmann representation shows explicitly that the Green's function is a sum of electron removal (first term) and electron addition (second term), taking the fact that $\langle n | c_\nu | n' \rangle \langle n' | c_\nu^\dagger | n \rangle = |\langle n | c_\nu | n' \rangle|^2$ and $\langle n | c_\nu^\dagger | n' \rangle \langle n' | c_\nu | n \rangle = |\langle n | c_\nu^\dagger | n' \rangle|^2$. The Lehmann expression further

allows to determine the Green's function from the exact many-body eigenstates. We will make use of it in the exact diagonalization (see Sec. 3.1) In this work we are mostly interested in zero temperature calculations, the corresponding zero temperature expression for the impurity level is

$$G^R(d\sigma, \omega) = \sum_n \frac{|\langle 0 | c_{d\sigma} | n \rangle|^2}{\omega + E_n - E_0 + i\delta} + \sum_n \frac{|\langle n | c_{d\sigma}^\dagger | 0 \rangle|^2}{\omega + E_0 - E_n + i\delta} \quad (28)$$

where $|0\rangle$ and E_0 denote the ground state and corresponding ground state energy. In case that the ground state is degenerate, we obtain

$$G^R(\nu, \omega) = \frac{1}{N_{deg}} \sum_{m=1}^{N_{deg}} \left(\sum_n \frac{|\langle 0_m | c_{d\sigma} | n \rangle|^2}{\omega + E_n - E_{0,m} + i\delta} + \sum_n \frac{|\langle n | c_{d\sigma}^\dagger | 0_m \rangle|^2}{\omega + E_{0,m} - E_n + i\delta} \right) \quad (29)$$

where N_{deg} refers to the number of ground state degeneracy. Furthermore we will use the Lehmann representation expression in order to introduce the spectral density.

2.2.2 Spectral density

Using

$$(\omega + i\delta)^{-1} = P \frac{1}{\omega} - i\pi\delta(\omega), \quad (30)$$

where P is a Cauchy principal and taking the imaginary part of eq. (27),

$$\text{Im } G^R(\nu, \omega) = -\frac{\pi}{Z} \sum_{nn'} \langle n | c_\nu | n' \rangle \langle n' | c_\nu^\dagger | n \rangle (e^{-\beta E_n} + e^{-\beta E_{n'}}) \delta(\omega + E_n - E_{n'}) \quad (31)$$

The spectral density or the spectral function, ρ is defined as

$$\rho(\nu, \omega) = -\frac{1}{\pi} \text{Im } G^R(\nu, \omega). \quad (32)$$

The spectral density can be written in terms of greater and lesser Green's function as well, namely,

$$\rho(\nu, \omega) = \frac{i}{2\pi} (G_\sigma^>(\nu, \omega) - G_\sigma^<(\nu, \omega)) \quad (33)$$

As can be seen in eq.(31) the spectral density is always positive. It also obeys

$$\int_{-\infty}^{\infty} d\omega \rho(\nu, \omega) = 1. \quad (34)$$

Hence the Spectral density has the properties of a probability distribution. For Further information we refer to e.g. the book written by Bruus and Flensberg.⁶¹ This concept, consideration of the spectral density as a probability distribution, will be further used in the distributional exact diagonalization (DED) approach (see Sec. 3.2).

2.3 Green's function for the Anderson model

Now we follow the equation of motion for the Anderson model. The impurity Green's function is:

$$G^R(d\sigma; t - t') = -i\theta(t - t') \langle \{ d_\sigma(t), d_\sigma^\dagger(t') \} \rangle \quad (35)$$

Since the Hamiltonian is non-diagonal in the d-operators due to the hybridization, the equations of motion will have another Green's function,

$$G^R(k\sigma, d\sigma, t - t') = -i\theta(t - t')\langle\{c_{k\sigma}(t), d_{d\sigma}^\dagger(t')\}\rangle \quad (36)$$

as well. By letting ν'' run over both d and k the following coupled equations are achieved:

$$(\omega + i\delta - \epsilon_d)G^R(d\sigma, \omega) - \sum_k V_k G^R(k\sigma, d\sigma, \omega) = 1 + U D^R(d\sigma, \omega), \quad (37)$$

$$(\omega + i\delta - \epsilon_k)G^R(k\sigma, d\sigma, \omega) - V_k^* G^R(d\sigma, \omega) = 0, \quad (38)$$

where

$$D^R(d\sigma, t - t') = -i\theta(t - t')\langle\{-[n_{d\uparrow}n_{d\downarrow}, c_{d\sigma}(t)], c_{d\sigma}^\dagger(t')\}\rangle. \quad (39)$$

The commutator for spin up $\sigma = \uparrow$ in eq.(39) is given by,

$$[n_{d\uparrow}n_{d\downarrow}, c_{d\uparrow}] = n_{d\downarrow}[n_{d\uparrow}, c_{d\uparrow}] = -n_{d\downarrow}c_{d\uparrow}. \quad (40)$$

Hence we face a more complicated expression

$$D^R(d\uparrow, t - t') = -i\theta(t - t')\langle\{n_{d\downarrow}(t)c_{d\uparrow}(t), c_{d\uparrow}^\dagger(t')\}\rangle \quad (41)$$

When the interactions are set to zero, $U = 0$, inserting $G^R(k\sigma, d\sigma, \omega)$ in eq.(37) which obtained from eq.(38), we find,

$$(\omega + i\delta - \epsilon_d)G_0^R(d\sigma, \omega) - \sum_k \frac{V_k V_k^*}{\omega + i\delta - \epsilon_k} G_0^R(d\sigma, \omega) = 1. \quad (42)$$

Subscript 0 refers to the non-interacting Green's function. Then the non-interacting impurity Green's function, $G_{d\sigma}^0(\omega)$ has a simple equation, namely,

$$G_{d\sigma}^0(\omega) = \frac{1}{\omega + i\delta - \epsilon_d - \Delta(\omega)} \quad (43)$$

with

$$\Delta(\omega) = \sum_k \frac{V_k V_k^*}{\omega + i\delta - \epsilon_k} \quad (44)$$

the hybridization function. The coupling occurs between the d orbital and the conduction band, giving rise to a hybridization $\Delta(\omega)$ between the two. The real part of the hybridization function describes the renormalization and the imaginary part the broadening of the impurity level. In this work we mainly focus on a flat hybridization. In order to make it clear we explore the analytic structure of this function. For simplicity we ignore the momentum dependency, assuming that $V_k = V$. Taking the imaginary part of the hybridization function and using eq.(30), we end up with the following expression for the imaginary part of the hybridization function:

$$\Delta^I(\omega) = \pi V^2 \sum_k \delta(\omega - \epsilon_k) = \pi V^2 \rho_c(\omega), \quad (45)$$

where $\rho_c(\omega)$ is the host density of states. A further simplification is to assume a constant conduction density of states. The Fermi level we take to be at the center of the band $\epsilon_F = 0$, and we assume energy cutoffs for the conduction band are at $-D$ and D . Therefore, the imaginary part of the hybridization

function is constant between $-D$ and D . The real part, can be obtained from the Kramers–Kronig relation:

$$\Delta^R(\omega) = \frac{1}{\pi} P \int_{-\infty}^{\infty} d\omega' \frac{\Delta^I(\omega')}{\omega - \omega'} = \frac{1}{\pi} P \int_{-D}^D d\omega' \frac{\Gamma}{\omega - \omega'} = -\frac{\Gamma}{\pi} \log \left| \frac{D - \omega}{D + \omega} \right| \quad (46)$$

In the wide band limit $D \rightarrow \infty$ the real part of the hybridization vanishes. This situation is approximately realized in noble metals which have s-like conduction electrons.

However, generally one has to take care of the interactions U which means dealing with a complicated expression, eq. (39). Thus the concept of self-energy Σ is introduced as the feedback of the interacting environment on a propagating particle.⁵⁸ Now in order to express the self-energy in terms of impurity correlation functions we do the same as what we did for eq. (42) but including the interactions,

$$(\omega + i\delta - \epsilon_d)G^R(d\sigma, \omega) - UD^R(d\sigma, \omega) - \sum_k \frac{V_k V_k^*}{\omega + i\delta - \epsilon_k} G^R(d\sigma, \omega) = 1. \quad (47)$$

We define the self-energy as,⁶²

$$\Sigma(\omega) = U \frac{D(d\sigma, \omega)}{G(d\sigma, \omega)}. \quad (48)$$

This allows to solve eq. (47) for the Green's function, which yields the Dyson equation,

$$G = G_0 + G_0 \Sigma G = \frac{1}{[G_0]^{-1} - \Sigma}. \quad (49)$$

Hence, the impurity propagator can be written as follows

$$G(d\sigma, \omega) = \frac{1}{\omega + i\delta - \epsilon_d - \Delta(\omega) - \Sigma(\omega)}. \quad (50)$$

Solving the Anderson model thus means finding the self-energy $\Sigma(\omega)$. It is difficult to calculate the self-energy exactly. Therefore various methodologies that have been developed to solve the Anderson model, apply different approximations to the self-energy. Also in this work we present a method to approximate the self-energy as an ensemble average of the finite size Anderson models.

2.4 Local moment formation in the Hartree-Fock Approximation

We now study the formation of a local moment on the impurity in the Hartree-Fock approximation. In order to do so we look at the occupancy of the state of the impurity. In simple words, when a state is occupied with a spin up and a spin down electron with equal probability, this state is not magnetic, while if there is a higher probability to occupy the state with one given spin than the other i.e. $\langle \hat{n}_{d\uparrow} \rangle \neq \langle \hat{n}_{d\downarrow} \rangle$, then the state is basically magnetic and will have a local moment. It should be mentioned that the procedure we are explaining for the local moment formation here, is only valid in the context of the mean field approximation, where breaking the spin symmetry exists. In this part we explore the solution of the Anderson model and local moment formations in a many-body system by means of the Hartree-Fock approximation. The interaction part U is replaced by its mean-field version

$$U d_{\uparrow}^{\dagger} d_{\uparrow} d_{\downarrow}^{\dagger} d_{\downarrow} = U n_{d\uparrow} n_{d\downarrow} \rightarrow U (\langle \hat{n}_{d\uparrow} \rangle \hat{n}_{d\downarrow} + \langle \hat{n}_{d\downarrow} \rangle \hat{n}_{d\uparrow} - \langle \hat{n}_{d\downarrow} \rangle \langle \hat{n}_{d\uparrow} \rangle) \quad (51)$$

The last term makes a shift to the whole system and thus does not affect the physics of the problem so that we drop it. Then the Anderson Hamiltonian is rewritten as

$$H^{HF} = \sum_{\sigma} \tilde{\epsilon}_{d\sigma} \hat{n}_{d\sigma} + \sum_{k,\sigma} (V_k c_{k\sigma}^{\dagger} d_{\sigma} + V_k^* d_{\sigma}^{\dagger} c_{k\sigma}) + \sum_{k,\sigma} c_{k\sigma}^{\dagger} c_{k\sigma} \quad (52)$$

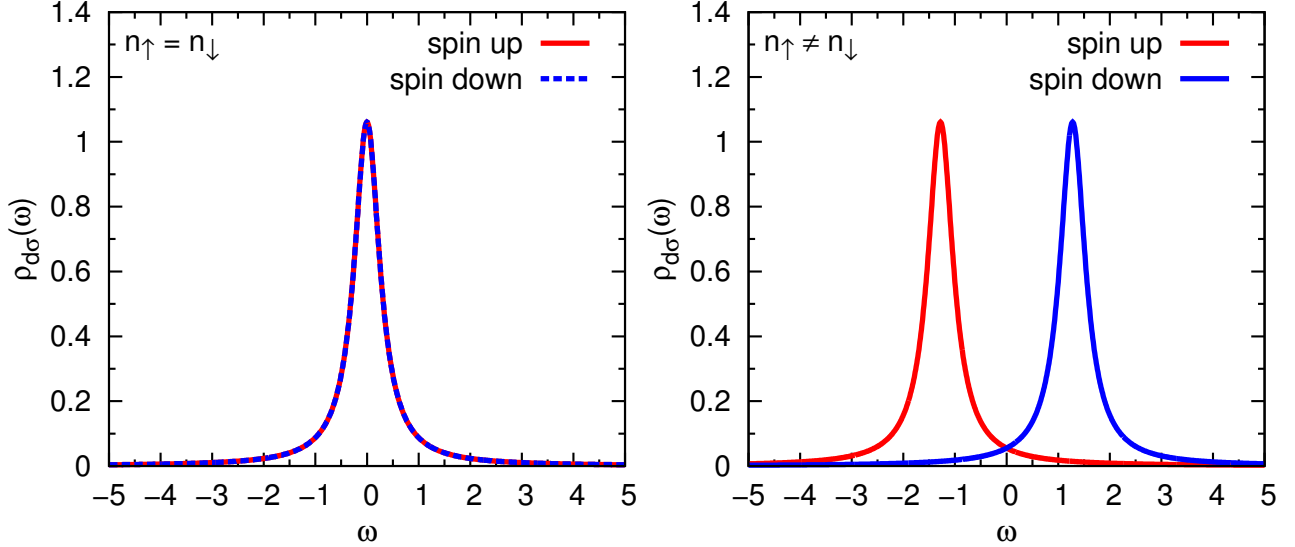


Figure 2: Hartree-Fock solution of the AIM: the spectral density of the impurity (d) electron for the non spin-polarized situation (LEFT) and the spin-polarized situation (RIGHT).

where $\tilde{\epsilon}_{d\sigma} = \epsilon_d + U\langle\hat{n}_{d-\sigma}\rangle$ and the corresponding Green's function is expressed as

$$G_{d\sigma}^{HF}(\omega) = \frac{1}{\omega - \tilde{\epsilon}_{d\sigma} - \Delta(\omega)}. \quad (53)$$

The hybridization function $\Delta(\omega)$, assumed to be a constant, $-i\Gamma$. Hence the spectral density becomes

$$\rho_{d\sigma}(\omega) = -\frac{1}{\pi} \text{Im} G_{d\sigma}^{HF}(\omega) = \frac{1}{\pi} \frac{\Gamma}{(\omega - \tilde{\epsilon}_d)^2 + \Gamma^2}, \quad (54)$$

which is a Lorentzian centered at $\tilde{\epsilon}_{d\sigma} = \epsilon_d + U\langle\hat{n}_{d-\sigma}\rangle$ with the width of Γ . To calculate the occupancy per spin the following equation is applied,

$$\langle\hat{n}_{d\sigma}\rangle = \int_{-\infty}^{\epsilon_F} d\omega \rho_{d\sigma}(\omega) = \frac{1}{\pi} \cot^{-1} \left(\frac{\tilde{\epsilon}_{d\sigma}}{\Gamma} \right). \quad (55)$$

Note that we set the Fermi energy to zero, and we consider low temperatures $T = 0$. Hence the spin up and spin down occupation are coupled via the following equations and have to be solved self-consistently,

$$\langle\hat{n}_{d\uparrow}\rangle = \frac{1}{\pi} \cot^{-1} \left(\frac{\epsilon_d + U\langle\hat{n}_{d\downarrow}\rangle}{\Gamma} \right) \quad (56)$$

and

$$\langle\hat{n}_{d\downarrow}\rangle = \frac{1}{\pi} \cot^{-1} \left(\frac{\epsilon_d + U\langle\hat{n}_{d\uparrow}\rangle}{\Gamma} \right). \quad (57)$$

These equations are the main equations of the Hartree-Fock approximation to the Anderson model. As we are doing the mean field approximation, local moments can be found in the magnetic regions. Mean field theory is often used to study phase transitions and thus changes of symmetry.⁶¹ Here as the Hamiltonian commutes with spin, changes in the spin symmetry is investigated. In Fig. 2, we show the impurity (d) electron spectral density $\rho_{d\sigma}(\omega) = -\frac{1}{\pi} \text{Im} G_{d\sigma}^{HF}$ for different spin channels with both the non spin-polarized (left) and spin-polarized (right) initial guess. The symmetric AIM with, $U = 3$, $\epsilon_d = 1.5$ and $\Gamma = 0.3$ is considered. For a non spin-polarized initial guess $n_{\uparrow} = n_{\downarrow}$ the spectrum is a

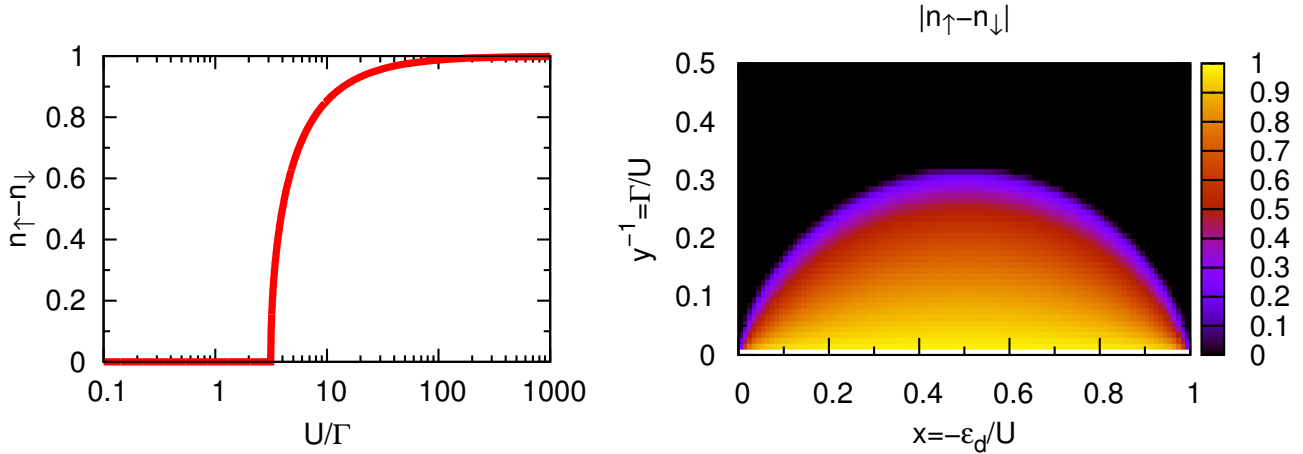


Figure 3: Hartree-Fock solution of the AIM: Spin-polarization versus $y = U/\Gamma$ for the symmetric AIM ($\epsilon_d = -U/2$ and $x = 1/2$) on the half-log scale (LEFT). Spin-polarization versus $x = -\epsilon_d/U$ and $y^{-1} = \Gamma/U$ (RIGHT). The colorful area shows the magnetic region where local moments form while the black area shows the non-magnetic region with no local moments.

single Lorentzian peak centered at zero for the both spin up and down channels. The Fermi energy is set to zero. Tuning the spin-up occupation slightly larger than the spin down occupation, $n_{\uparrow} = n_{\downarrow} + \delta n$ for the initial guess, we now look at the spin-polarized situation. The corresponding spectrum can be found on the right hand side of Fig.2. We see that the spectra turned into a double Lorentzian, each of which presents a specific spin channel.

Since we already saw the spin symmetry broken, as is required for the mean-field approaches, in the next step, we search for the magnetic regimes where the local moments can form. Solving eq. (56) and eq. (57) gives the occupation of the impurity level (d-level) and tells us whether there is magnetization or not. In other words, whether there exists a solution where $\langle \hat{n}_{d\uparrow} \rangle \neq \langle \hat{n}_{d\downarrow} \rangle$ different from the non-magnetic solution $\langle \hat{n}_{d\uparrow} \rangle = \langle \hat{n}_{d\downarrow} \rangle$. We immediately notice that if $U = 0$, the only possible solution is $\langle \hat{n}_{d\uparrow} \rangle = \langle \hat{n}_{d\downarrow} \rangle$, which is non-magnetic. In the limit $\Gamma \rightarrow \infty$, there is again a non-magnetic solution $\langle \hat{n}_{d\uparrow} \rangle = \langle \hat{n}_{d\downarrow} \rangle = 1/2$. A magnetic solution exists, however, in the intermediate parameter range, $\Gamma/U \ll 1$. To simplify the notation we introduce the dimensionless parameters $x = -\epsilon_d/U$ and $y = U/\Gamma$. Hence $x = 0$ corresponds to the d-level energy ϵ_d lying right at the Fermi level. At $x = 1$, we have $\epsilon_d = -U$, and thus the upper d-state with energy $\epsilon_d + U$ is degenerate with the Fermi level. Hence, magnetization exist only in this interval, $0 < x < 1$. So the borders located symmetrically around the symmetric situation $x = 1/2$ or $\epsilon_d = -U/2$.

Now, we show the transition between the magnetic and the non-magnetic area by means of the Hartree-Fock approximation in Fig. 3. First we consider the symmetric regime, $\epsilon_d = -U/2$ and $x = 1/2$. On the left hand side the spin polarization $n_{\uparrow} - n_{\downarrow}$ is shown versus $y = U/\Gamma$. In order to have better resolution we show it on the half-log scale. Approximately below $U/\Gamma = 3.1$ there is no magnetic solution. Around $U/\Gamma = 3.1$ the spin polarized area starts to appear. Moving towards higher U/Γ values, the spin up population increases and consequently the spin down population decreases. This behaviour continues until the spin up is completely dominant.

To explore other regions (not only particle hole symmetric area) we also alter x between 0 and 1.

In Fig. 3 on the right hand side, the spin polarization magnitude $|n_{\uparrow} - n_{\downarrow}|$ versus $x = -\epsilon_d/U$ and $y^{-1} = \Gamma/U$ is shown. The symmetric situation, $x = 1/2$ and $\epsilon_d = -U/2$ in the middle of the plot is the most favorable case for the magnetic moment to form. Moving from the middle, $x = 1/2$ (symmetric case) on either side corresponds to the mixed valence regime. On the left (right) region the lower (upper) level is nearly degenerate with the Fermi level. A slight change in Γ leads to the non-magnetic solution and consequently, loss of the local moment. Further useful discussion can be found e.g. in the book of Philip Phillips.⁵⁷

3 Method

3.1 Exact Diagonalization

The main idea of the exact diagonalization (ED) method is to approximate the infinite and continuous many-body Hamiltonian by a discretized finite one, which can be diagonalized exactly. This yields the exact eigenvalues $\{E_n\}$ and the exact eigenstates $\{|\Psi_n\rangle\}$ of the finite many-body Hamiltonian,

$$\hat{H}|\Psi_n\rangle = E_n|\Psi_n\rangle, \quad (58)$$

The starting point is to set up the basis sets. Our choice for the basis sets, $\{|\phi_n\rangle\}$, are Slater determinants for fermions, which span the Hilbert space. The Hamiltonian matrix elements in the selected basis, can then be obtained as,

$$H_{mn} = \langle\phi_m|\hat{H}|\phi_n\rangle. \quad (59)$$

The direct diagonalization of the Hamiltonian matrix provides the eigenstates,

$$|\Psi_n\rangle = \sum_m C_{mn}|\phi_m\rangle, \quad (60)$$

and the eigenenergies

$$E_n = \langle\Psi_n|\hat{H}|\Psi_n\rangle. \quad (61)$$

It should be emphasized that once the eigenstates $\{|\Psi_n\rangle\}$ and the eigenenergies $\{E_n\}$ are determined, all system properties can be derived. However, ED is only able to deal with finite size systems i.e. finite Hilbert spaces. The two-body term in the Hamiltonian causes a rapid growth of the many body Hilbert space. Due to that, the number of bath levels used to represent the conduction band is very limited. To make it clear, assume a finite system including impurity and bath levels. The size of the corresponding single-particle Hilbert space underlying the Fock space is n_{dim} . This system can then be filled by different number of electrons, i.e. $n_{\text{el}} = 0, 1, \dots, 2n_{\text{dim}}$. Thus the Fock space can be constructed as a sum of a set of Hilbert spaces representing zero-particle states, one-particle states, ... and $2n_{\text{dim}}$ -particle states. The size of the corresponding Hilbert space for the each occupancy subspace is given by,

$$\text{Dim}\{n_{\text{el}}\} = \binom{2n_{\text{dim}}}{n_{\text{el}}}, \quad (62)$$

while the memory needed in order to save the whole corresponding Hamiltonian matrix is,

$$\text{Dim}\{H_{n_{\text{el}}}\} = \binom{2n_{\text{dim}}}{n_{\text{el}}}^2. \quad (63)$$

The largest Hilbert space belongs to the half-filled subspace, where $n_{\text{el}} = n_{\text{dim}}$. Finally, the total dimension of the Fock space including all the Hilbert spaces representing the occupancy subspaces is,

$$\sum_{n_{\text{el}}=1}^{2n_{\text{dim}}} \binom{2n_{\text{dim}}}{n_{\text{el}}} = 2^{2n_{\text{dim}}}. \quad (64)$$

It immediately becomes clear that calculations are restricted by the available computer memory. Due to the exponential growth of the Hilbert space and consequently the Hamiltonian with the system size, only a few number of bath levels can be considered. ED implementation with the full matrix

diagonalization for 8 levels with the maximum Hamiltonian dimension, 4900 has been reported.⁶³ The point is that the simple ED yields all the eigenenergies and eigenstates via the direct diagonalization. Hence in order to diagonalize the Hamiltonian matrix the entire matrix has to be saved which is very expensive. To circumvent this problem and specially for the situations that all eigenenergies are not needed the Lanczos method and the Arnoldi algorithm are particularly suited. The Green's functions and consequently the spectral functions can be found using the Lanczos method for the ground state. The full exact diagonalization which is limited to below 10 levels, can then be extended to 15 or even higher when the Lanczos algorithm is used.⁶⁴ The Arnoldi algorithm, is suited for evaluating those excited states that are physically important at low temperatures. This scheme allows the consideration of 12-15 levels with the maximum Hamiltonian dimension around $(10^6, \dots, 4 \times 10^6)$ without significantly increased storage requirement.^{35,65} In this work we only make use of the simple ED where we diagonalize the full Hamiltonian matrix and we obtain all the corresponding eigenenergies and eigenstates. But we plan to implement the Lanczos in near future.

By making use of symmetries e.g. the spin S^2 and S_z the Hamiltonian can become block-diagonal. Then the blocks can be diagonalized individually which allows to reach larger number of bath levels. In order to do so, symmetries of the system i.e. the conserved properties of the system should be taken into account. In the following, we illustrate the ED formalism on the example of the two-site Anderson model, which can be solved analytically.

3.1.1 Two-site Anderson model

Calculating the many body eigenstates for a simple version of the single AIM, including one conduction band site at the fermi level (zero band width limit) $\epsilon_k = 0$, gives some insight into the Kondo problem.⁸ Therefore in the following we go through the exact diagonalization process for this system. The corresponding Anderson Hamiltonian is simply given by,

$$H_{\text{ZB}} = \epsilon_d \hat{n}_d + U n_{d\uparrow} n_{d\downarrow} + \epsilon_k \hat{n}_k + \sum_{\sigma} V_k (c_{k\sigma}^{\dagger} d_{\sigma} + d_{\sigma}^{\dagger} c_{k\sigma}), \quad (65)$$

where $\hat{n}_d = d_{\sigma}^{\dagger} d_{\sigma}$ and $\hat{n}_k = c_{k\sigma}^{\dagger} c_{k\sigma}$ are the number operators for the impurity level and the bath site, respectively. The symmetric Anderson model is considered and the Fermi energy is set to zero. As each energy level can be occupied at most by two electrons of unlike spin. Therefore we have four possible occupancy subspaces i.e. $n_{\text{el}} = 0, 1, 2, 3$ or 4. Accordingly we divide the basis into different subspaces with respect to the electron numbers.

The dimension of the Hilbert space for the 1-electron basis is $\binom{4}{1} = 4$ and the corresponding basis vectors are

$$\{|d \uparrow\rangle, |d \downarrow\rangle, |0 \uparrow\rangle, |0 \downarrow\rangle\}. \quad (66)$$

Note that we use $|0\sigma\rangle$ notation for the bath state, as it lies at the Fermi level ($\epsilon_F = 0$). Thus the Hamiltonian matrix for the 1-electron subspace is given by,

$$H^{(1)} = \begin{pmatrix} \epsilon_d & 0 & V & 0 \\ 0 & \epsilon_d & 0 & V \\ V & 0 & 0 & 0 \\ 0 & V & 0 & 0 \end{pmatrix}.$$

As can be seen the Hamiltonian matrix is quite sparse. Although, for such a small system the computational cost is not important, generally we have to deal with larger systems. More efficiently, the block matrices should be diagonalized instead of the whole matrix. To build the block matrices, the symmetries of the system must be considered. The Anderson Hamiltonian commutes with S_z , $[H, S_z] = 0$, i.e. spin is conserved. Therefore we build the spin blocks, where the blocks correspond to fixed values of S_z . Also, intuitively can be seen in the Hamiltonian matrix, $H^{(1)}$, that by displacing the second and third row and column, we can make two blocks on the top left and bottom right. This is equivalent to swap the second and third basis states in eq. (66), which results in ordering the basis states with respect to spin up and down. Hence, the corresponding 1-electron Hamiltonian matrix per spin subspace is:

$$H_\sigma^{(1)} = \begin{pmatrix} \epsilon_d & V \\ V & 0 \end{pmatrix}.$$

Diagonalizing the Hamiltonian matrix, yields the eigenenergies,

$$E_{\sigma,\pm}^{(1)} = \frac{\epsilon_d}{2} \pm \sqrt{\frac{\epsilon_d^2}{4} + V^2}. \quad (67)$$

Let's move to the 2-electron subspace. The dimension of the Hilbert space for this case is $\binom{4}{2} = 6$. Since in the two electron case the spin and the spatial part can be separated, hence the spin state can be classified as either singlets, $S = 0, S_z = 0$ or triplets, $S = 1, S_z = 0, \pm 1$. In the triplet case the spatial part of the wave function must be antisymmetric, so the levels cannot be doubly occupied. Therefore the interaction, U , does not play any role, and the total energy of the triplet states is $\epsilon_d + \epsilon_k$. The triplet states $S = 1, S_z = -1, 0, 1$ are:

$$|0, d\rangle^{(-)} \otimes \begin{cases} |\downarrow, \downarrow\rangle \\ \frac{1}{\sqrt{2}}(|\uparrow, \downarrow\rangle + |\downarrow, \uparrow\rangle) \\ |\uparrow, \uparrow\rangle \end{cases}$$

In the singlet case $S = S_z = 0$ there are three possible states with different energies:

$$\left. \begin{array}{l} |d, d\rangle \\ \frac{1}{\sqrt{2}}(|0, d\rangle - |d, 0\rangle) \\ |0, 0\rangle \end{array} \right\} \otimes |\uparrow, \downarrow\rangle^{(-)}$$

The corresponding singlet subspace of the 2-electron Hamiltonian is given by,

$$H_s^{(2)} = \begin{pmatrix} 0 & \sqrt{2}V & 0 \\ \sqrt{2}V & \epsilon_d & \sqrt{2}V \\ 0 & \sqrt{2}V & 0 \end{pmatrix}$$

where the corresponding eigenenergies can be found by the direct diagonalization, namely,

$$E_{0,s}^{(2)} = 0, \quad (68)$$

$$E_{\pm,s}^{(2)} = \epsilon_d/2 \pm \sqrt{\epsilon_d^2/4 + 4V^2}. \quad (69)$$

By comparing the eigenenergies of the singlet and triplet subspaces we find that the minimum singlet eigenenergy, $E_-^{(s)} = \epsilon_d/2 - \sqrt{\epsilon_d^2/4 + 4V^2}$ is lower than the triplet eigenenergy, $E^{(t)} = \epsilon_d$ (with $\epsilon_k = 0$).

Thus the ground state of the system is a singlet state, which explains the origin of the Kondo singlet state formation.

We now look at the singlet-triplet splitting for the symmetric Anderson model ($\epsilon_d = -U/2$):

$$E^{(t)} - E^{(s)} \approx \frac{8V^2}{U}, \quad (70)$$

with $U \gg V$. This value is identical to $2J_{\text{eff}}$, where J_{eff} is given in the Schrieffer-Wolff transformation and to $J_{kk'}$ in the Kondo model, eq. (4) (see Sec 2.1).

We further continue by considering the 3-electron subspace. The dimension of the Hilbert space for the 3-electron basis is $\binom{4}{3} = 4$. The corresponding basis, ordered with respect to the spin, is

$$\{|d \uparrow, d \downarrow, 0 \uparrow\rangle, |d \uparrow, 0 \uparrow, 0 \downarrow\rangle, |d \uparrow, d \downarrow, 0 \downarrow\rangle, |d \downarrow, 0 \uparrow, 0 \downarrow\rangle\}. \quad (71)$$

The corresponding Hamiltonian matrix for the 3-electron subspace per spin is then given by,

$$H_{\sigma}^{(3)} = \begin{pmatrix} 0 & V \\ V & \epsilon_d \end{pmatrix}.$$

The eigenenergies, which can be found by diagonalizing the Hamiltonian matrix can be obtained as,

$$E_{\sigma, \pm}^{(3)} = \frac{\epsilon_d}{2} \pm \sqrt{\frac{\epsilon_d^2}{4} + V^2}. \quad (72)$$

Thus the eigenenergies of the 1-electron and 3-electron subspaces are identical. Indeed, the 3-electron subspace is nothing but the 1-hole subspace, which due to particle-hole must be equivalent.

Since we are already equipped with the eigenenergies of 1-electron, 2-electron and 3-electron subspaces, in the next step, we compute the excitation energies from the ground state (2-electron) subspace to the one electron less (1-electron) subspace:

$$E_{-}^{(s)} - E_{+}^{(1)} \approx \epsilon_d - 2J_{\text{eff}} - J_{\text{eff}}/2 = \epsilon_d - 5J_{\text{eff}}/2, \quad (73)$$

$$E_{-}^{(s)} - E_{-}^{(1)} \approx \epsilon_d - 2J_{\text{eff}} - \epsilon_d + J_{\text{eff}}/2 = -3J_{\text{eff}}/2. \quad (74)$$

and to the one electron more (3-electron) subspace:

$$E_{-}^{(s)} - E_{+}^{(3)} = E_{-}^{(s)} - E_{+}^{(1)} = \epsilon_d - 5J_{\text{eff}}/2, \quad (75)$$

$$E_{-}^{(s)} - E_{-}^{(3)} = E_{-}^{(s)} - E_{+}^{(1)} = -3J_{\text{eff}}/2. \quad (76)$$

The second set of the equations, (75,76) can be again understood in terms of the particle-hole symmetry. As the 1-electron and the 3-electron(1-hole) subspaces are identical due to the particle-hole symmetric condition, consequently the the excitation energies to the half-filled (2-electron) subspace must be equal of course with the opposite sign.

In Fig. 4 we show the spectral density $\rho(\omega) = -\frac{1}{\pi} \text{Im} G_{d\sigma}(\omega)$ of the impurity (d) level per spin for both the symmetric (left side) and the asymmetric Anderson model (right side). $G_{d\sigma}(\omega)$ is computed from the Lehmann representation. Hence it becomes clear that the spectrum indeed shows the excitations from the 2-electron ground state on adding or removing one d electron. The peak positions are already derived according to equations.(73-76).

Hence, it can be seen that using ED for such a simple system can give an illustration to the Kondo physics. Moreover, the particle hole symmetry can be very well conceived.

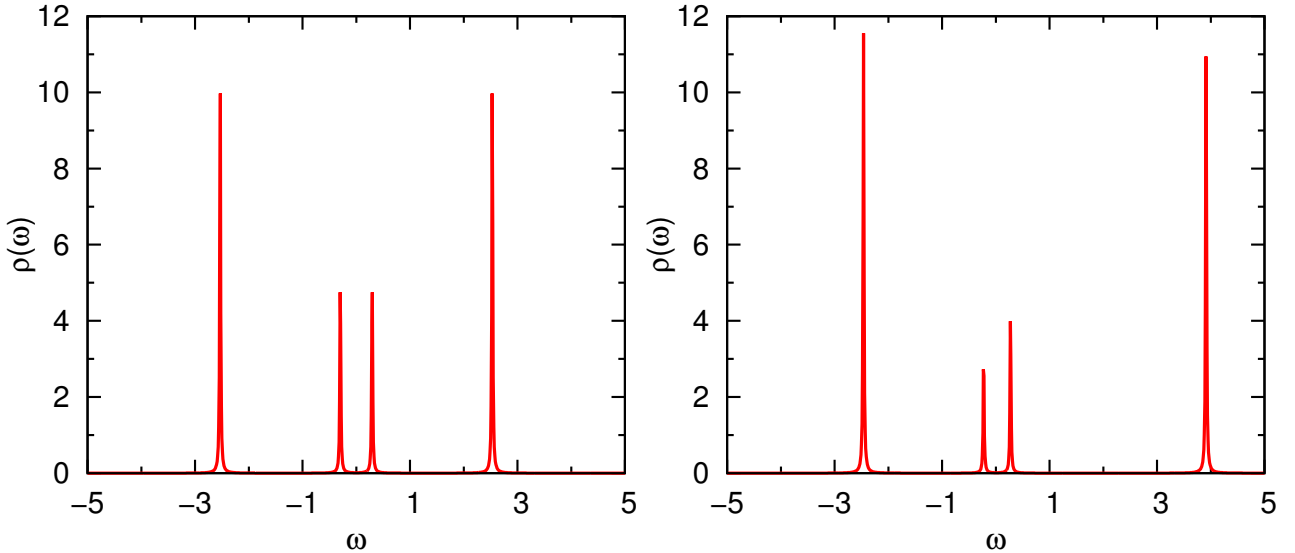


Figure 4: Spectral density calculated by ED for a two-site Anderson model (including one impurity level and one bath site) for the symmetric case $\epsilon_d = -2$, $\epsilon_k = 0.0$, $V = 0.5$ and $U = 4$ (LEFT), and the asymmetric case $\epsilon_d = -2$, $\epsilon_k = 0.0$, $V = 0.5$ and $U = 5.5$ (RIGHT).

3.1.2 Some implementation details of the exact diagonalization procedure

In this section we explain in detail the technical implementation of the ED method for the general case. At first, the basis sets should be represented. Our basis sets, Slater determinants for fermions, $\{|\phi_m\rangle\}$, are represented in the occupation number representation. The reason of this choice is, that in this way they can be represented by binary digits of integer numbers. Since a bit can have only one of these two values, either 0 or 1, it is similar to a fermionic state, which can be either occupied by an electron with a certain spin or unoccupied. In order to make it clear we continue with an examples. Consider a 3-site system $n_{\text{dim}} = 3$, consisting of a single impurity (d) level plus two bath sites k_1, k_2 , which is filled with 3 electrons. One possible configuration with the corresponding integer number is,

$$|d \uparrow, k_1 \downarrow, k_2 \uparrow\rangle = |100110\rangle \rightarrow 1 \times 2^0 + 0 \times 2^1 + 0 \times 2^2 + 1 \times 2^3 + 1 \times 2^4 + 0 \times 2^5 = 25. \quad (77)$$

Once the basis set is set up, the next step is ordering the basis in terms of the system symmetry. Since the spin S_z is conserved in the AIM, i.e. $[H, S_z] = 0$, we classify the Slater determinants according to the spin S_z .

Now the block Hamiltonian matrices corresponding to a specific occupancy and a certain spin value can be built up. Generally, the Hamiltonian can be separated in terms of the one-body and two-body interaction terms

$$H_1 = \sum_{\sigma} \sum_{i,j} t_{ij} c_{i\sigma}^{\dagger} c_{j\sigma}, \quad (78)$$

and

$$H_2 = \frac{1}{2} \sum_{\sigma, \sigma'} \sum_{i,j,k,l} U_{ijkl} c_{i\sigma}^{\dagger} c_{j\sigma'}^{\dagger} c_{l\sigma'} c_{k\sigma}, \quad (79)$$

respectively, where i, j, k and l run over the number of sites. Here, e.g. the first position is assigned to spin up and the second to spin down. Note that as the idea is to obtain the Hamiltonian matrix for a

very general situation, the general expression for the two-body interaction eq. (79) is used. However, if acquiring the Hamiltonian matrix for the single impurity is the case, then the corresponding two-body Hamiltonian matrix is much simpler. The Hamiltonian now acts on the basis sets and constructs new states, obviously different from the initial ones. To make it clear, we assume a two-site model and we act with the corresponding Hamiltonian on an arbitrary basis state, say, $|1001\rangle$. Acting with the one-body part yields,

$$\begin{aligned} \sum_{\sigma} \left(t_{11} c_{1\sigma}^{\dagger} c_{1\sigma} + t_{12} c_{1\sigma}^{\dagger} c_{2\sigma} + t_{21} c_{2\sigma}^{\dagger} c_{1\sigma} + t_{22} c_{2\sigma}^{\dagger} c_{2\sigma} \right) |1001\rangle &= (-1)^0 (-1)^0 t_{11} |1001\rangle \\ &+ (-1)^1 (-1)^1 t_{12} |1100\rangle \\ &+ (-1)^1 (-1)^1 t_{21} |0011\rangle \\ &+ (-1)^0 (-1)^0 t_{22} |1001\rangle \end{aligned} \quad (80)$$

and the corresponding non-zero matrix elements for this case are,

$$\langle 1001 | H_1 | 1001 \rangle = t_{11} + t_{22} \quad (81)$$

$$\langle 1100 | H_1 | 1001 \rangle = t_{12} \quad (82)$$

$$\langle 0011 | H_1 | 1001 \rangle = t_{21}. \quad (83)$$

Acting with the two-body part of the Hamiltonian on the same basis, $|1001\rangle$, gives zero. The two-body interaction is nonzero only when the impurity level is doubly occupied, namely,

$$\begin{aligned} 1/2 \sum_{\sigma\sigma'} U_{1111} c_{1\sigma}^{\dagger} c_{1\sigma'}^{\dagger} c_{1\sigma'} c_{1\sigma} |1100\rangle &= U_{1111} (-1)^0 c_{1\sigma}^{\dagger} c_{1\sigma'}^{\dagger} c_{1\sigma'} c_{1\sigma} |0100\rangle \\ &= U_{1111} (-1)^0 (-1)^0 c_{1\sigma}^{\dagger} c_{1\sigma'}^{\dagger} |0000\rangle \\ &= U_{1111} (-1)^0 (-1)^0 (-1)^0 c_{1\sigma}^{\dagger} |0100\rangle \\ &= U_{1111} |1100\rangle \end{aligned} \quad (84)$$

and consequently the only nonzero matrix element for this case is according to,

$$\langle 1100 | H_2 | 1100 \rangle = U_{1111}. \quad (85)$$

We should add a bit of explanation regarding the sign attribution to states during acting with the field operators of the Hamiltonian. When the number of the occupied positions behind the acted position (where the electron will be added or removed), m , is odd, the corresponding sign is negative and when m is even the sign is positive. More, assume $c_{3\uparrow} |110010\rangle$, which we should remove an electron from the first position of the second bath site (third site). The number of occupied positions behind it is $m = 2$ (the first and second positions are occupied while the third and fourth are empty), hence the result is $(-1)^2 |110000\rangle$. The last point is that due to the hermiticity of the Hamiltonian matrix, $H_{mn} = H_{nm}$ we do not need to calculate all the matrix elements.

3.2 The distributional exact diagonalization Algorithm

In this chapter we review the distributional exact diagonalization (DED) approach, originally introduced by Granath and Strand.⁵⁴ We consider the AIM of a single interacting impurity level coupled to an infinite conduction electron bath according to eq. (1). The general idea of the DED approach is to map the infinite Anderson model to an ensemble of relatively small finite Anderson models, instead of a single effective Anderson model. Each finite Anderson model can then be solved exactly by exact diagonalization. Our starting point is the non-interacting retarded Green's function G_0 , including Σ_0 :

$$G_0(\omega) = \frac{1}{\omega^+ - \epsilon_d - \Sigma_0 - \Delta(z)} \quad (86)$$

Where $\omega^+ = \omega + i\delta$, with δ , a positive infinitesimal. Σ_0 can be understood as an effective one-body potential for the non-interacting reference system. Its exact role will be elucidated later in Sec.3.3. Anticipating our later discussion, we mention here that Fermi liquid theory considerations suggest that Σ_0 should be the real part of the interacting self-energy at the Fermi level. It is here in including Σ_0 at this stage, and interpreting it as an effective one-body potential that our approach deviates from that originally proposed by Granath and Strand.⁵⁴

In the next step, we need to replace the continuous nature of the infinite AIM by the discretized electronic states in order to feed them into the exact diagonalization process. Therefore the representation of the non-interacting Green's function of the impurity level G_0 in terms of a large number M of poles b_i on the real axis is considered:

$$G_0(\omega) = \sum_{i=1}^M \frac{a_i}{\omega^+ - b_i}, \quad (87)$$

thereby effectively discretizing the conduction electron bath. Note that, here a_i are the residues corresponding to the poles b_i which have to be normalized according to $\sum a_i = 1$. Then We divide the poles into N groups of size n ($Nn=M$):

$$G_0(\omega) = \frac{1}{N} \sum_{\nu=1}^N \sum_{i=1}^n \frac{a_i^\nu}{\omega^+ - b_i^\nu} = \frac{1}{N} \sum_{\nu} G_0^\nu(\omega), \quad (88)$$

where n is a relatively small integer number that ultimately determines the size of the finite AIM, and N stands for the number of groups, the number of finite-size Anderson models in the ensemble. Now the residues in *each group* have to be normalized as well, i.e. $\sum_{i=1}^n a_i^\nu = 1$ for all $\nu = 1 \dots N$.

The poles representing $G_0(\omega)$ are generated randomly using the non-interacting spectral density $\rho_0(\omega) = -\text{Im}[G_0(\omega)]/\pi$ as the probability distribution. As we picked up a flat hybridization, then the corresponding non-interacting spectral density is a Lorentzian function:

$$\rho_0(\omega) = \frac{\Gamma/\pi}{\omega^2 + \Gamma^2} \quad (89)$$

Hence, each set ν of n randomly chosen poles uniquely defines the non-interacting part of a finite-size Anderson model:

$$\begin{aligned} H_0^\nu &= \epsilon_0^\nu \sum_{\sigma} d_{\sigma}^{\dagger} d_{\sigma} + \sum_{\sigma, k=1}^{n-1} V_k^\nu (d_{\sigma}^{\dagger} c_{k\sigma} + c_{k\sigma}^{\dagger} d_{\sigma}) \\ &+ \sum_{\sigma, k=1}^{n-1} \epsilon_k^\nu c_{k\sigma}^{\dagger} c_{k\sigma}. \end{aligned} \quad (90)$$

The mapping from the set of poles to the parameters of the finite Anderson model is achieved by equating G_0^ν and the impurity Green's function corresponding to H_0^ν :

$$\sum_{i=1}^n \frac{a_i^\nu}{\omega^+ - b_i^\nu} = \left(\omega - \epsilon_0^\nu - \sum_{k=1}^{n-1} \frac{(V_k^\nu)^2}{\omega^+ - \epsilon_k^\nu} \right)^{-1}, \quad (91)$$

where the residues are taken to be constant with $a_i^\nu = 1/n$. Note that since the poles b_i^ν are chosen to be distributed randomly according to the probabilities $\rho_0(b_i^\nu)$, the seemingly reasonable choice $a_i^\nu \sim \rho_0(b_i^\nu)$ for the residues is actually wrong as it would lead to a sampled non-interacting DOS different from $\rho_0(\omega)$.

The mapping process can be recast into the three equations to extract the finite AIM parameters: The bath energy levels ϵ_k^ν can now be found from the roots of G_0^ν ,

$$G_0^\nu(\omega = \epsilon_k^\nu) = 0 \quad \forall k = 1, \dots, n-1, \quad (92)$$

while the hoppings V_k^ν between the impurity and the bath levels are determined from the derivative of G_0^ν at the bath level energies as

$$\left. \frac{dG_0^\nu}{d\omega} \right|_{\epsilon_k^\nu} = -\frac{1}{(V_k^\nu)^2} \quad \forall k = 1, \dots, n-1. \quad (93)$$

And the impurity level energy is obtained from the mean value of sampled poles:

$$\epsilon_0^\nu = \sum_{i=1}^n a_i^\nu b_i^\nu = \frac{1}{n} \sum_{i=1}^n b_i^\nu. \quad (94)$$

By now, we successfully extracted all parameters for the non-interacting Anderson models. Then, the interacting finite Anderson model is obtained by adding the interaction part, and, importantly, subtracting out the effective one-body potential Σ_0 to avoid double counting of interaction:

$$H^\nu = H_0^\nu + U n_{d\uparrow} n_{d\downarrow} - \Sigma_0 n_d \quad (95)$$

Hence we see that Σ_0 does not really play a role yet. The role of Σ_0 will become clear later in the context of the constraint (see Sec. 3.3). For later convenience we also define the bare impurity level $\epsilon_d^\nu = \epsilon_0^\nu - \Sigma_0$ of the finite model. Note that $\epsilon_d^\nu \rightarrow \epsilon_d$ in the limit of $n \rightarrow \infty$.

The finite Anderson model Hamiltonian H^ν is now diagonalized numerically. This yields the many-body eigenstates $|m^\nu\rangle$ and the corresponding eigenenergies E_m^ν . The Green's function for the impurity level in the full interacting system is then given by the Lehmann representation:

$$G_\sigma^\nu(\omega) = \sum_m \frac{|\langle m^\nu | d_\sigma | 0^\nu \rangle|^2}{\omega^+ + E_m^\nu - E_0^\nu} + \sum_m \frac{|\langle m^\nu | d_\sigma^\dagger | 0^\nu \rangle|^2}{\omega^+ + E_0^\nu - E_m^\nu} \quad (96)$$

where $|0^\nu\rangle$ and E_0^ν denote the ground state and corresponding ground state energy. In the case of a degenerate ground state the corresponding Green's function would be obtained as,

$$G^R(\nu, \omega) = \frac{1}{N_{deg}} \sum_{n=1}^{N_{deg}} \left(\sum_m \frac{|\langle 0_n^\nu | d_\sigma | m^\nu \rangle|^2}{\omega^+ + E_m^\nu - E_{0,n}^\nu} + \sum_m \frac{|\langle m^\nu | d_\sigma^\dagger | 0_n^\nu \rangle|^2}{\omega^+ + E_{0,n}^\nu - E_m^\nu} \right) \quad (97)$$

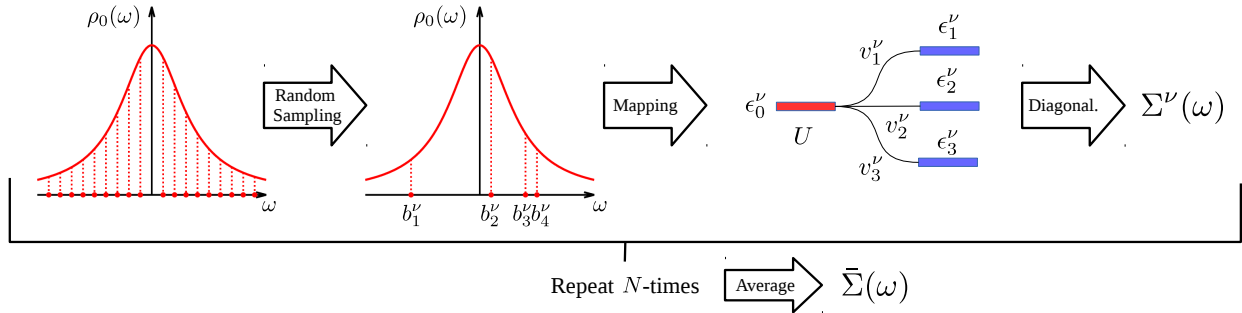


Figure 5: Schematic representation of the DED method. The non-interacting density of the impurity level $\rho_0(\omega)$ is interpreted as a probability distribution for the poles of the non-interacting Green's function $G_0(\omega)$. A finite number of poles b_i^ν is then generated randomly according to the distribution $\rho_0(\omega)$. The selected n poles uniquely define a finite Anderson model H^ν with $n - 1$ bath sites. Diagonalization of H^ν yields the self-energy $\Sigma^\nu(\omega)$ corresponding to the finite Anderson model. This process is repeated many times (N). An approximation to the self-energy of the original infinite Anderson model (1) is obtained from the ensemble average of the self-energies of the finite Anderson model samples (99).

where N_{deg} refers to the number of the number of ground state degeneracy. However, we will see in Sec.3.3 that the particle constraint ensures that the ground state is actually a singlet state. The corresponding self-energy of the finite Anderson model is

$$\Sigma_\sigma^\nu(\omega) = (G_0^\nu(\omega))^{-1} - (G_\sigma^\nu(\omega))^{-1} + \Sigma_0 \quad (98)$$

This process of generating finite Anderson model Hamiltonians H^ν and calculating their self-energies Σ^ν is repeated N times. Finally, an approximation to the self-energy of the original *infinite* Anderson model is obtained from the ensemble average

$$\bar{\Sigma}_\sigma(\omega) = \frac{1}{N} \sum_{\nu=1}^N \Sigma_\sigma^\nu(\omega) \quad (99)$$

An approximation to the corresponding interacting Green's function is obtained from $G_\sigma(\omega) = (\omega^+ - \epsilon_d - \bar{\Sigma}_\sigma(\omega) - \Delta(\omega))^{-1}$. As observed by Granath and Strand, obtaining an approximation to the Green's function of the infinite Anderson model by directly averaging the $G_\sigma^\nu(\omega)$ is not an option, since the sample-averaged interacting and non-interacting Green's functions $\bar{G}_\sigma(\omega) = \frac{1}{N} \sum_\nu G_\sigma^\nu(\omega)$ and $\bar{G}_0(\omega) = \frac{1}{N} \sum_\nu \bar{G}_\sigma^\nu(\omega)$, respectively, do not form a proper pair of interacting and non-interacting Green's functions connected by the Dyson equation.⁵⁴ Fig. 5 shows a schematic representation summarizing the main steps of the DED procedure.

3.3 Role of the constraint

In order to achieve valid spectra not all randomly generated Anderson models can be accepted. Granath and Strand introduced a constraint comparing the ground state particle numbers in the interacting and non-interacting systems. More precisely, a sample ν is only accepted if the number of particles of the ground state of the interacting model H^ν and that of the non-interacting model H_0^ν coincide, i.e.

$$N^\nu \stackrel{(!)}{=} N_0^\nu. \quad (100)$$

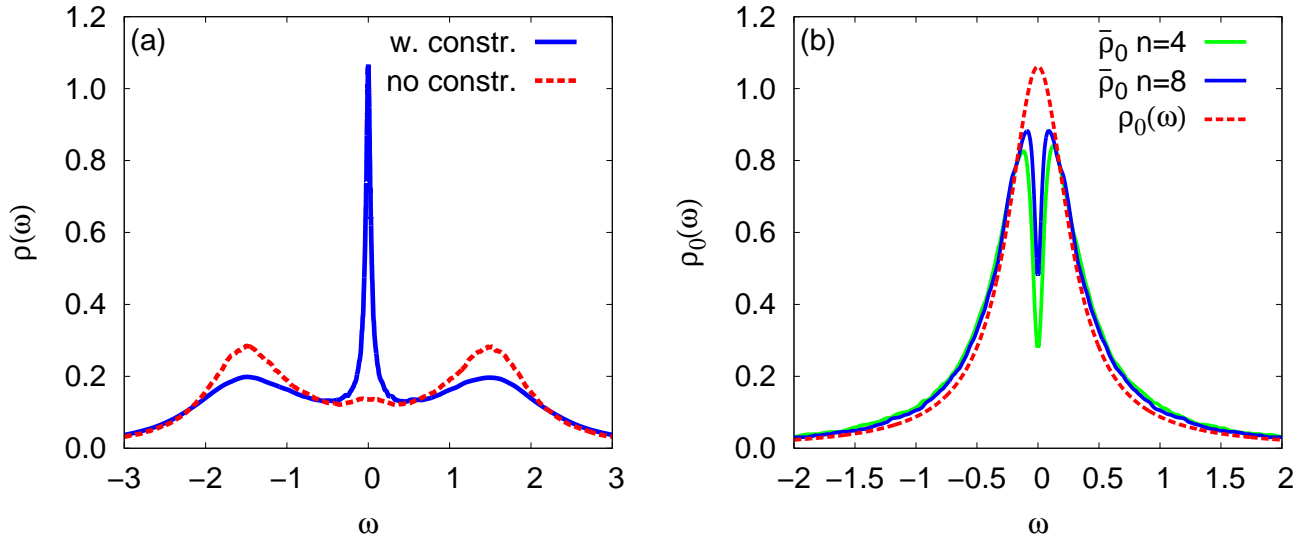


Figure 6: Effect of constraint: (a) Comparison of spectra calculated with (blue line) and without (red line) imposing the particle number constraint for $n = 4$ sites, $\Gamma = 0.3$, $U = 3$, $\epsilon_d = -U/2$. (b) Comparison of sampled non-interacting DOS $\bar{\rho}_0(\omega)$ for different number of sites with original Lorentzian non-interacting DOS $\rho_0(\omega)$.

To show the important role of the constraint, in Fig. 6a we show the spectra corresponding to the situation when all randomly generated finite Anderson model samples are equally contributing to the sample-averaged self-energy, i.e. when no constraint is imposed (red dashed line), compared to the case when only the configurations fulfilling the particle constraint contribute to the ensemble-averaged self-energy (blue line). As can be seen when no constraint is imposed there is essentially no Kondo peak and the Hubbard side peaks are overestimated, while applying the constraint, indeed recovers the full height of the Kondo peak at the Fermi level and lowers the Hubbard side peaks. According to the Fermi liquid theory and the Friedel sum rule, for the flat wide band limit, the impurity spectral density at the Fermi level⁸ is as:

$$\rho_{d,\sigma}(\epsilon_F) = \frac{\sin^2(\pi \langle n_{d,\sigma} \rangle)}{\pi \Gamma}. \quad (101)$$

This is an exact expression, which interestingly is independent of the interaction U . For the particle hole (ph) symmetric case, the impurity spectral density at the Fermi energy coincides exactly with the height of the Kondo peak, and the occupancy of the impurity level per spin is $1/2$, so that,

$$\rho_{d,\sigma}(\epsilon_F) = \frac{1}{\pi \Gamma}. \quad (102)$$

The effect of the constraint on the sampled non-interacting density of states is shown in Fig. 6b. The effect is to deplete the density of states around the Fermi level. As the number of sites n increases, the effect of the constraint become less important. As already can be noticed the role of the constraint is very crucial to capture the Kondo physics correctly. Now, in the following, we elaborate the physical interpretation of it. Recalling the particle constraint, the sample ν is accepted, if the ground state particle number of the interacting system N^ν coincides with the ground state particle number in the

non-interacting system N_0^ν . For each finite size sample we have:

$$N^\nu = n_{imp}^\nu + n_{bath}^\nu \quad (103)$$

$$N_0^\nu = n_{imp,0}^\nu + n_{bath}^\nu \quad (104)$$

where the contribution of the isolated bath (which is not connected to the impurity) to the total particle numbers is

$$n_{bath}^\nu = -\frac{1}{\pi} \int_{-\infty}^{\epsilon_F} d\omega \sum_k \frac{1}{\omega^+ - \epsilon_k^\nu}. \quad (105)$$

Since, the isolated bath levels are exactly the same in both cases eq.(103) and eq.(104), the pure bath contribution to the total particle number n_{bath}^ν is the same for both the interacting and non-interacting system. Hence, the constraint imposes that the *impurity charge* be the same in the interacting and non-interacting case, i.e.:

$$n_{imp}^\nu = n_{imp,0}^\nu \quad (106)$$

The impurity charge consists of the impurity level occupancy, n_d^ν plus the additional charge induced in the conduction electrons (i.e. bath levels) by the scattering due to the presence of the impurity level, δn_{imp}^ν :

$$n_{imp}^\nu = n_{d,\sigma}^\nu + \delta n_{imp}^\nu = -\frac{1}{\pi} \text{Im} \int_{-\infty}^{\epsilon_F} d\omega (G_d^\nu(\omega) + \sum_k g_k^\nu(\omega) T_{kk}^\nu(\omega) g_k^\nu(\omega)) \quad (107)$$

where $g_k^\nu = \frac{1}{\omega^+ - \epsilon_k^\nu}$ is the propagator for the isolated bath level k , and $T_{kk}^\nu(\omega) = V_k^\nu G_d^\nu(\omega) V_k^\nu$ is the scattering T-matrix. Note that in the case of a flat wide band limit, the scattering induced charge δn_{imp}^ν vanishes.⁸ However, here we are considering a small finite number of bath levels, thus this contribution becomes indeed very important. To further elucidate this we now consider Friedel's sum rule for the Anderson model. According to that the impurity charge, n_{imp} is connected to the scattering phase shift at the Fermi level $n_{imp} = \eta(\epsilon_F)/\pi$.⁸ For a finite Anderson model sample ν we can write:

$$n_{imp,\sigma}^\nu = \eta_\sigma^\nu(\omega)/\pi \quad (108)$$

where the scattering phase shift of the interacting system is given by,

$$\eta_\sigma^\nu(\omega) = \frac{\pi}{2} - \tan^{-1} \left(\frac{\omega - \epsilon_d^\nu - \text{Re} \Sigma_\sigma^\nu(\omega) - \text{Re} \Delta^\nu(\omega)}{\text{Im} \Sigma_\sigma^\nu(\omega) + \text{Im} \Delta^\nu(\omega)} \right). \quad (109)$$

Hence it becomes immediately clear, that the particle constraint which is imposing the same impurity charge to the interacting system and the non-interacting system, is ultimately equivalent to enforcing the same phase shift to the interacting system and the corresponding non-interacting one, i.e.,

$$n_{imp,\sigma}^\nu = \frac{\eta_\sigma^\nu(\epsilon_F)}{\pi} \stackrel{constr.}{=} n_{imp,\sigma,0}^\nu = \frac{\eta_{\sigma,0}^\nu(\epsilon_F)}{\pi} \quad (110)$$

where the phase shift of the non-interacting system is given by,

$$\eta_{0,\sigma}^\nu(\omega) = \frac{\pi}{2} - \tan^{-1} \left(\frac{\omega - \epsilon_0^\nu - \text{Re} \Delta^\nu(\omega)}{\text{Im} \Delta^\nu(\omega)} \right), \quad (111)$$

Note that the hybridization function of the sample ν , $\Delta^\nu(\omega)$ describing the coupling of the impurity level to the bath levels, is according to:

$$\Delta^\nu(\omega) = \sum_k |V_k^\nu|^2 g_k^\nu(\omega) = \sum_k \frac{|V_k^\nu|}{\omega^+ - \epsilon_k^\nu}. \quad (112)$$

with $\omega^+ = \omega + i\delta$ where δ is a positive infinitesimal. Let us now have a closer look onto how the constraint acts on individual samples. We define the effective level as $\epsilon'_0 = \epsilon'_d + \Sigma_0$. In the expression for the non-interacting system eq.(111) we take the limit of $\delta \rightarrow 0$. The denominator $\text{Im } \Delta^\nu(\epsilon_F) = -\delta \sum_k \frac{|V_k|^2}{(\epsilon_F - \epsilon_k)^2 + \delta^2}$ is always negative for positive δ and goes to zero for $\delta \rightarrow 0$ unless, $\epsilon_k = \epsilon_F$. Hence depending on the sign of the numerator the \tan^{-1} argument tends to $-\infty$, ∞ or zero. So that, for finite systems the phase shift can only have three different values:

$$\eta'_0(\epsilon_F) \rightarrow \begin{cases} 0 & ; & \text{for } \epsilon_F - \epsilon_0 - \text{Re } \Delta^\nu(\epsilon_F) < 0 \\ \pi/2 & ; & \text{for } \epsilon_F - \epsilon_0 - \text{Re } \Delta^\nu(\epsilon_F) = 0 \\ \pi & ; & \text{for } \epsilon_F - \epsilon_0 - \text{Re } \Delta^\nu(\epsilon_F) > 0 \end{cases}$$

The sign of the numerator is determined by the position of the effective level $\tilde{\epsilon}_0^\nu = \epsilon'_0 + \text{Re } \Delta^\nu(\tilde{\epsilon}_0^\nu)$. The effective level is the most important excitations from the Fermi level. If $\tilde{\epsilon}_0^\nu$ happens to be below the Fermi level, then it is hole excitation so that, the numerator $\epsilon_F - \epsilon_0 - \text{Re } \Delta^\nu(\epsilon_F)$ is negative, and consequently the phase shift is zero. Conversely, if $\tilde{\epsilon}_0^\nu$ lies above the Fermi level there is a particle excitation, then the numerator $\epsilon_F - \epsilon_0 - \text{Re } \Delta^\nu(\epsilon_F)$ is positive, and hence the phase shift is π . A phase shift $\pi/2$ is theoretically also possible (implying $n_{imp} = 1$) but in practice it does not happen. This situation can occur when the effective level $\tilde{\epsilon}_0^\nu$ sits right at the Fermi level, or when two effective levels are at exactly the same distance from the Fermi level, one below and one above. Thus the numerator becomes zero, and accordingly the phase shift is $\pi/2$.

Hence during the DED procedure the phase shift of individual samples will fluctuate between these two values 0 and π . In the ph-symmetric situation ($\epsilon_d = -U/2$) the probability of samples with phase shift 0 will be equal to the samples with phase shift π for a large enough number of samples. Hence on average we have a phase shift of $\pi/2$ as required in that situation. Away from ph symmetry, the number of samples with one phase grows on the expense of samples with other phase shifts, so that the average phase shift becomes different from $\pi/2$.

Similar to the non-interacting case, also in the interacting case the phase shift oscillates between the three values, 0, $\pi/2$ and π , depending on the sign of the numerator $\epsilon_F - \epsilon'_d - \text{Re } \Sigma^\nu(\epsilon_F) - \text{Re } \Delta^\nu(\epsilon_F)$ in eq. 109 since the denominator $\text{Im } \Sigma^\nu(\epsilon_F) - \text{Im } \Delta^\nu(\epsilon_F) \propto \delta$

$$\eta^\nu(\epsilon_F) \rightarrow \begin{cases} 0 & ; & \text{for } \epsilon_F - \epsilon'_d - \text{Re } \Sigma^\nu(\epsilon_F) - \text{Re } \Delta^\nu(\epsilon_F) < 0 \\ \pi/2 & ; & \text{for } \epsilon_F - \epsilon'_d - \text{Re } \Sigma^\nu(\epsilon_F) - \text{Re } \Delta^\nu(\epsilon_F) = 0 \\ \pi & ; & \text{for } \epsilon_F - \epsilon'_d - \text{Re } \Sigma^\nu(\epsilon_F) - \text{Re } \Delta^\nu(\epsilon_F) > 0 \end{cases}$$

Also in the interacting case the sign of the numerator can be related to the position of effective quasi-particle (QP) levels $\tilde{\epsilon}'_d = \epsilon'_d - \text{Re } \Sigma^\nu(\epsilon_F) - \text{Re } \Delta^\nu(\epsilon_F)$ with respect to the Fermi level. The point is that by construction in the non-interacting case all poles of the impurity Green's function have the same residue, i.e. all QP levels have the same weight while in contrast to the non-interacting case we have to take into account that the QPs are renormalized, so in principle they can have different weights. Therefore, $\tilde{\epsilon}'_d$ in the interacting case is not simply the nearest quasi particle level to the Fermi level, but rather the most important one, taking also into account its weight (or residue). The most important one should be given by the pole in the interacting Green's function with the largest ratio between pole and residue.

Now just as in the non-interacting case, if the effective energy level $\tilde{\epsilon}'_d$ of the most important QP, lies below the Fermi level (hole excitation) the numerator $\epsilon_F - \epsilon'_d - \text{Re } \Sigma^\nu(\epsilon_F) - \text{Re } \Delta^\nu(\epsilon_F)$ is negative, and

we get a phase shift of 0, and if $\tilde{\epsilon}_d^\nu$ lies above the Fermi level (particle excitation), then the numerator becomes positive, and the phase shift is π . In the situation where the numerator becomes exactly zero we either have a QP exactly at the Fermi level or two equally important QPs above and below the Fermi level, leading to a phase shift of $\pi/2$. The latter situation is not very unlikely especially for the two site(level) model (one impurity and one bath level) thus we have $n_{imp} = 1$. But then the particle constraint can not be fulfilled as in the non-interacting system we either have $n_{imp} = 0$ or $n_{imp} = 2$.

Hence we can see that the particle constraint, by demanding that the interacting system has the same phase shift as the non-interacting one, ultimately requires that the type of the most important excitation, (i.e. hole-like or particle-like) be the same in the interacting and non-interacting systems. This is illustrated in Fig. 7 which compares the spectra of an interacting and non-interacting finite Anderson model in the case that the constraint is not fulfilled (a) and when it is fulfilled (b). One can clearly see that the main excitations are not of the same type when the constraint is not fulfilled, while they are of the same type if the constraint is fulfilled. Clearly, in the latter case a 1:1 correspondence can be established between the excitations of the interacting and corresponding non-interacting system. Hence the constraint guarantees that only self-energies $\Sigma_\sigma^\nu(\omega)$ which have the same phase shift as the corresponding non-interacting model contribute to the ensemble average (99). A closer look at the phase shifts η_σ^ν and $\eta_{0,\sigma}^\nu$ of individual finite Anderson model samples ν further reveals that the constraint really establishes a 1:1 correspondence between the excitations of the interacting Hamiltonian H^ν and the corresponding non-interacting one H_0^ν , as required by Fermi liquid theory. When the constraint is not fulfilled, the 1:1 correspondence with the non-interacting system cannot be established, because the ground state of the interacting system has an odd number of electrons ($N^\nu = N_0^\nu \pm 1$) and thus is a doublet state ($S = 1/2$), while the non-interacting system must have an even number of electrons (single-particle levels are either doubly occupied or unoccupied), and thus has a singlet ground state ($S = 0$). Thus the constraint ultimately enforces that individual Anderson model samples contributing to the self-energy average (99) comply with Nozieres' Fermi liquid picture⁶⁶ of the Kondo effect in the strong coupling regime: the impurity spin locks into a total spin singlet state with a few conduction electron bath levels, and the remaining conduction electrons interact weakly with the singlet state, thus leading to Fermi liquid behavior. Since Friedel's sum rule is directly related to the height of the Kondo peak at the Fermi energy, the particle constraint ultimately leads to the recovery of the unitary limit for the interacting spectral function, and consequently to the recovery of Fermi-liquid behavior.

The effective potential Σ_0 included in the non-interacting Green's function (86) enters in the constraint: Since $\epsilon_0^\nu = \epsilon_d^\nu + \Sigma_0$ it determines the phase shift $\eta_{0,\sigma}^\nu(\epsilon_F)$ and consequently the impurity charge $n_{imp,\sigma,0}^\nu$ of the non-interacting reference system. as the corresponding non-interacting model contribute to the ensemble average (99). The interpretation of the constraint as a sample-wise enforcement of Fermi liquid behavior suggests that the parameter Σ_0 should be interpreted as an effective one-body potential that can be identified with the real part of the (yet to be determined) many-body self-energy:

$$\Sigma_0 \equiv \text{Re} \bar{\Sigma}(\epsilon_F) \quad (113)$$

This conjecture can be further justified by considering the exact limit of the DED approach: taking the number of poles $n \rightarrow \infty$, the original infinite Anderson model is recovered. Since now there is only one sample, the constraint must be fulfilled for this one sample, hence the phase shift of the interacting

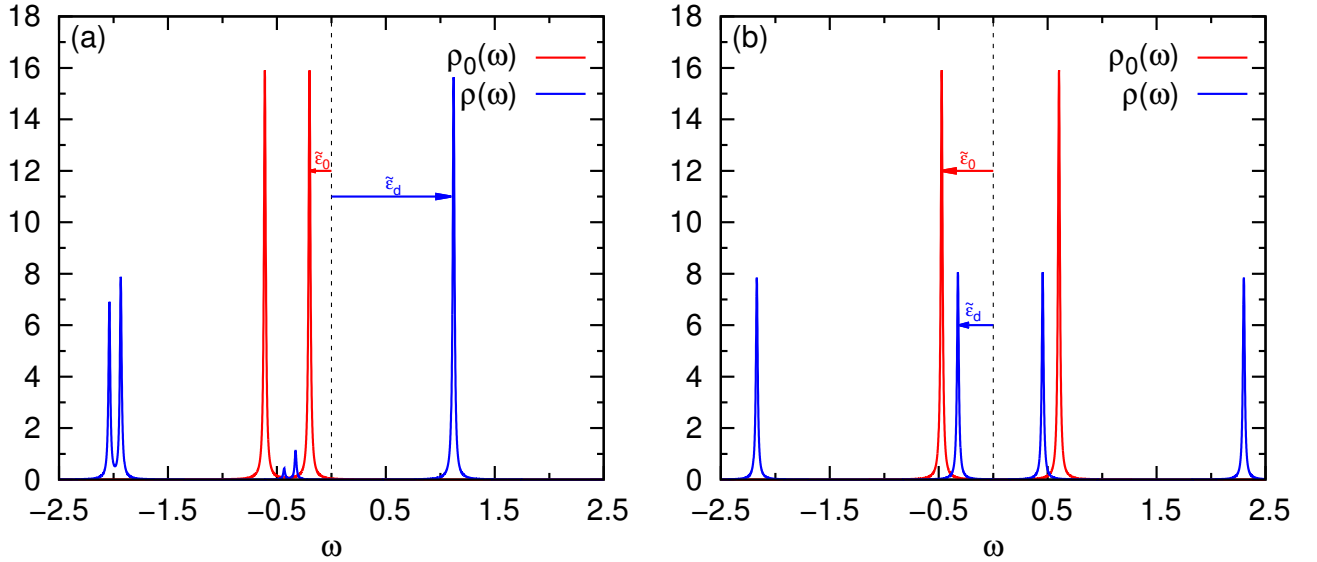


Figure 7: Comparison of the non-interacting and interacting finite Anderson model spectra for the case that the particle constraint is not fulfilled (a) and is fulfilled (b).

and corresponding non-interacting model must match exactly, leading to:

$$\tan^{-1} \left(\frac{\epsilon_d + \text{Re} \Sigma(\epsilon_F) - \epsilon_F}{\Gamma} \right) \stackrel{(!)}{=} \tan^{-1} \left(\frac{\epsilon_d + \Sigma_0 - \epsilon_F}{\Gamma} \right) \quad (114)$$

which implies $\Sigma_0 \equiv \text{Re} \bar{\Sigma}(\epsilon_F)$.

Since the self-energy itself is not known prior to the calculation, Σ_0 has to be determined self-consistently, starting with some initial guess for Σ_0 , for example the Hartree shift $\Sigma_0 \equiv U n_d / 2$ with n_d being the Hartree-Fock occupancy. This is where our approach slightly differs from the one originally proposed by Granath and Strand. There Σ_0 was introduced as an effective chemical potential which is equal to $U/2$ for the symmetric situation and away from the ph symmetry is an adjustable parameter to be fixed by demanding that the interacting and non-interacting impurity occupancy n_d be the same.

4 Zero temperature results

In the following we present results for the AIM described by eq. (1), assuming a constant hybridization function $\Delta(\omega) = -i\Gamma$. The non-interacting density of states $\rho_0(\omega)$ is thus a Lorentzian centered at $\epsilon_d + \Sigma_0$ of width 2Γ . To resolve the interacting spectral functions we use a logarithmic mesh, and a frequency dependent Lorentzian broadening scheme where an imaginary part proportional to the frequency is added to the frequency argument in the denominators of the Green's functions, i.e. $\omega^+ = \omega + i\eta_1 \cdot |\omega|$ with $\eta_1 = 0.02$. For all cases Numerical renormalization Group (NRG), a numerically exact method is used as a benchmark.

4.1 Symmetric Anderson model

First we study the AIM at particle-hole symmetry, $\epsilon_d = -U/2$ and $\langle n_d \rangle = 1$. In this case the real part of the self-energy at the Fermi level is known prior to calculation, $\Sigma_0 = U/2$, and hence does not have to be determined self-consistently. Fig. 8a shows the impurity spectral function $\rho(\omega) = -\text{Im}G(\omega)/\pi$ for $U = 3$ and $\Gamma = 0.3$ calculated by DED with $n = 8$ sites, in comparison with the NRG spectrum. The DED and NRG spectra are in excellent overall agreement. The Anderson model is in the Kondo regime, where the spectral function is characterized by three resonances: The sharp Kondo resonance at the Fermi level and two Hubbard side peaks on either side of the Fermi level close to the excitation energies ϵ_d and $\epsilon_d + U$. In Fig. 8b, we show DED spectra for different numbers of sites n in comparison with NRG for the same set of parameters as in Fig. 8a. In order to better resolve the spectra at low energies, the energies are plotted on a logarithmic scale. Even for very small models ($n = 2$) there is good qualitative agreement with the NRG spectrum, but the width of the Kondo peak is overestimated roughly by a factor of 2 (see also Fig. 10b), and the height of the Hubbard side peaks is slightly underestimated. Note, however, that the height of the Kondo peak $1/\pi\Gamma$ (eq. (102)) is always exact, independent of the number of sites n , since it is imposed by the particle constraint, as discussed in Sec. 3.3. As the number of sites n increases, the quantitative agreement with NRG improves considerably, becoming excellent for $n = 8$ sites. The quantitative improvement with increasing number of sites can also be seen in Fig. 10b, where we show the half-width of the Kondo peak as a function of the model size n in comparison to the NRG value.

The number of randomly generated samples contributing to the ensemble average of the self-energy (99) generally determines the amount of noise in the spectra. By increasing the number of samples N the noise can be reduced, and vanishes in the limit $N \rightarrow \infty$. On the other hand, the larger the number of sites n of the finite size Anderson models, the fewer samples are needed to achieve the same level of noise, since the number of poles in the spectrum of individual samples increases. For example, in Fig. 8b for $n = 2, 4, 8$ sites about 5.8×10^4 , 3.6×10^4 and 1.7×10^4 samples, respectively, were used to generate the spectra. Obviously, in the (theoretical) limit of the original infinite Anderson model ($n \rightarrow \infty$) there would be only one sample which would yield an exact and thus noiseless spectrum. In Table. 2 we report the number of samples used for calculating the spectra shown in Figs. 8-12.

Next we investigate how the quality of the DED spectra changes when the correlation strength controlled by U/Γ is altered. In Fig. 9a,b we show a comparison of spectra calculated by DED and NRG for higher values of the broadening Γ than before. For weak correlation strength ($\Gamma = 0.9$, Fig. 9a), the system is no longer in the Kondo regime: the spectra are characterized by a single peak,

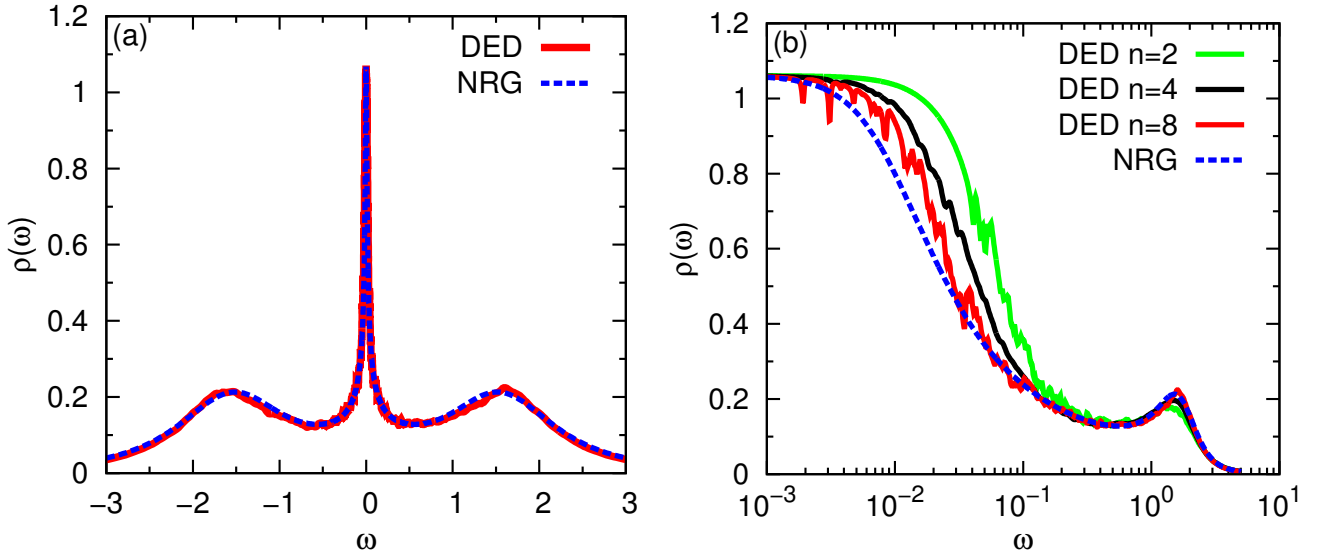


Figure 8: Comparison between DED and NRG spectra for the symmetric Anderson model ($U = 3$ and $\epsilon_d = -1.5$). (a) DED ($n = 8$) and NRG spectra for $\Gamma = 0.3$. (b) NRG and DED with different number of sites n on a half-log scale for $\Gamma = 0.3$.

though different from the Lorentzian of the non-interacting system due to interaction effects. Here the agreement with NRG is excellent already for $n = 2$ (not shown). As the correlation strength increases, more sites are necessary to achieve good quantitative agreement. For $\Gamma = 0.5$ (Fig. 9b), we approach the Kondo regime, and the three peak structure starts to emerge. Now excellent quantitative agreement with NRG can be achieved for $n = 6$ sites. We have already discussed the case $\Gamma = 0.3$ (Figs. 8a,b and Fig. 10b), already in the Kondo regime, where excellent agreement with NRG is reached for $n = 8$ sites. Figures 9c,d show DED spectra in comparison with NRG for $\Gamma = 0.2$, on a normal energy scale (Fig. 9c), and on a logarithmic energy scale (Fig. 9d) for better resolution of the low-energy features. The overall qualitative agreement with the NRG spectrum is again quite good, as can be seen from Fig. 9c. However, the quantitative agreement, especially of the low energy features, i.e. the Kondo peak, is not very good anymore: the width of the Kondo peak is still strongly overestimated by almost a factor of 2 even for $n = 8$ sites. The high energy features on the other hand are captured quite well, although the height of the Hubbard side peaks is slightly overestimated.

This behavior of decreasing quality of the DED at a fixed number of sites with increasing correlation strength U/Γ is summarized in Fig. 10a which shows the half-width of the Kondo peak as a function of Γ , comparing DED for $n = 8$ sites, NRG and an exact expression.⁶⁷ For not too strong correlations up to $\Gamma \geq 0.3$ ($U/\Gamma \leq 10$), DED for $n = 8$ sites yields an excellent approximation to the width of the Kondo peak, but begins to deviate from NRG as the correlations become stronger (decreasing Γ). For very strong correlations (i.e. $U/\Gamma \gg 10$), the width of the Kondo peak becomes strongly overestimated, by orders of magnitude (see also Fig. 9c and Fig. 9d). This behavior can be understood by considering the Kondo screening cloud, whose spatial extension grows exponentially with increasing correlation strength.⁶⁸ $\xi_K \propto 1/T_K \propto e^{\Gamma/U}$. Thus the number of bath sites necessary to correctly describe the Kondo screening cloud grows exponentially with the correlation strength, leading generally to an overestimation of the Kondo temperature for too small bath sizes. Hence for very strong correlation

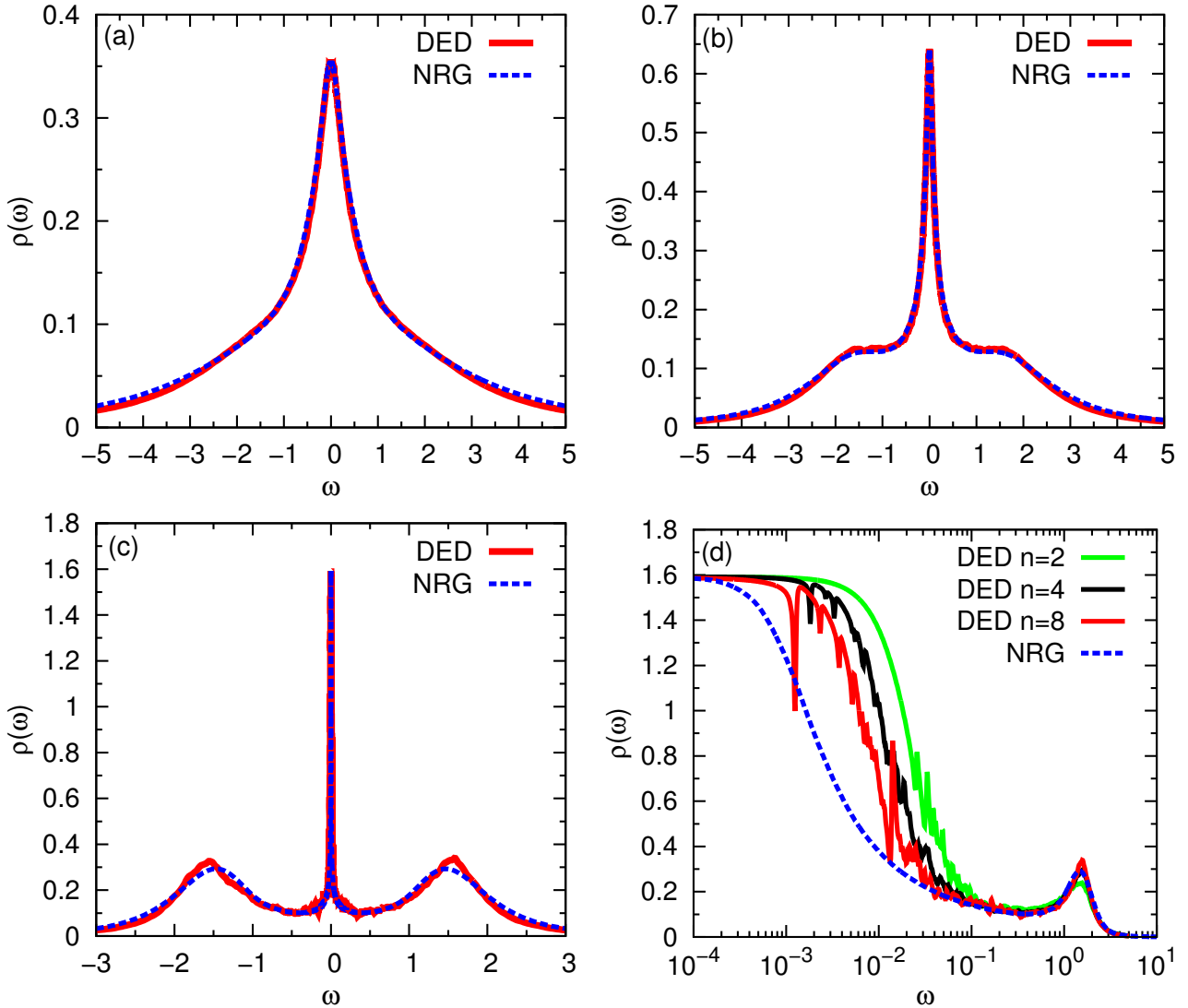


Figure 9: Comparison between DED and NRG spectra for the symmetric Anderson model. ($U = 3$, $\epsilon_d = -1.5$) (a) DED ($n = 6$) and NRG spectra for $\Gamma = 0.9$. (b) DED ($n = 6$) and NRG spectra for $\Gamma = 0.5$. (c) DED ($n = 8$) and NRG spectra for $\Gamma = 0.2$. (d) NRG and DED for different number of sites n on a half-log scale for $\Gamma = 0.2$.

strengths the DED method cannot provide a quantitatively satisfactory description of the spectra with a computationally feasible number of bath sites. Yet for correlation strengths up to and including $U/\Gamma \approx 10$ DED yields an excellent description of the spectra for small to moderate numbers of bath sites.

4.2 Asymmetric Anderson model

We now consider the AIM away from particle-hole symmetry, $\epsilon_d < -U/2$ and $\langle n_d \rangle > 1$. As explained before in Sec. 3.3, the parameter Σ_0 has to be determined self-consistently since we identified it with the real part of the self-energy at the Fermi level, $\Sigma_0 \equiv \text{Re} \bar{\Sigma}(\epsilon_F)$ which is unknown prior to the DED calculation. We thus start with some reasonable initial guess, for example the Hartree shift $\Sigma_0 \equiv U \langle n_d \rangle / 2$, calculated within Hartree-Fock, $\Sigma_0 \equiv U/2$, or simply $\Sigma_0 \equiv -\epsilon_d$. Using this Σ_0 in the

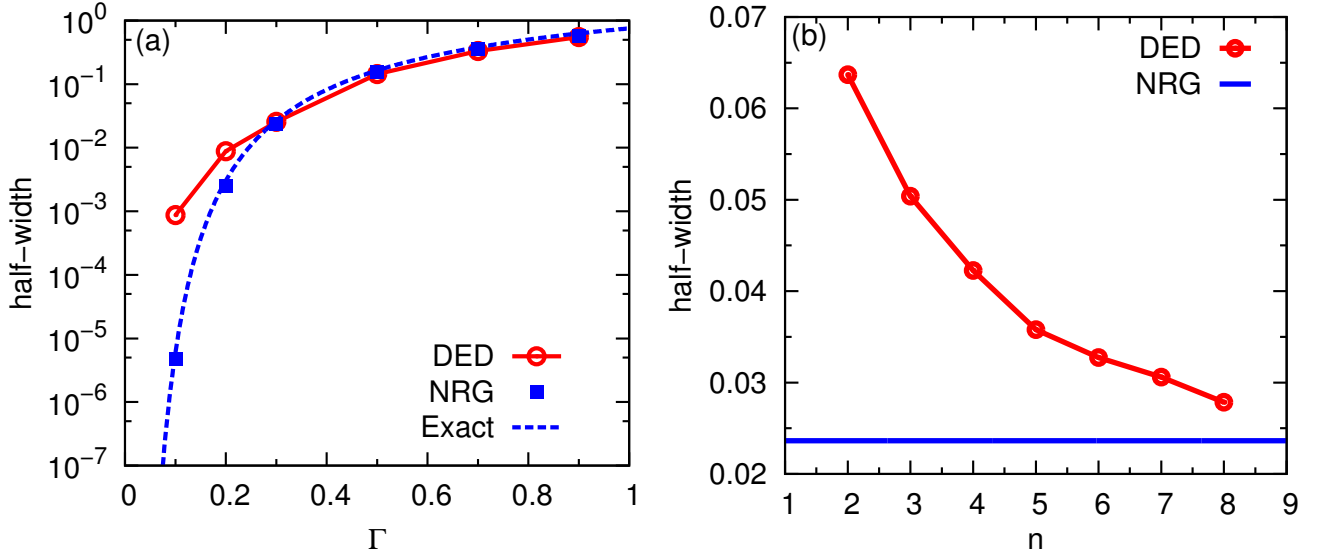


Figure 10: Comparison between DED and NRG spectra for the symmetric Anderson model ($U = 3$ and $\epsilon_d = -1.5$). (a) Half-width of Kondo peak estimated by fitting with Frota line shapes⁶⁹ versus Γ calculated by DED ($n = 8$ for $\Gamma \leq 0.3$ and $n = 6$ for $\Gamma \geq 0.5$) compared to NRG and the exact expression on half-log scale. (b) Half-width of Kondo peak versus number of sites n compared to NRG for $\Gamma = 0.3$.

DED procedure we calculate the self-energy $\bar{\Sigma}^{(1)}(\omega)$ and thus obtain a new guess for $\Sigma_0 \rightarrow \text{Re } \bar{\Sigma}^{(1)}(\omega)$, and repeat until self-consistency is reached. This procedure usually converges within a few cycles (2-4) to an accuracy of under 1%. We find that the effect of the self-consistency on the overall spectrum is relatively small. The main effect is to improve the position of the Kondo peak and to recover the exact height of the Kondo peak. Hence if the fine details of the spectrum are less important, it suffices to compute $\bar{\Sigma}(\omega)$ for some reasonable guess, for example $\Sigma_0 = U/2$. More details on the self-consistent determination of Σ_0 can be found in the following section.

In Fig. 11a we show the impurity spectral density for $U = 3$, $\Gamma = 0.3$ and $\epsilon_d = -2$, calculated by DED for $n = 8$ sites in comparison with the NRG spectrum. The DED spectrum is in very good overall agreement with the NRG spectrum. For as much as we are in the Kondo regime the three peak structure is retained (see Sec. 4.1). As in the symmetric case, in order to better resolve the spectra at low energies, we use a logarithmic scale for the energy axis. Since here we are dealing with asymmetric spectra, we represent the spectral density on the logarithmic scale for negative and positive energies in Fig. 11c and Fig. 11d, respectively. As in the ph-symmetric case, we observe quantitative improvement of the DED spectra with increasing n . Especially the position and height of the Kondo peak improve considerably: While for small n the peak is considerably offset from the Fermi level, the pinning of the Kondo peak to the Fermi level as seen in NRG is almost completely recovered for $n = 8$. As can be seen from Fig. 11b, similar to the symmetric case (see Sec. 4.1), the width of the Kondo peak is strongly overestimated for $n = 2$ by almost a factor of 3, but decreases rapidly with increasing n , until for $n = 8$ the width is only slightly overestimated by a few percent.

Next we investigate the quality of the DED spectra when moving away from the Kondo regime, by further decreasing ϵ_d such that $\epsilon_d + U$ approaches the Fermi level. In Figs. 12a,b we compare spectra

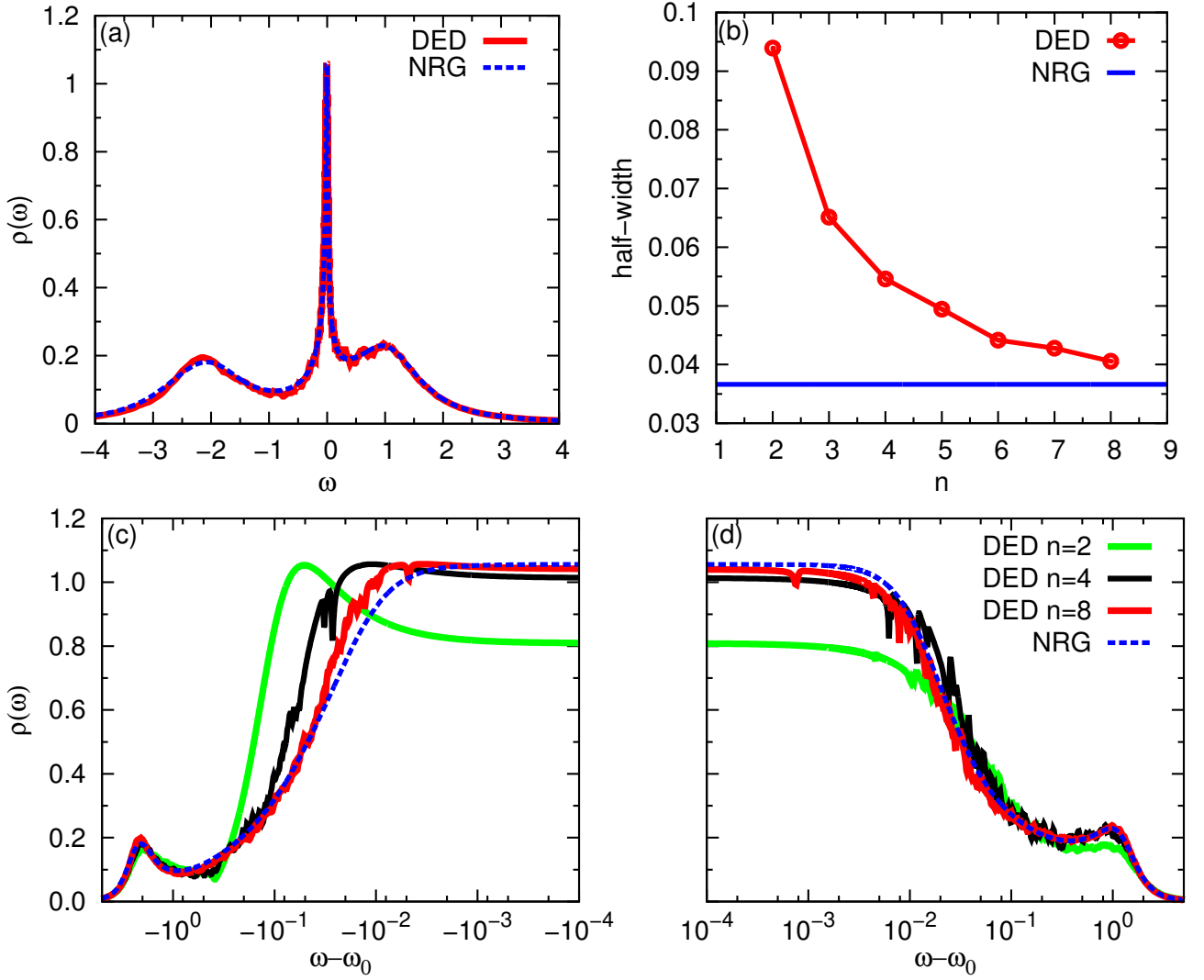


Figure 11: Comparison between DED and NRG spectra for the asymmetric Anderson model ($U = 3$, $\epsilon_d < -1.5$, $\Gamma = 0.3$). (a) DED (for $n = 8$ sites) and NRG spectra for $\epsilon_d = -2$. (b) Half-width of Kondo peak versus number of sites n compared to NRG ($\epsilon_d = -2$). (c) NRG and DED spectra with different number of sites n for $\epsilon_d = -2$ on a half-log scale for negative energies. (d) NRG and DED spectra with different number of sites n for $\epsilon_d = -2$ on a half-log scale for positive energies.

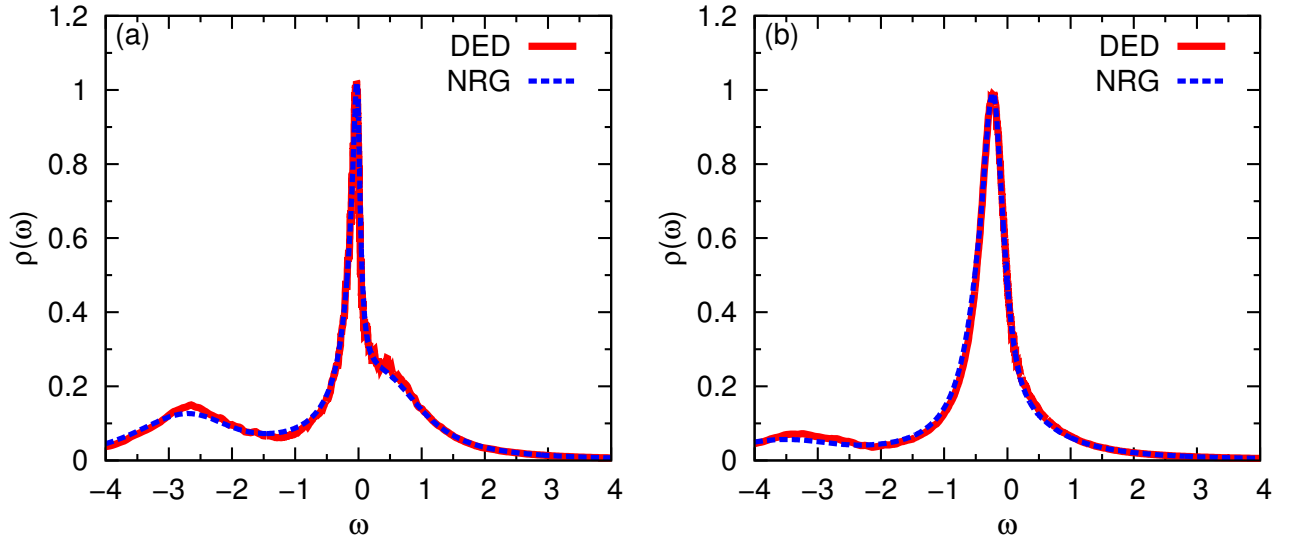


Figure 12: Comparison between DED and NRG spectra for the asymmetric Anderson model ($U = 3$, $\epsilon_d < -1.5$, $\Gamma = 0.3$). (a) DED (for $n = 8$ sites) and NRG spectra for $\epsilon_d = -2.5$. (b) DED (for $n = 8$ sites) and NRG spectra for $\epsilon_d = -3$.

ϵ_d	NRG	DED (ENS)	DED (FSR)	Σ_0
-1.5	1.0000	0.9992 ± 0.0062	1.0080 ± 0.068	1.496 ± 0.032
-1.65	1.0202	1.0234 ± 0.0063	1.0398 ± 0.062	1.630 ± 0.030
-1.8	1.0420	1.0495 ± 0.0066	1.0646 ± 0.056	1.769 ± 0.027
-2.0	1.0765	1.0862 ± 0.0089	1.1315 ± 0.055	1.937 ± 0.027
-2.5	1.2322	1.2370 ± 0.0110	1.2970 ± 0.030	2.349 ± 0.019
-3.0	1.5270	1.5450 ± 0.0150	1.5280 ± 0.014	2.673 ± 0.014

Table 1: The d -level occupancy $\langle n_d \rangle$ calculated by NRG compared to DED obtained (i) via the ensemble average (ENS) and (ii) via Friedel's sum rule (FSR) from $\text{Re} \bar{\Sigma}(\epsilon_F)$ as well as the self-consistently determined $\Sigma_0 = \text{Re} \bar{\Sigma}(\epsilon_F)$ for different values of ϵ_d and their statistical errors.

calculated by DED (for $n = 8$ sites) and by NRG in the intermediate valence regime $\epsilon_d + U - \epsilon_F \approx \Gamma$. In this regime the charge of the impurity level fluctuates strongly between single and double occupation, leading to a significant deviation of $\langle n_d \rangle$ from unity. The spectral density is characterized by two resonances, one at $\approx \epsilon_d + U$ of width $\approx \Gamma$, and a much less pronounced resonance at ϵ_d . Upon further decreasing ϵ_d the resonance at ϵ_d becomes more strongly suppressed (compare Fig. 12b with Fig. 12a), as we get closer to the non-magnetic regime ($\epsilon_d + U - \epsilon_F \ll -\Gamma$) where the impurity level is almost doubly occupied, and the resonance finally vanishes (not shown). As can be seen from Figs. 12a,b, the DED spectra are in excellent agreement with the NRG ones even for strong asymmetry, capturing all the described features very well.

Finally, we also calculate the occupancy of the impurity level $\langle n_d \rangle$ for different values of ϵ_d and compare with NRG. We investigate two different ways of calculating $\langle n_d \rangle$ within DED. On the one hand we can calculate the the occupancy from the ensemble average (ENS) over accepted finite Anderson

model samples:

$$\langle n_d \rangle \approx \bar{n}_d = \frac{1}{N} \sum_{\nu} \langle 0^{\nu} | n_d | 0^{\nu} \rangle \quad (115)$$

On the other hand we can make use of Friedel's sum rule (FSR), and calculate $\langle n_d \rangle$ from the self-energy at the Fermi level:

$$\langle n_d \rangle = 1 - \frac{2}{\pi} \tan^{-1} \left(\frac{\epsilon_d + \text{Re} \bar{\Sigma}(\epsilon_F) - \epsilon_F}{\Gamma} \right) \quad (116)$$

where we have already taken into account spin-degeneracy. Also note that $n_{\text{imp}} = \langle n_{d,\sigma} \rangle$, in the flat wide band limit.⁸ Table 1 shows the results for NRG and DED using $n = 8$ sites. The overall agreement between DED and NRG is very good. The values of $\langle n_d \rangle$ calculated by both approaches in DED agree with the NRG results within the statistical error for all values of ϵ_d . The statistical errors of the ensemble-averaged occupancy and of Σ_0 were estimated from the standard deviation from the mean over all accepted samples. In the case of the occupancy calculated from Σ_0 by FSR, the statistical error was calculated by error propagation from the standard deviation of Σ_0 , i.e.:

$$\delta n_d = |\delta n_d / \delta \Sigma_0|_{\Sigma_0} \delta \Sigma_0. \quad (117)$$

However, the statistical error is generally smaller for the ENS approach. Only for very strong asymmetry ($\epsilon_d = -3$) does the error of the FSR approach become slightly smaller than the one of the ENS approach, and also the mean values are closer to the NRG results for ENS than for FSR.

From Table. 1 we can see that the error in the occupancy $\langle n_d \rangle$ calculated via FSR as well as the error in Σ_0 decrease with increasing asymmetry. This can be understood by considering the acceptance ratio which becomes better the stronger the asymmetry (see Sec. 4.4) so that more samples are accepted (for a fixed total number of samples) contributing to the ensemble average for the self-energy, and thus improving the statistics. For small asymmetries the argument to \tan^{-1} in FSR (116) is close to zero ($\epsilon_d + \text{Re} \bar{\Sigma}(\epsilon_F) - \epsilon_F \approx 0$), and therefore \tan^{-1} has an approximately linear behavior so that $\delta n_d \approx \frac{2}{\pi} \delta \Sigma_0$, explaining the factor of roughly two between the error in $\langle n_d \rangle$ and the error in Σ_0 for small asymmetry since $2/\pi \Gamma \approx 2$ for $\Gamma = 0.3$. On the other hand, the error for $\langle n_d \rangle$ calculated via ENS *increases* slightly with increasing asymmetry despite more samples being accepted, since the occupancies of individual finite Anderson model samples fluctuate more strongly with increasing asymmetry.

4.3 Σ_0 determination

As explained in Sec. 3.3 the effective one-body potential Σ_0 entering the non-interacting Green's function (86) should be identified with the real part of the self-energy at the Fermi level, $\Sigma_0 \equiv \text{Re} \Sigma(\epsilon_F)$. However, with the exception of the ph-symmetric situation where $\text{Re} \Sigma(\epsilon_F) = U/2$, the self-energy at the Fermi level is unknown prior to calculation. Hence we propose to determine Σ_0 self-consistently, by starting with some initial guess, e.g. $\Sigma_0 \rightarrow U/2$. Using this initial guess the DED procedure yields $\text{Re} \bar{\Sigma}(\epsilon_F)$, generally different from Σ_0 , which is taken as the new guess, $\Sigma_0 \rightarrow \text{Re} \bar{\Sigma}(\epsilon_F)$. This procedure is repeated until self-consistency is reached, i.e. Σ_0 does not change anymore within a specified accuracy. We find that the self-consistency converges quite rapidly to an accuracy of under 1% within 3-4 cycles. In Fig. 13 we show the effect of the self-consistency for Σ_0 on the spectra close to the Fermi level. The agreement between NRG and DED using the converged value $\Sigma_0 = \text{Re} \bar{\Sigma}(\epsilon_F) \approx 2.65$ (red line) is quite

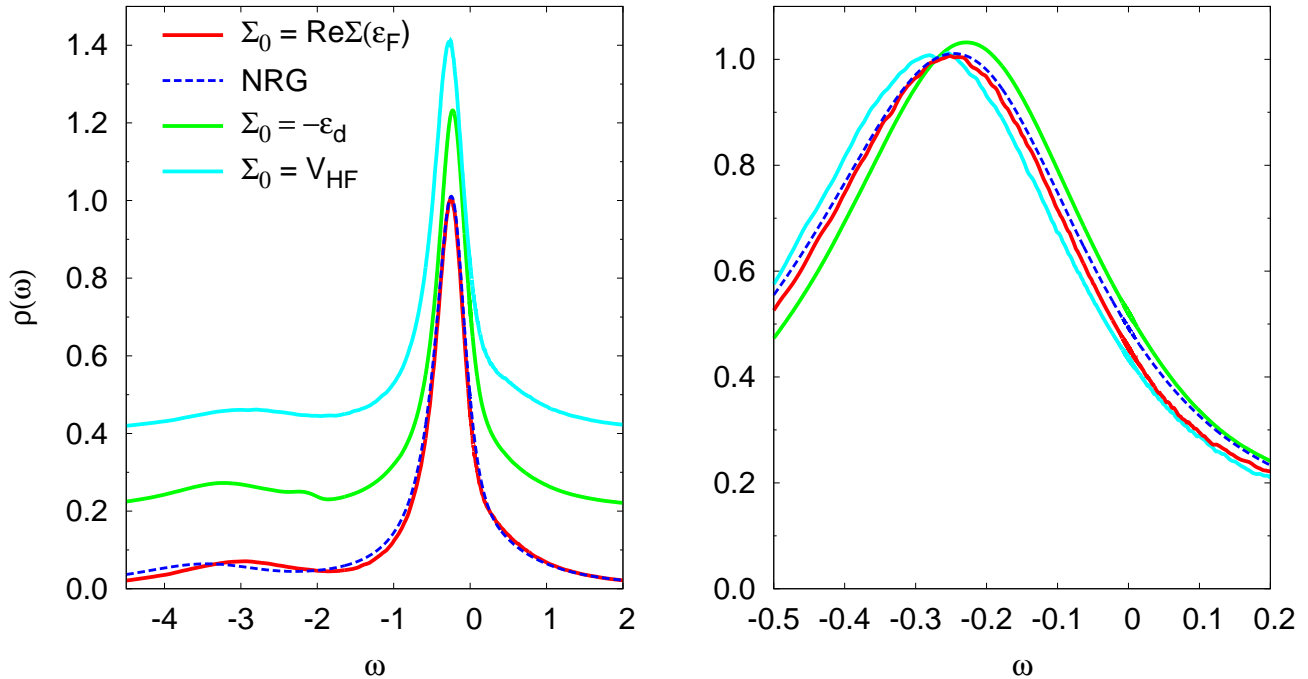


Figure 13: Spectral function close to the Fermi level for different values of Σ_0 calculated by DED ($n = 4$ sites) compared to NRG for $U = 3$, $\epsilon_d = -3$ and $\Gamma = 0.3$ on a large energy scale (left) and at low energies (right). Note that on the left panel the curves for $\Sigma_0 = -\epsilon_d$ (green) and for $\Sigma_0 = V_{\text{HF}}$ (cyan) have been offset by 0.2 and 0.4, respectively, in order to increase the visibility.

good. But the effect of self-consistency is actually relatively weak: DED with the initial guess $\Sigma_0 = -\epsilon_d$ or using the Hartree shift for Σ_0 yield spectra that are also quite close to the NRG spectrum, with the peak position just slightly shifted, even when using the Hartree-Fock potential $\Sigma_0 \equiv V_{\text{HF}} \approx 2.49$ (cyan line).

4.4 DED statistics

In Table 2 we summarize statistical information on the DED calculations reported in the text. One can see that the acceptance ratio r_{acc} increases with increasing Γ (i.e. decreasing correlation strength U/Γ), and increasing asymmetry. In both cases interaction effects become weaker, so that the non-interacting limit is approached, where the DED becomes exact already for the one-site model (the non-interacting DOS can be reproduced by simply sampling the non-interacting DOS $\rho_0(\omega)$ of course) where the constraint is always fulfilled.

ϵ_d	Γ	n	N_{tot}	N_{acc}	r_{acc}
-1.5	0.2	8	23875	7449	31%
-1.5	0.3	2	200000	57561	29%
-1.5	0.3	4	100000	35918	31%
-1.5	0.3	8	26000	11090	43%
-1.5	0.5	6	100000	55066	55%
-1.5	0.9	6	100000	70297	70%
-1.65	0.3	8	8500	3743	44%
-1.8	0.3	8	8495	3847	45%
-2.0	0.3	8	8495	4037	47%
-2.5	0.3	8	5093	3071	60%
-3.0	0.3	8	5100	4156	81%

Table 2: Summary of statistical information of the DED calculations reported in the text. Total number of samples N_{tot} , number of accepted samples N_{acc} , and the acceptance ratio r_{acc} for different values of ϵ_d , Γ and number of sites n . For all calculations $U = 3$ was used.

5 DED for finite temperatures

According to the results shown in the previous chapter the DED scheme with the particle constraint is well suited to describe the single impurity Anderson model at zero temperature. However, strongly correlated systems often show interesting behaviour at finite temperature, for example, high-temperature superconductivity, Coulomb blockade in quantum dots⁷⁰ and Mott metal-insulator transition.² Importantly the Kondo resonance is strongly temperature dependent. This has been shown experimentally^{19,71,72} as well as theoretically.^{73–75} On the other hand, thermodynamic properties are of particular interest for bulk systems, such as dilute concentrations of transition metal or rare-earth ions in nonmagnetic metals.^{8,76} Thermodynamic properties such as the specific heat and susceptibility as a function of temperature provide important information of the system, e.g. whether the system behaves as a Fermi liquid or not.^{76,77} Hence, in order to be able to describe the exciting physics occurring at finite temperatures by means of DED, the next step is to generalize the approach to finite temperatures.

5.1 Straightforward generalization to finite temperatures

To calculate the impurity spectral density at finite temperatures, the DED procedure is implemented as in the zero temperature case, except that now all the excitations contribute to the spectra (not only excitations from the ground state). We know that at zero temperature only states up to the Fermi level are occupied, but when temperature increases also states above the Fermi level can be occupied and states below the Fermi level vacated. In order to include the effect of all excited states as well, in the interacting finite Anderson model ν , the general form of the Lehmann representation is used,

$$G_{\sigma}^{\nu}(\omega) = \frac{1}{Z^{\nu}} \sum_{nm} \frac{\langle n^{\nu} | d_{\sigma} | m^{\nu} \rangle \langle m^{\nu} | d_{\sigma}^{\dagger} | n^{\nu} \rangle}{\omega^{+} + E_n^{\nu} - E_m^{\nu}} \left(e^{-\beta E_n^{\nu}} + e^{-\beta E_m^{\nu}} \right) \quad (118)$$

where n^{ν} and m^{ν} run over all eigenstates, including those with occupancies different from the ground state, and E_n^{ν} and E_m^{ν} are the corresponding eigenenergies for each sample ν . Following the DED procedure the corresponding self-energy $\Sigma^{\nu}(\omega, T)$ for each finite Anderson model ν , is calculated via eq. (98). Finally, the self-energy of the original infinite Anderson model is approximated by the ensemble average,

$$\bar{\Sigma}_{\sigma}(\omega, T) = \frac{1}{N} \sum_{\nu=1}^N \Sigma_{\sigma}^{\nu}(\omega, T), \quad (119)$$

which leads to the corresponding interacting Green's function,

$$G_{\sigma}(\omega, T) = \frac{1}{\omega^{+} - \epsilon_d - \bar{\Sigma}_{\sigma}(\omega, T) - \Delta(\omega)}. \quad (120)$$

Performing the DED scheme as explained above results in the impurity spectral densities $\rho(\omega, T) = -1/\pi \text{Im} G_{\sigma}(\omega, T)$ at different temperatures according to Fig. 14a. In this figure we present the corresponding results of the single impurity Anderson model at particle-hole symmetry, $U = -\epsilon_d$ for $U = 3$ and $\Gamma = 0.3$ with $n = 4$. In addition, $\Gamma_K = 0.042$ is determined from the corresponding zero temperature $T = 0$ spectrum ($n = 4$), by measuring the half width at the half maximum of the Kondo peak. It should be mentioned that the half width of the Kondo peak at $T = 0$ for the $n = 4$ model, is overestimated by a factor of 2 in comparison with that of the NRG (see Fig. 8). So, we expect to

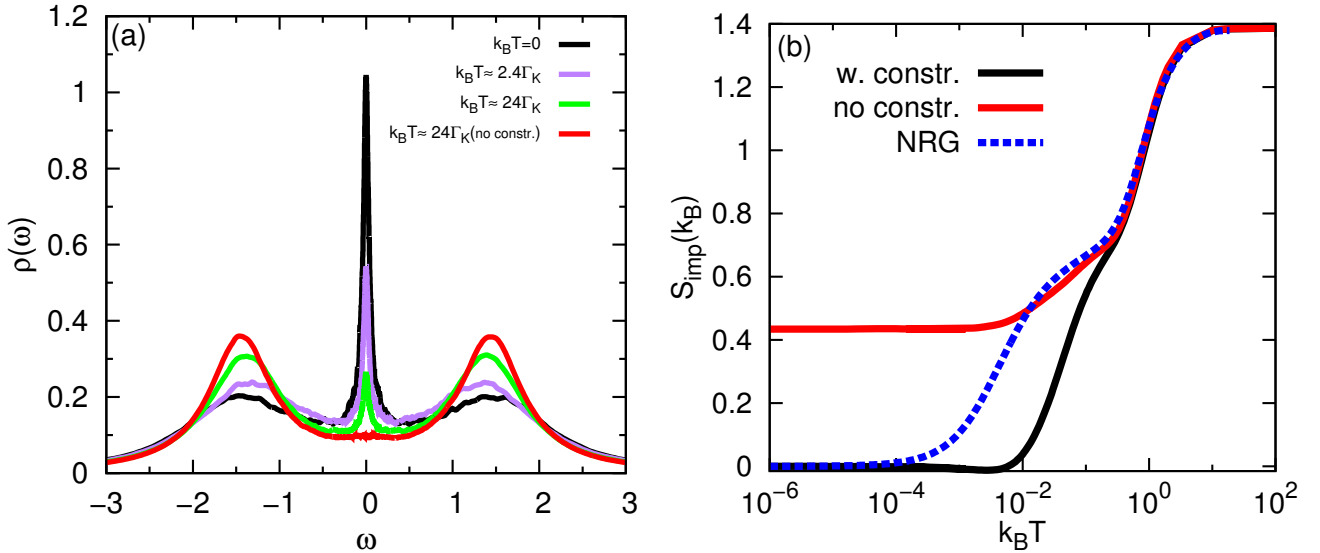


Figure 14: Effect of temperature for the symmetric Anderson model for $U = 3$, $\epsilon_d = -1.5$ and $\Gamma = 0.3$: (a) DED spectral densities for different temperatures with $n = 4$. $\Gamma_K = 0.042$ is the half-width (at half maximum) of the Kondo peak at $T = 0$ for $n = 4$. For very high temperature ($k_B T \approx 24\Gamma_K$) the DED spectrum when no constraint is imposed is also shown. (b) Comparing the impurity entropy calculated by DED with (black line) and without (red line) imposing the particle number constraint for $n = 6$ sites and NRG.

see the temperature evolution of the Kondo peak to be determined by the Kondo temperature for the $n = 4$ model.

The expected behaviour of the single-particle spectral densities with respect to temperature for the Anderson model is as follows: At low temperatures $T \ll T_K$, where the Anderson model is in the Kondo regime, the spectrum is characterized by three resonances: A narrow Kondo resonance at the Fermi level of width approximately T_K , and two (atomic like) Hubbard resonances at ϵ_d and $\epsilon_d + U$ energies (see Sec. 2.1), which carry most of the spectral weight. On increasing the temperature, the Kondo resonance reduces in height and eventually vanishes at $T \gg T_K$, while the two Hubbard resonances acquire more weight with increasing temperature. Thus, at high temperatures $T \gg T_K$, the spectral density is well described by the two Hubbard side peaks. Fig. 14a shows that the expected evolution of the spectral density is partially captured, i.e. the height of the Kondo peak somehow decreases and the weight of the side peaks increases. But even substantially above the Kondo temperature $k_B T \approx 24\Gamma_K$, where the Kondo peak should have vanished completely,⁷⁴ in the DED spectrum (green line) the Kondo peak has not entirely disappeared yet. On the other hand, following the red line, it immediately can be realized that DED, when no constraint is applied (i.e. all configurations equally contribute to the sampled average self-energy), is able to produce the qualitatively correct result for high temperatures. This indicates that the DED scheme without the constraint seems to be suited for describing the high temperature physics e.g. the Coulomb blockade regime or the Mott insulating phase of the Hubbard model.⁵⁵

This failure of DED to describe the transition from the low temperature to the high temperature regime is also present in the thermodynamic properties as we will see. In the next step, we study the

impurity contribution to the entropy as a central quantity of the thermodynamic properties for the symmetric Anderson model. Assuming a grand canonical ensemble, the grand potential is:

$$\Omega = -k_B T \ln Z(T) \quad (121)$$

where $Z(T) = \sum_n e^{-\beta(E_n - \mu N_n)}$ is the partition function. Note that without loss of generality the chemical potential can be set to zero, $\mu = 0$. The impurity contribution to the entropy, $S_{\text{imp}}(T)$ can be calculated from the total entropy $S(T)$, when the bath contribution to the entropy $S_{\text{bath}}(T)$, is subtracted,⁷⁶ i.e.

$$S_{\text{imp}}(T) = S(T) - S_{\text{bath}}(T). \quad (122)$$

We approximate the impurity entropy as a function of temperature within DED, from the ensemble average, similar to the self-energy (see Sec. 3.2). The impurity entropy for each sample ν can be obtained from eq. (122), namely,

$$S_{\text{imp}}^\nu = S^\nu(T) - S_{\text{bath}}^\nu(T). \quad (123)$$

$S^\nu(T)$ is the total entropy of the finite size AIM where the corresponding Hamiltonian is given by eq. (160) and $S_{\text{bath}}^\nu(T)$ is the contribution of the conduction electron bath to the entropy where the Hamiltonian of conduction electrons H_{bath} , is simply given by,

$$H_{\text{bath}}^\nu = \sum_{\sigma, k=1}^{n-1} \epsilon_k^\nu c_{k\sigma}^\dagger c_{k\sigma}. \quad (124)$$

From the eigenenergies of the Hamiltonian H^ν , the grand canonical partition function,

$$Z^\nu(T) = \text{Tr} e^{-\beta H^\nu} = \sum_n e^{-\beta E_n^\nu} \quad (125)$$

and the corresponding thermodynamic potential,

$$\Omega^\nu(T) = -k_B T \ln Z^\nu(T) \quad (126)$$

can be constructed. Thus the total entropy of the finite AIM can be calculated by,

$$S^\nu(T) = -\frac{\partial \Omega^\nu}{\partial T} = k_B \ln Z^\nu(T) + \frac{\langle H^\nu \rangle}{T} \quad (127)$$

where the corresponding total energy is obtained as follows:

$$\langle H^\nu \rangle = \frac{1}{Z^\nu} \sum_n E_n^\nu e^{-\beta E_n^\nu}. \quad (128)$$

The entropy contribution of the isolated conduction electron bath (i.e. not connected to the impurity) is,

$$S_{\text{bath}}^\nu(T) = -\frac{\partial \Omega_{\text{bath}}^\nu}{\partial T} = k_B \ln Z_{\text{bath}}^\nu(T) + \frac{\langle H_{\text{bath}}^\nu \rangle}{T}. \quad (129)$$

Since the bath is a non-interacting system, the corresponding partition function is given by

$$Z_{\text{bath}}^\nu = \sum_\sigma \prod_k (1 + e^{\beta \epsilon_k^\nu}) \quad (130)$$

where the ϵ_k^ν 's are the energies of the bath levels of each sample. Finally, the corresponding energy for the isolated conduction electron bath is obtained via

$$\langle H_{\text{bath}}^\nu \rangle = \sum_{\sigma} \int d\omega \rho_0^\nu(\omega) f(\omega) \omega = \sum_{\sigma} \sum_k \epsilon_k^\nu f(\epsilon_k^\nu) = \sum_{\sigma} \sum_k \frac{\epsilon_k^\nu}{e^{\beta \epsilon_k^\nu} + 1}, \quad (131)$$

where the non-interacting density of states is given by $\rho_0^\nu(\omega) = \sum_k \delta(\omega - \epsilon_k^\nu)$ and $f(\omega)$ is the Fermi function. Applying the DED ensemble average as described by eq. (119) for the self-energy to the impurity entropy yields

$$\bar{S}_{\text{imp}}(T) = \frac{1}{N} \sum_{\nu} S_{\text{imp}}^\nu(T). \quad (132)$$

In Fig. 14b we show the impurity entropy as a function of temperature for the symmetric Anderson model ($U = 3$, $\epsilon_d = -1.5$) and $\Gamma = 0.3$, calculated from eq. (132) for $n = 6$ (black curve), in comparison with the numerical renormalization group (NRG) flow (blue curve). Again we take the NRG results as a benchmark which have been shown to be in perfect agreement with exact Bethe-Ansatz calculations.⁷⁶

The impurity entropy behaviour in the Anderson model is characterized by three different regions: In the high temperature limit the entropy is given by $S_{\text{imp}} = \ln 4$, since the 4 impurity states (empty, singly occupied with either spin, or doubly occupied state) are effectively degenerate at high temperature. In the low temperature limit, on the left side of the plot, the entropy value goes to zero, $S_{\text{imp}} = 0$, expressing that the spin of the impurity forms a total spin singlet state. Between the two mentioned regions, Fig. 14b (blue and black curve) shows how the impurity entropy is quenched from its high to its low values as temperature is reduced. The quenching process basically occurs in two stages: Starting from the high temperatures limit and decreasing temperature the first quenching stage happens. At this stage, since the singly occupied states of either spins are lower in energy, the size of the effective impurity Hilbert space reduces from 4 to 2 which corresponds to the formation of free local moments. As in this local moment regime only the spin degree of freedom remains, there are only two accessible states for the impurity, corresponding to the entropy as $S_{\text{imp}} = \ln 2$. On further decreasing the temperature, the second quenching stage takes place. Now the system reaches the crossover between the local moment regime and the Kondo regime at the Kondo temperature T_K . Finally, below the Kondo temperature the Kondo singlet forms, leading to the complete screening of the impurity spin by conduction electrons, so that $S_{\text{imp}} = 0$.

The impurity entropy as calculated by DED when the particle constraint is imposed (black curve), captures the overall expected behaviour, given by NRG, as can be seen in Fig. 14b. At low temperatures as well as at high temperatures, we see good agreement with NRG, whereas in the crossover regime, the DED result is considerably off from the NRG's. This large deviation from NRG corresponds to the persistence of the Kondo peak in the spectra at finite temperatures. More importantly, the temperature evolution is not consistent with the Kondo temperature estimated from the half width of the Kondo peak at $T = 0$. More precisely, in the crossover region between the local moment regime and the Kondo regime, where the system reaches the Kondo temperature a large difference (of about 2 orders of magnitude) between the DED and the NRG impurity entropy is seen. However, referring to Fig. 10 the half width of the Kondo peak at $T = 0$ for the $n = 6$ model is only slightly overestimated (factor of 1.4) in comparison to that of NRG. Note that the Kondo temperature is proportional to the half width of the Kondo peak,⁷⁸ i.e:

$$T_K = \Gamma_K/3.7 \quad (133)$$

where Γ_K is the half width of the Kondo peak at half maximum at $T = 0$. On the other hand, considering the DED impurity entropy when no constraint is applied (red curve), shows almost perfect agreement with NRG at high temperatures. However, as expected (see Fig. 6) in the low temperature region no correspondence between NRG and DED without the particle constraint, which yields a finite entropy, is achieved.

Comparing the impurity entropy calculated by DED as a function of temperature with the NRG one further shows that imposing the particle constraint is essential to describe the low temperature region. As we argued in detail in Sec. 3.3, the particle constraint enforces a spin singlet state to govern the Fermi liquid behaviour. Apparently, imposing the particle constraint when the temperature is raised leads to the persistence of Fermi liquid behaviour and the Kondo singlet state at finite temperatures, as can be seen from the temperature evolution of the spectra (Fig.14a) and the entropy (Fig. 14b). Another very interesting aspect, which can be seen in Fig. 14b, is that in the intermediate temperature regime, where we see the persistence of the Kondo peak, the correct impurity entropy behaviour (given by NRG), seems to be an interpolation between imposing no constraint (red curve) and imposing the particle constraint (black curve). Therefore, in order to capture the temperature evolution of the spectra and entropy with DED, it seems to be necessary to relax the particle constraint in some way at finite temperature. In this way the full particle constraint would impose Fermi liquid behaviour at low temperatures, while at high temperatures the complete lifting of the constraint would describe non-Fermi liquid behaviour.

5.2 Relaxation of the constraint

In the previous section, we elaborated that the particle constraint in the DED formalism, needs to be relaxed in some way in order to make the method capable of describing the correct behaviour at finite temperatures. From another point of view, generally at zero temperature the state of system can be described as a pure singlet state, which in terms of the density matrix can be written as:

$$\hat{\rho} = |0\rangle\langle 0|, \quad (134)$$

where $|0\rangle$ is the ground state, with

$$S^2|0\rangle = 0. \quad (135)$$

The interaction between the Kondo cloud and the rest of the system is basically very weak. Hence, in the DED scheme the idea is to describe the Kondo correlation cloud by means of an impurity level plus a finite number of bath sites, as the Kondo cloud interacts very weakly with the rest of the system, according to the Fermi liquid picture.⁶⁶ In DED the system of one impurity and a few number of bath sites may arrange various configurations where the energy levels and the hopping between levels differs from one to the other. It is important to emphasize that the mixture of those configurations (samples) satisfies eq. (135) only if each configuration (sample) itself satisfies eq. (135), since the expectation value of the spin angular momentum is always positive, i.e. $S^2|s, m_s\rangle = \hbar^2 s(s+1)|s, m_s\rangle$. This is another way of interpreting the particle constraint role which guarantees the singlet ground state for each sample (see Sec. 3.3). Thus in DED the state of the system in the Kondo regime at

zero temperature is described as a mixture of singlets, namely,

$$\hat{\rho}_{\text{DED}} \equiv \text{Tr}_{\text{res}} [|0\rangle\langle 0|] \approx \frac{1}{N} \sum_{\nu}^N |0^{\nu}\rangle\langle 0^{\nu}| \quad (136)$$

where “res” stands for the rest of the system which is assumed to interact only weakly with the Kondo spin singlet state in the DED formalism. When temperature is raising, the phase coherence is lost, meaning that the system cannot be described as a pure singlet state anymore but rather as a mixed state i.e.:

$$\hat{\rho} = \sum_n e^{-\beta E_n} |n\rangle\langle n|. \quad (137)$$

Hence in analogy to the exact system also in the DED formalism we should produce a mixed state. Apparently, in DED at finite temperatures it is not enough to only consider the excited states of the samples with singlet ground state (see Sec. 5.1). Therefore, we assume a mixture of singlet and non-singlet configurations:

$$\hat{\rho}_{\text{DED}} \equiv \text{Tr}_{\text{Bath}} \left[\sum_n e^{-\beta E_n} |n\rangle\langle n| \right] \approx \sum_{\nu} q_{\nu}(T) \sum_{n^{\nu}} |n^{\nu}\rangle\langle n^{\nu}| e^{-\beta E_n^{\nu}} \quad (138)$$

Including the non-singlet configurations should happen smoothly in order to gradually balance the Kondo singlet state with respect to temperature increment. Therefore, we include the non-singlet configurations with some temperature dependent weight $q_{\nu}(T)$, to calculate the ensemble average quantities, e.g. self-energy:

$$\bar{\Sigma}(\omega, T) = \frac{1}{Q(T)} \sum_{\nu} q_{\nu}(T) \Sigma^{\nu}(\omega, T) \quad (139)$$

and the impurity entropy:

$$\bar{S}_{\text{imp}}(T) = \frac{1}{Q(T)} \sum_{\nu} q_{\nu}(T) S_{\text{imp}}^{\nu}(T), \quad (140)$$

with $Q(T) = \sum_{\nu} q_{\nu}(T)$. In addition, this weight q_{ν} , (yet to be determined), should satisfy two extreme conditions: At low temperatures $T \ll T_K$, it should recover the particle constraint and at high temperatures $T \gg T_K$, it should include all the configurations, thereby effectively lifting the effect of the constraint.

The entire system of N finite size Anderson models can be considered as an ensemble of N systems which may be labelled as $\nu = 1, 2, \dots, N$. Since the various possible states (with a given energy value) are equally likely to occur, the relevant probability is given by P_{ν} , which should obey:

$$\sum_{\nu} P_{\nu} = 1 \quad (141)$$

The probability P_{ν} at a certain temperature is related to the weight factor q_{ν} as,

$$P_{\nu}(T) = \frac{q_{\nu}(T)}{Q(T)} \quad (142)$$

The averaged energy of the ensemble $\delta\bar{E}$ is given by,

$$\sum_{\nu} P_{\nu} \delta E_{\nu} = \delta\bar{E} \quad (143)$$

where δE_ν ($\nu = 0, 1, 2, \dots, N$) denote some energy scale of the systems, which has to be determined. The original aim of relaxing the particle constraint was about finding some energy scale to weaken the effect of the Kondo singlet state at finite temperatures. In addition we keep in mind that in the zero temperature limit the weight factor q_ν should recover the particle constraint. Therefore we conjecture that an energy scale which is associated with the energy required for breaking the Kondo singlet state should be assumed, e.g.:

$$\delta E_\nu = E_\nu(N'_0) - E_\nu(N^\nu). \quad (144)$$

N^ν (N'_0) denotes the ground state particle number of the interacting (non-interacting) systems corresponding to H^ν and H'_0 , respectively. $E_\nu(N^\nu)$ and $E_\nu(N'_0)$ denote the minimum eigenenergy of the corresponding N^ν and N'_0 subspaces.

All possible states of the ensemble, compatible with the conditions (141) and (143) are equally likely to occur. Then, the aim is to determine the distribution set which while satisfying the conditions (141) and (143) also maximizes the ensemble entropy,

$$S = - \sum_\nu P_\nu \ln P_\nu. \quad (145)$$

The desired $\{P_\nu\}$ set is determined by the method of Lagrange multipliers, by which the condition determining this set becomes

$$- \sum_\nu P_\nu \ln P_\nu - \alpha \left(\sum_\nu P_\nu - 1 \right) - \beta \left(\sum_\nu P_\nu \delta E_\nu - \delta \bar{E} \right) = 0. \quad (146)$$

To maximize the entropy, its variation δS with respect to $\{P_\nu\}$ should vanish, i.e.:

$$\frac{\delta S}{\delta P_\nu} = -\ln P_\nu - 1 - \alpha - \beta \delta E_\nu = 0 \quad (147)$$

which yields,

$$P_\nu = e^{-1-\alpha} e^{-\beta \delta E_\nu} \quad (148)$$

As $\sum_\nu P_\nu = 1$ should hold,

$$\sum_\nu P_\nu = e^{-1-\alpha} \sum_\nu e^{-\beta \delta E_\nu} = 1 \quad (149)$$

then,

$$e^{-1-\alpha} = 1 / \sum_\nu e^{-\beta \delta E_\nu} \equiv Q^{-1} \quad (150)$$

Hence, the weight of each Anderson model in the ensemble at finite temperature is obtained by,

$$q_\nu = e^{-\beta \delta E_\nu} \quad (151)$$

and

$$P_\nu = Q^{-1} q_\nu \quad (152)$$

In the zero temperature limit ($\beta \rightarrow \infty$) this Boltzmann factor reduces to the expression of eq. (99):

$$\lim_{\beta \rightarrow \infty} \exp(-\beta (E_\nu(N^\nu) - E_\nu(N'_0))) = \begin{cases} 1 & \text{for } N^\nu = N'_0 \\ 0 & \text{for } N^\nu \neq N'_0 \end{cases} \quad (153)$$

Conversely, at high temperatures ($\beta \rightarrow 0$) the constraint is effectively lifted as $\exp(-\beta (E_\nu(N^\nu) - E_\nu(N'_0))) \rightarrow 1$. Thus the generalized DED scheme relaxes the constraint for increasing temperatures thereby allowing to balance the Kondo singlet state.

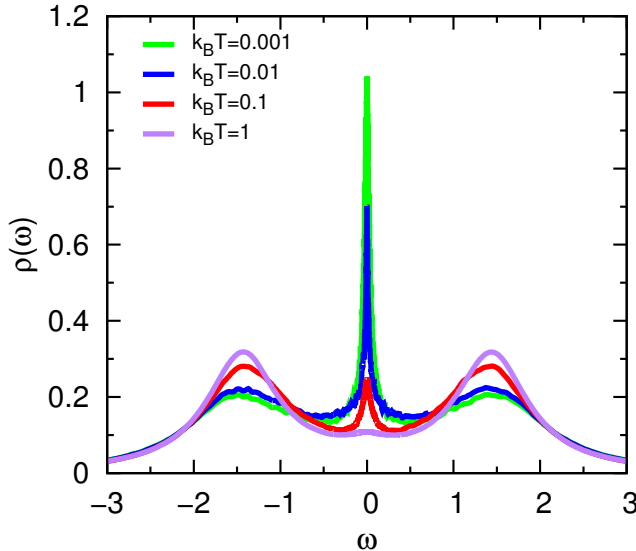


Figure 15: DED spectral densities with $n = 4$ for $U = 3, \epsilon_d = -1.5, \Gamma = 0.3$ at different temperatures when the particle constraint is relaxed.

5.3 Finite temperature results

Now, within the generalized DED, as explained in the previous section, we compute the impurity spectral densities at different temperatures as well as the impurity contribution to the entropy as a function of temperature for the symmetric single AIM ($\epsilon_d = -U/2$ and $\langle n \rangle = 1$). Fig. 15 shows the spectral densities $\rho(\omega) = -\frac{1}{\pi} \text{Im} G(\omega)$ for $U = 3$ and $\Gamma = 0.3$ at different temperatures calculated by DED with $n = 4$. As we are in the Kondo regime the spectral density of the Anderson model is characterized by three peaks, two Hubbard side peaks and a sharp Kondo peak. On increasing the temperature, the Kondo resonance decreases rapidly in height and eventually disappears completely for $T \gg T_K$ while the side peaks gain more weight as temperature is raised. As can be seen the expected behaviour is captured correctly by DED when the particle constraint is relaxed. In contrast to the DED calculations with no relaxation (Fig. 14a) where the Kondo peak does not disappear even at very high temperatures, one can see here that relaxing the constraint leads to the complete vanishing of the Kondo peak at high temperatures (purple curve).

Now to study how the quality of DED spectra change at different temperature regimes, we compare the DED results with the corresponding NRG ones at a wide temperature range, from far below to far above the Kondo temperature T_K . In Fig. 16 we present the spectral densities $\rho(\omega) = -\frac{1}{\pi} \text{Im} G(\omega)$ calculated by DED with $n = 4$ in comparison with NRG for the same set of parameters as before at different temperatures. In addition to observe the effect of the relaxation, at each temperature value we also report the corresponding DED spectrum without relaxing the particle constraint. It can be seen clearly that the height of the Kondo peak is captured quite well when we relax the constraint, while before relaxing the constraint the height of the Kondo is substantially overestimated. The only exception is the panel *a* where we are very low in temperature and the effect of the relaxation is not yet visible.

If we calculate the Kondo temperature T_K from eq. (133) while taking Γ_K as the half width of the Kondo peak in the NRG spectrum, the corresponding value becomes $T_K = 0.006$. So, below the

Kondo temperature Fig. 16a the quantitative agreement between NRG and DED is almost perfect. It should be kept in mind that the DED results presented here are only for three bath sites ($n = 4$). Near the Kondo temperature Fig. 16b, the DED and NRG spectrum are still in quite good agreement. However, at higher temperatures (Fig. 16c), the DED spectrum deviates from the NRG spectrum: the DED side peaks are somewhat higher while the Kondo peak is narrower, although the height of the Kondo peak is correctly captured by DED. The deviation of the DED spectrum from the NRG one becomes more considerable at very high temperatures, to the extent that the Kondo peak in DED requires a higher temperature to disappear in comparison with NRG (Fig. 16d). In Fig. 16d we show the DED (green line) and NRG (blue line) spectrum at $k_B T = 0.3$. As can be seen in contrast to NRG, in the DED result the Kondo peak has not disappeared. To wash out the Kondo peak in the DED calculations higher temperatures are required. This can be observed in the purple spectrum in Fig. 15 which shows the DED spectrum at $k_B T = 1$. This behaviour can be understood by comparing the half width of the Kondo peak at $T = 0$ in the DED spectrum with ($n = 4$) and that of NRG (see Fig. 10). Since the Kondo peak is wider in the DED ($n = 4$) spectrum, the Kondo temperature for the $n = 4$ model is higher, so that higher temperatures are required to wash out the Kondo peak.

Next we investigate the quality of the DED impurity entropy in different regimes where the correlation strength i.e. U/Γ is changed. The corresponding DED results for $U = 3$ compared to the NRG results are shown in Fig. 17. In order to better resolve the impurity entropy behaviour, temperatures are plotted on a logarithmic scale. Overall, the qualitative behaviour of the impurity entropy is captured by DED when the particle constraint is relaxed, as can be seen. Following Fig. 16a-d, one can see that the quantitative agreement between DED and NRG improves when the correlation strength is reduced. In the regime of stronger correlation strength ($\Gamma = 0.2$) where the number of bath sites necessary to correctly describe the system becomes too big to be feasible at the current level of DED, the DED curve is quite off from the NRG one (Fig. 16a). In Fig. 16b we show the DED results for $\Gamma = 0.3$ with $n = 2, 4, 8$ compared to NRG with the same set of parameters as before. Here we are in the Kondo regime but the correlation strength is not as strong as in the previous case (Fig. 16a). Nevertheless, the DED impurity entropy even for $n = 8$ is not in very good agreement with that of NRG, even though the $T = 0$ DED spectrum showed almost perfect agreement with NRG (see Fig.8 in Sec.4.1). Following the DED results for different n once more we see that the DED results improve by enlarging the finite Anderson models. By further decreasing the correlation strength DED yields closer results to NRG. In Fig. 16c where $\Gamma = 0.5$ we expect to obtain perfect agreement with NRG already for $n = 6$, since the effect of correlations are not so strong and we saw perfect correspondence of DED with NRG in the spectra at $T = 0$ (see Fig.9b). As it is not yet achieved we also bring in the DED calculations for $n = 8$. Including more bath sites results in moving the DED curve towards the NRG curve but even for ($n = 8$) DED is not completely on top of NRG. Finally in Fig. 16d we achieve excellent agreement with NRG where the Anderson model is not in the Kondo regime anymore: the shoulder corresponding to the local moment regime is non existence, basically the Hilbert space of the impurity electron is effectively reduced from 4 to 1 in one step by decreasing the temperature.

5.4 Discussion

Following the impurity entropy behaviour it can be understood that by relaxing the constraint as discussed, the thermodynamic properties, specifically the impurity contribution to the entropy is not described as well as the spectral density evolution with temperature increment. The impurity entropy behaviour is not completely consistent with the spectral density behaviour. More precisely, the Kondo temperature is only slightly overestimated by DED ($n = 8$), according to the width of the Kondo peak at $T = 0$, while in Fig. 16b a larger difference between the DED ($n = 8$) and NRG in the crossover between the Kondo regime and the local moment regime is visible. In addition the high temperature impurity entropy is precisely captured with and without imposing the particle constraint (see Fig.14b) which is not the case in the spectral density. Enforcing the particle constraint leads to the persistence of the Kondo peak in the spectral density even when temperature is strongly increased (see Fig. 14a). This inconsistency in the entropy and the spectral density behaviour leads us to believe that perhaps the impurity entropy should be calculated differently. Here we propose another approach which may help to improve the current thermodynamic results. Apparently, the DED approach is constructed to capture the correct behaviour of the self-energy and the spectral density. Therefore a possibly more plausible way is to calculate the impurity entropy or any thermodynamic quantity via the sample averaged self-energy. To this end, for instance the free energy can be written as a functional of the self-energy⁷⁹ as:

$$F [\bar{\Sigma}] = -2 \sum_{i\omega} \ln (G_0^{-1}(i\omega) - \bar{\Sigma}(i\omega)), \quad (154)$$

where $i\omega$ are Matsubara frequencies. From the free energy the impurity entropy can be obtained as the temperature derivative,

$$S = -\frac{\delta F}{\delta T}. \quad (155)$$

In general, thermodynamic quantities are very sensitive to the high-frequency behaviour of the Green's function and the self-energy on the Matsubara axis which causes problems for making cutoffs.⁸⁰ However this problem can in principle be controlled by the approach suggested by Deisz *et al.*⁸⁰

Another important issue that should be discussed here is the lack of quantitative agreement between the DED and NRG spectra at high temperatures. Remembering that at low temperatures $T \ll T_K$, the standard interpretation is that a spin- $\frac{1}{2}$ impurity is screened by a surrounding Kondo cloud of spatial extent ξ_k . A.K. Mitchell *et al.* argued that the behaviour of ξ_k at high temperatures is described as $\xi_k(T) \propto \frac{\xi_k(0)}{1-b(T/T_K)}$, where b is a first order function.⁸¹ Due to electron correlations the Kondo cloud evaporates on increasing temperature⁸¹ which possibly explains that in the DED calculations one needs to include more number of bath sites, in order to produce a perfect description of the system at high temperatures.

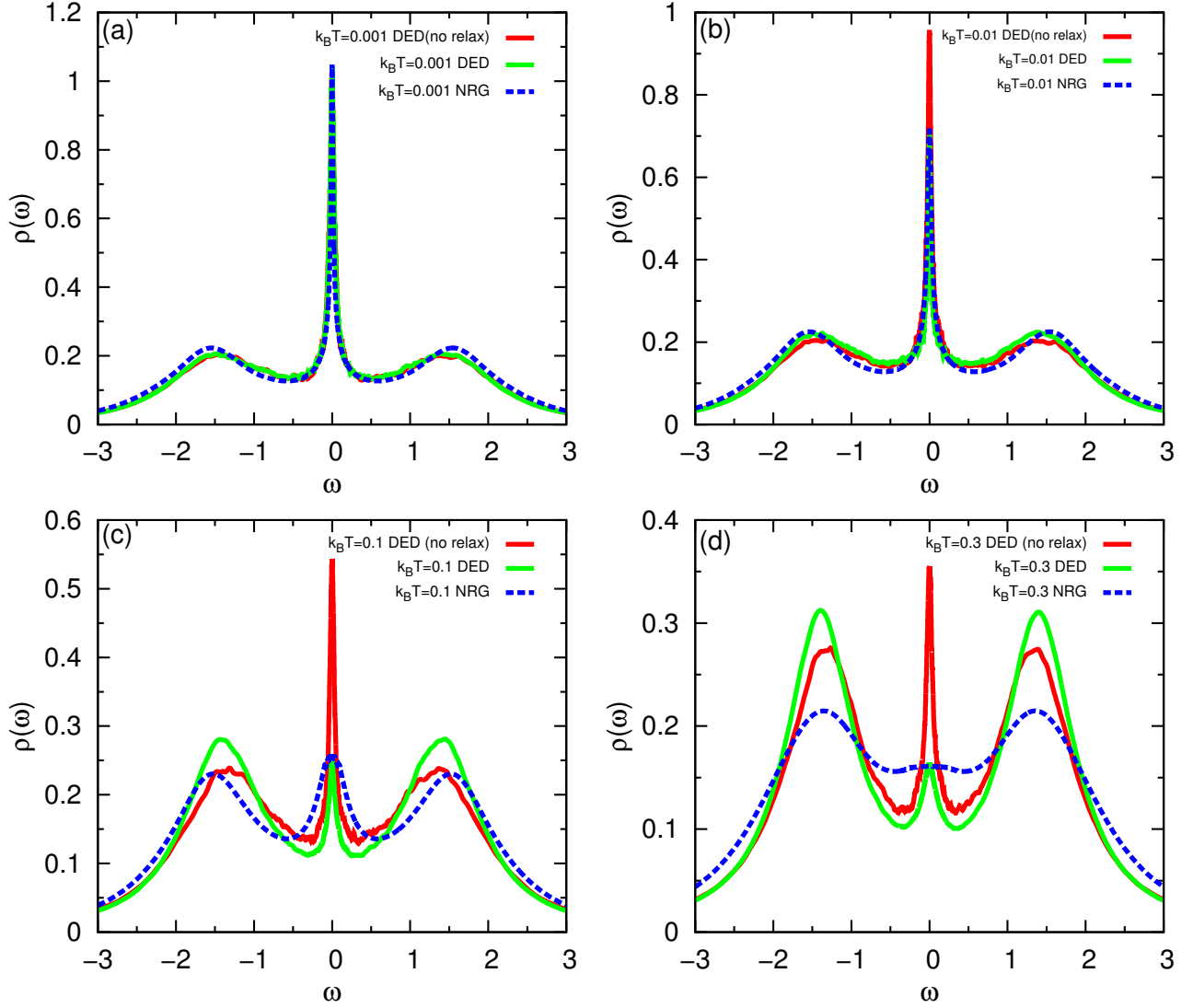


Figure 16: Comparison between DED ($n = 4$) before and after relaxing the constraint and NRG spectra for the symmetric Anderson model at finite temperatures ($U = 3$, $\epsilon_d = -1.5$, $\Gamma = 0.3$). (a) Comparison between DED and NRG spectra at $k_B T = 0.001$. (b) Comparison between DED and NRG spectra at $k_B T = 0.01$. (c) Comparison between DED and NRG spectra at $k_B T = 0.1$. (d) Comparison between DED at $k_B T = 0.3$, $k_B T = 1$ and NRG spectra at $k_B T = 0.3$.

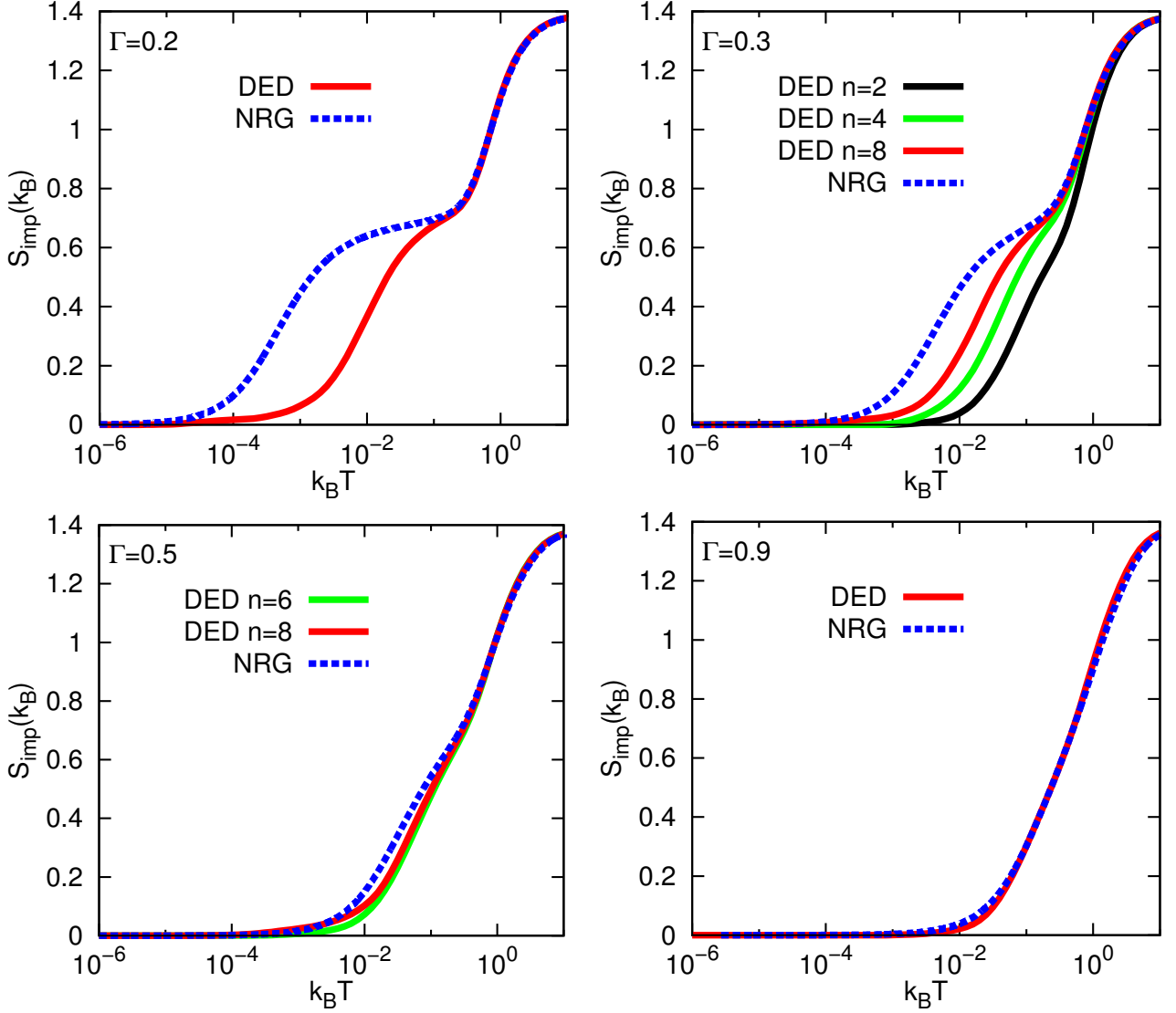


Figure 17: Comparison between the DED and NRG impurity entropy for the symmetric Anderson model ($U = 3$, $\epsilon_d = -1.5$), with different Γ values. Comparison between DED and NRG for $\Gamma = 0.2$ (the upper left panel). Comparison between DED ($n = 8$) and NRG for $\Gamma = 0.3$ with different number of sites n (the upper right panel). Comparison between DED ($n = 8$, $n = 6$) and NRG for $\Gamma = 0.5$ (the bottom left panel). Comparison between DED ($n = 6$) and NRG for $\Gamma = 0.9$ (the bottom right panel).

6 Towards multi-orbital Kondo physics in real systems

The case of a single correlated impurity orbital in a metal host has been hitherto thoroughly investigated. However, describing strongly correlated materials in realistic situations, requires that all the (highly correlated) d or f electrons in different orbitals be considered. This is naturally accompanied by more complexity, due to more than one orbital being involved: besides the interactions within orbitals (intra-orbital Coulomb repulsion), also interactions between orbitals, (inter-orbital Coulomb repulsion) as well as Hund's rule coupling, should be taken into account. The interplay of these highly correlated electrons in different orbitals may result in a variety of interesting and exotic phenomena, such as non-Fermi liquid behaviour⁸² or the orbital selective Mott transition.⁸³

In the following, in order to generalize the DED method to multi-orbital situations, we focus on the two-orbital Anderson model and initially on situations governed by Fermi liquid behaviour. At the end of this chapter the underscreened Kondo effect is studied as an example of non Fermi liquid behaviour.

6.1 The two-orbital Anderson model

Generally, the multi-orbital Anderson impurity model, describes a local impurity with both orbital and spin degrees of freedom coupled to a bath of non-interacting conduction electrons. It is not only the paradigmatic model for the description of magnetic impurities such as Fe or Mn in non-magnetic metal hosts such as Au, but has also successfully been applied to the description of magnetic adatoms and molecules on metallic substrates,⁸⁴⁻⁹⁶ quantum dots coupled to conducting wires⁹⁷ and single molecules coupled to metal leads^{98,99}

The two-orbital Anderson model as a first step towards multi-orbital model for the entire d - or f -shell, already captures the additional complexity that leads to exotic phenomena (e.g. non Fermi liquid behaviour and the orbital selective Mott transition). Additionally, it can still be treated by Numerical renormalization group (NRG) so that we can benchmark the DED results with NRG calculations. The two-orbital Anderson model is defined by the following Hamiltonian:

$$\begin{aligned}
\hat{H}_{\text{AIM}} &= H_{\text{bath}} + H_{\text{impurity}} + H_{\text{coupling}} \\
H_{\text{bath}} &= \sum_{km\sigma} \epsilon_{km} c_{km\sigma}^\dagger c_{km\sigma} \\
H_{\text{coupling}} &= \sum_{m\sigma} V_{km} (c_{km\sigma}^\dagger d_{m\sigma} + d_{m\sigma}^\dagger c_{km\sigma}) \\
H_{\text{impurity}} &= \sum_{m\sigma} \epsilon_{dm} d_{m\sigma}^\dagger d_{m\sigma} + \frac{U}{2} \sum_{m\sigma\sigma'} n_{m\sigma'} n_{m\sigma} \\
&\quad + \frac{U'}{2} \sum_{m \neq m' \sigma \sigma'} n_{m\sigma} n_{m'\sigma'} + \frac{J_H}{2} \sum_{m \neq m' \sigma \sigma'} d_{m\sigma}^\dagger d_{m'\sigma'}^\dagger d_{m\sigma} d_{m'\sigma'}. \tag{156}
\end{aligned}$$

We assume each impurity orbital $m(= 1, 2)$ has its own bath, thus $c_{km\sigma}^\dagger$ ($c_{km\sigma}$) creates (annihilates) bath electrons, with wavevector k in band m (associated with impurity orbital m) and spin σ . $d_{m\sigma}^\dagger$ ($d_{m\sigma}$) creates (annihilates) the impurity (d) electron with spin σ in orbital m , ϵ_{dm} is the bare energy of the impurity orbital m and V_{km} is the hopping between impurity orbital m and its connected bath. $n_{m\sigma} = d_{m\sigma}^\dagger d_{m\sigma}$, $n_m = \sum_{\sigma} d_{m\sigma}^\dagger d_{m\sigma}$ and $n_d = \sum_{\sigma m} d_{m\sigma}^\dagger d_{m\sigma}$. The intra-orbital and the inter-orbital

Coulomb repulsion denoted by U and U' , respectively, are related by $U' = U - 2J_H$. J_H is the so-called Hund's rule coupling originating in the intra-atomic exchange interaction $J_H = \langle 1, 2 | V_{ee} | 2, 1 \rangle$. The Hund's rule coupling lowers the cost in repulsive Coulomb energy when placing two electrons in different orbitals with parallel spin, as opposed to two electrons in the same orbital^{100,101} as can be seen by rewriting the last term of eq. (156) in terms of an explicit spin-spin interaction (see appendix):

$$\begin{aligned}
H_{\text{impurity}} &= \sum_{m\sigma} \epsilon_{dm} d_{m\sigma}^\dagger d_{m\sigma} + U \sum_m n_{m\uparrow} n_{m\downarrow} \\
&+ \left(U' - \frac{J_H}{4} \right) \sum_{m \neq m' \sigma \sigma'} n_{m\sigma} n_{m'\sigma'} - J_H \sum_{m \neq m'} \vec{S}_m \cdot \vec{S}_{m'}. \quad (157)
\end{aligned}$$

The last term explicitly shows that for $J_H > 0$, parallel alignment of the spins of impurity electrons in different orbitals results in lowering the impurity energy.

6.2 DED for the multi-orbital model

In order to generate finite Anderson model samples we proceed in the same way as for the single impurity level case, described in Sec. 3.2: For each impurity level a finite number of poles is generated randomly according to the probability distribution given by the non-interacting density of states for each impurity level m , $\rho_{0m}(\omega) = -\text{Im}[G_{0m}(\omega)]/\pi$. Note that in the non-interacting case we are dealing with two *uncoupled* single-level Anderson models. Hence the set of poles for each impurity level uniquely defines a finite single-level Anderson model. When switching on the Coulomb interaction (U' , J_H), the two Anderson model become coupled. We now make a further simplification and assume that both impurity levels are degenerate, i.e. $\epsilon_{d1} = \epsilon_{d2}$ and $\Delta_1(\omega) = \Delta_2(\omega)$ and consequently $\rho_{01}(\omega) = \rho_{02}(\omega)$. Hence we only generate one set of poles which defines the finite Anderson models of both impurity levels. More precisely, we randomly generate $n/2$ poles according to the non-interacting density of states $\rho_{0m}(\omega) = -\text{Im}[G_{0m}(\omega)]/\pi$, and we then follow eq. (91), eq. (92), eq. (93) and eq. (94) (with $n \rightarrow n/2$), to extract the impurity and bath level energies as well as the hoppings for subsystem 1. The same data is finally also used for subsystem 2:

$$\begin{aligned}
\epsilon_{01}^\nu &= \epsilon_{02}^\nu \\
\epsilon_{k1}^\nu &= \epsilon_{k2}^\nu \quad \forall k = 1, \dots, n/2 - 1 \\
V_{k1}^\nu &= V_{k2}^\nu \quad \forall k = 1, \dots, n/2 - 1. \quad (158)
\end{aligned}$$

The non-interacting part of the finite size (n sites) Anderson model is defined:

$$H_0^\nu = \sum_{\sigma m} \epsilon_{0m}^\nu d_{m\sigma}^\dagger d_{m\sigma} + \sum_{\sigma, k=1}^{n-1} V_{km}^\nu (d_{m\sigma}^\dagger c_{km\sigma} + c_{km\sigma}^\dagger d_{m\sigma}) + \sum_{\sigma, k=1}^{n-1} \epsilon_{mk}^\nu c_{km\sigma}^\dagger c_{km\sigma}. \quad (159)$$

The interacting finite Anderson model is obtained by adding the two-body interaction part and subtracting out the effective one body potential Σ_0 to avoid double counting of interactions:

$$H^\nu = H_0^\nu + \sum_m U n_{m\uparrow} n_{m\downarrow} + \left(U' - \frac{J_H}{4} \right) \sum_{m \neq m' \sigma \sigma'} n_{m\sigma} n_{m'\sigma'} - J_H \sum_{m \neq m'} \vec{S}_m \cdot \vec{S}_{m'} - \sum_m \Sigma_0 n_m \quad (160)$$

The rest of the DED scheme for the two-orbital Anderson model is analogous to the single impurity Anderson model: The finite Anderson model Hamiltonian H^ν is diagonalized numerically to give the

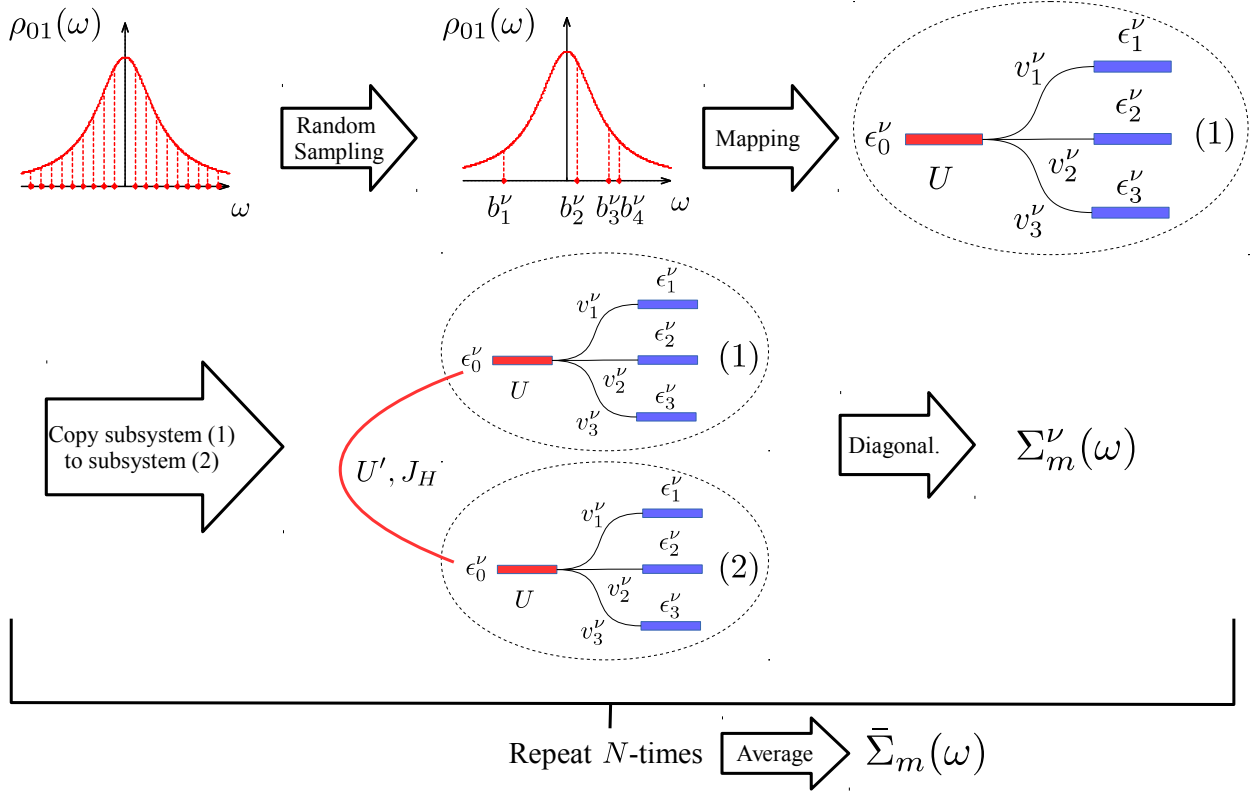


Figure 18: Schematic representation of the DED method for the two-orbital Anderson model: The non-interacting density of states of the impurity level m , $\rho_{0m}(\omega)$ is interpreted as a probability distribution for the poles of the non-interacting Green's function $G_{0m}(\omega)$. Since both subsystems are the same $\rho_{01}(\omega) = \rho_{02}(\omega)$, a finite number of poles b_i^ν is generated randomly according to the distribution $\rho_{01}(\omega)$. The selected $n/2$ poles uniquely define a finite single Anderson model for subsystem 1 with $n/2 - 1$ bath sites. The data of the first subsystem is then copied to subsystem 2, and finally by adding U , U' and J_H the finite size two-orbital Anderson model H^ν including two subsystems is completed. Diagonalization of H^ν yields the self-energy $\Sigma_m^\nu(\omega)$ corresponding to the finite two-orbital Anderson model. This process is repeated many times (N). An approximation to the self-energy of the original infinite Anderson model (156) is obtained from the ensemble average of the self-energies of the finite Anderson model samples (162).

many-body eigenstates and the corresponding eigenenergies. The interacting Green's function is then determined by the Lehmann representation and the corresponding self-energy of the finite Anderson model per impurity level is calculated by,

$$\Sigma_{\sigma m}^{\nu}(\omega) = (G_{0m}^{\nu}(\omega))^{-1} - (G_{\sigma m}^{\nu}(\omega))^{-1} + \Sigma_0. \quad (161)$$

Finally, the approximated self-energy for each impurity is obtained from the ensemble average:

$$\bar{\Sigma}_{m\sigma}(\omega) = \frac{1}{N} \sum_{\nu=1}^N \Sigma_{m\sigma}^{\nu}(\omega). \quad (162)$$

Fig. 18 depicts the DED scheme applied to the two-orbital Anderson model as discussed above. It should be mentioned that only samples ν which satisfy the particle constraint *per subsystem* i.e. $N_1^{\nu} = N_{01}^{\nu}$ and $N_2^{\nu} = N_{02}^{\nu}$, contribute to the ensemble averaged self-energy. This ensures that each subsystem obeys Fermi liquid behaviour, and the corresponding screening of the spin in each subsystem. Imposing the particle constraint to the whole system ($N^{\nu} = N_0^{\nu}$) would allow the contribution of samples with $N_m^{\nu} = N_{0m}^{\nu} \pm 1$, leading to the violation of Fermi liquid behaviour in each subsystem (see Sec. 3.3).

The Hund's rule coupling (intra-atomic exchange) is known to be responsible for strong correlations in multi-orbital metallic materials.¹⁰¹ Thus in order to explore the effect of Hund's rule coupling we study the two-orbital Anderson model $m = 1, 2$ both in the presence and absence of Hund's coupling in the Kondo regime. In this regime the characteristic three peak structure of the spectral density is expected to retain. In the presence of Hund's coupling we present the DED results for the fully screened as well as the underscreened half-filled two-orbital Anderson model (spin-1 impurity).

In the calculations a constant hybridization function with the same value for each impurity level is assumed $\Delta_m = -i\Gamma$, thus the non-interacting density of states $\rho_{0m}(\omega)$ is a Lorentzian centered at $\epsilon_d + \Sigma_0$. To resolve the interacting spectral functions we use a logarithmic mesh, and a frequency dependent Lorentzian broadening scheme where an imaginary part proportional to the frequency is added to the frequency argument in the denominators of the Green's functions, i.e. $\omega^+ = \omega + i\eta_1 \cdot |\omega|$ with $\eta_1 = 0.02$. The DED results are benchmarked by comparison with NRG results.

6.3 Two-orbital Anderson model without Hund's rule coupling

First, we study the two-orbital Anderson model when the Hund's coupling is set to zero, i.e. $J_H = 0$ and $U = U'$. The half-filled ($n_d = 2$ and $\epsilon_{dm} = -3U/2$) and the quarter-filled ($n_d \approx 1$ and $\epsilon_{dm} = -U/2$) cases are considered. Fig. 19 shows the impurity spectral density $\rho_m(\omega) = -\frac{1}{\pi} \text{Im} G_m(\omega)$ for the half-filled impurity for $\Gamma = 0.3$, $U = U' = 3$ and $\epsilon_d = -4.5$ calculated by DED with $n = 6$ ($n_m = 3$) and $n = 8$ ($n_m = 4$) in comparison with the NRG spectrum. In this case the real part of the self-energy $\Sigma_0 = -3U/2$ is known prior to the calculations, so it does not need to be determined self-consistently. As can be seen the DED and NRG spectra are in very good agreement with each other, especially at low energies, i.e. the Kondo peak (see the inset), already for a few bath sites per subsystem $n_m = 3$ ($n = 6$). By adding one more bath site to each subsystem i.e. $n_m = 4$ ($n = 8$), the DED Kondo peak is basically on top of the NRG one. However, the side peaks practically do not change and remain above the NRG ones. One should bear in mind though that the NRG results which are very reliable and essentially exact at low energies, are not necessarily as accurate at high energies. It clearly can be seen

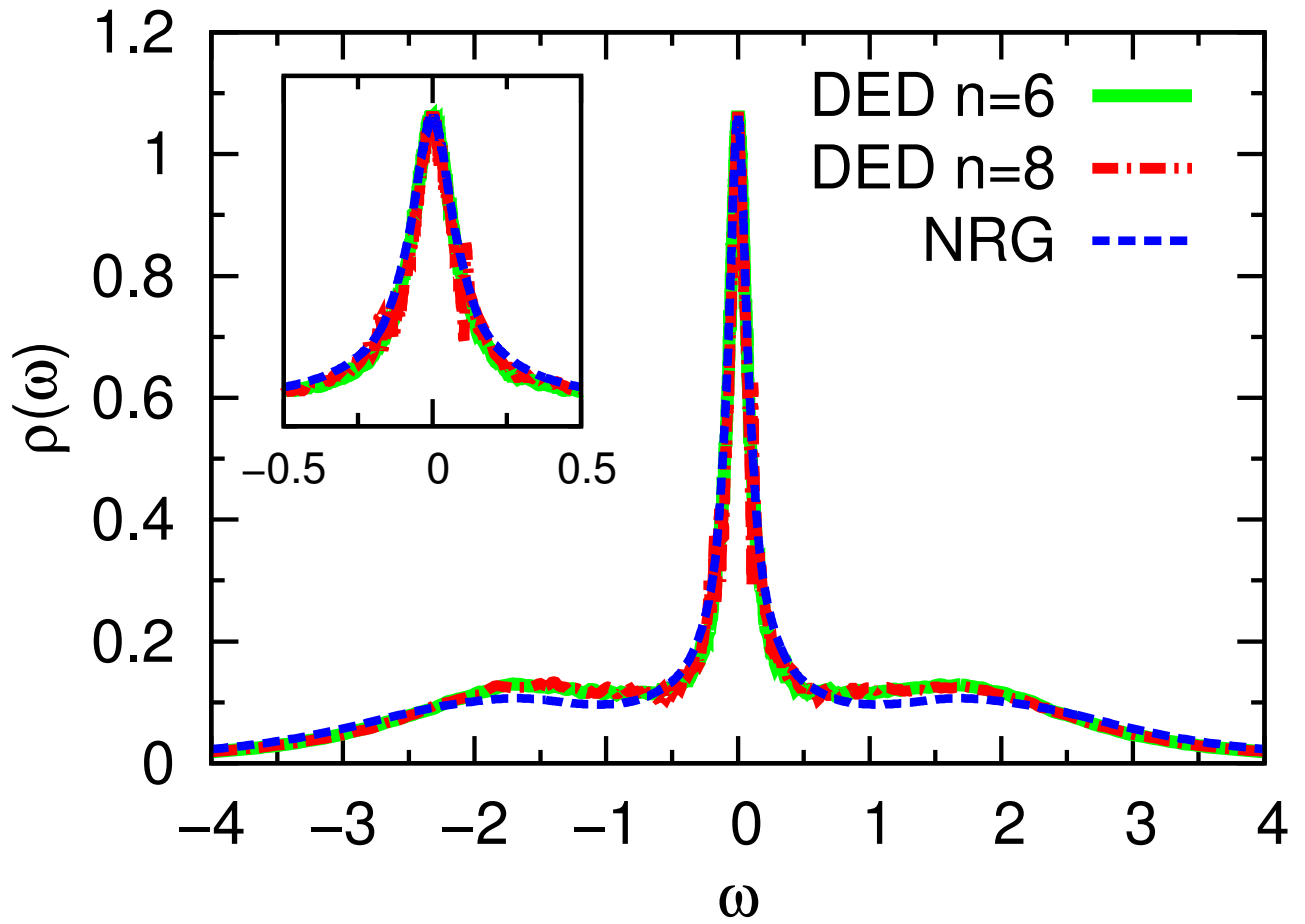


Figure 19: Comparison of DED $n = 6$, $n = 8$ and NRG spectra for the half-filled two-orbital Anderson model without Hund's rule coupling ($\epsilon_d = -4.0$, $U = 3.5$, $U' = 3.5$, $J_H = 0$, $\Gamma = 0.3$).

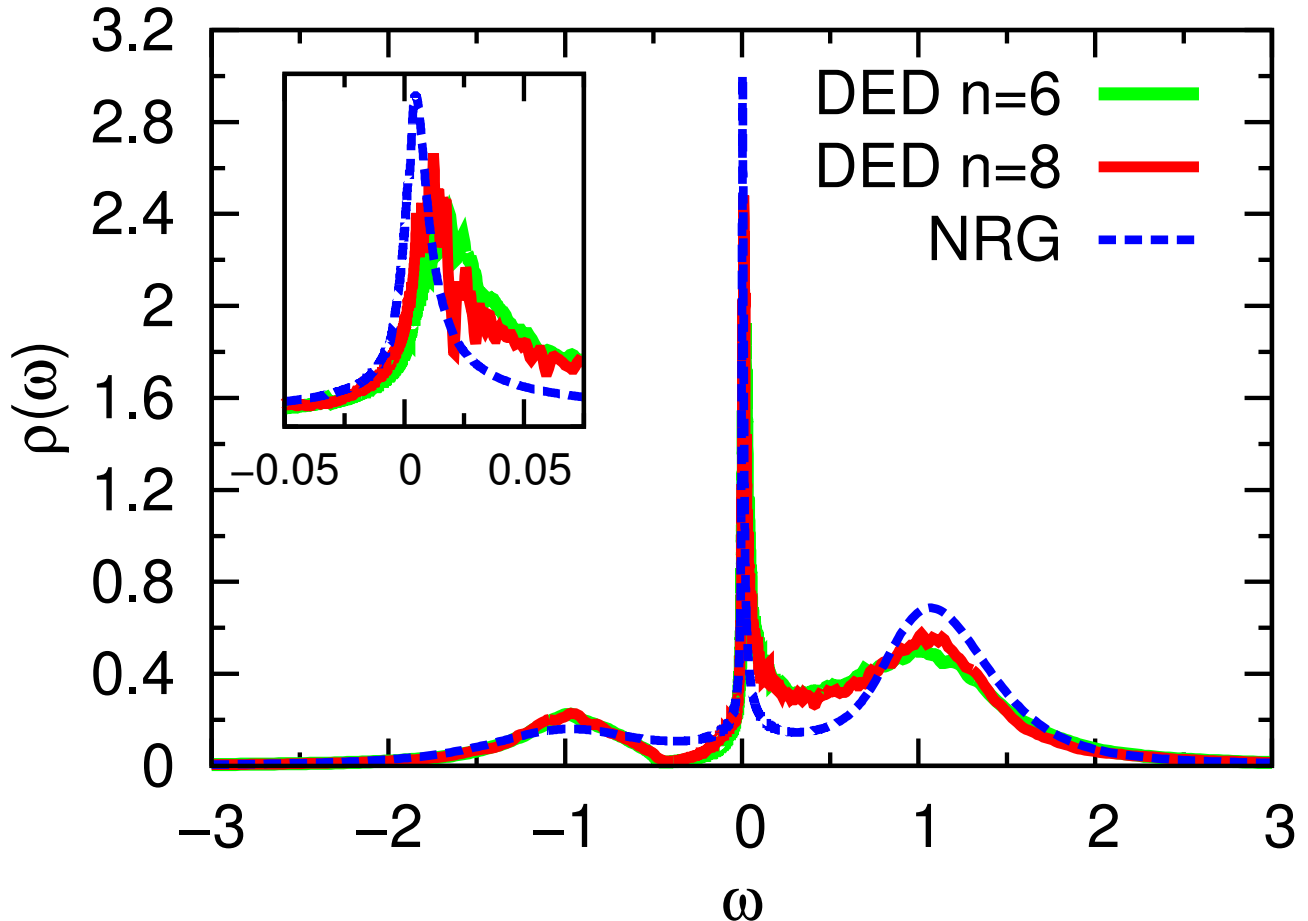


Figure 20: Comparison of DED $n = 6$, $n = 8$ and NRG spectra for the quarter filled two-orbital Anderson model without Hund's rule coupling ($\epsilon_d = -1$, $U = 2$, $U' = 2$, $J_H = 0$, $\Gamma = 0.096$).

that the correlation effects here are not so strong: the Kondo peak is quite wide and the side peaks are not yet very pronounced. Therefore already a small number of bath sites ($n_m = 3$ per subsystem) suffices to describe the correct behaviour.

In Fig. 20 we show the spectral density $\rho_m(\omega) = -\frac{1}{\pi} \text{Im} G_m(\omega)$ for the quarter-filled impurity for $\Gamma = 0.096$, $U = U' = 2$ and $\epsilon_d = -1$ calculated by DED with $n = 6$ ($n_m = 3$) and $n = 8$ ($n_m = 4$) in comparison with the NRG spectrum. The d orbital occupancy computed by DED via the ensemble average is $\langle n_d \rangle = 1.028$. In this case the larger size of the Hilbert space for the one electron more subspace i.e. $n_d = 2$ compared to the one electron less subspace i.e. $n_d = 0$ leads to an asymmetric spectrum, as can be seen. Therefore the real part of the self-energy Σ_0 is not known in advance and it should in principle be determined self-consistently. However, the spectrum is relatively noisy as can be seen in the inset which makes it relatively hard to obtain the exact value of Σ_0 , but we find roughly $-\epsilon_d$. As we saw in Sec. 4.3 that anyway the effect of self-consistency is actually not that strong, we perform the calculations for $\Sigma_0 = \epsilon_d = -U/2$. The overall qualitative agreement between DED and NRG spectra is OK. However, even for $n = 8$ it is more asymmetric compared to NRG and the Kondo peak is slightly misplaced. Due to the little shift in the Kondo peak position, also the height of the Kondo peak may not be captured accurately, as a frequency dependent broadening scheme has been used. While the position of the Hubbard sided peaks is well reproduced, their height

is somewhat underestimated by DED. On the other hand, in the region between the Kondo peak and the upper Hubbard peak DED somewhat overestimates the spectral density, while it is underestimated just below the Kondo peak. The lack of quantitative agreement can be understood by the fact that the correlation strength is very strong here: $U/\Gamma \approx 20$. Therefore according to Sec. 4.1 the number of bath sites considered here, apparently is too small to correctly describe the Kondo screening cloud. Indeed, as can be seen from Fig. 20, increasing the number of sites from $n = 6$ (red curve) to $n = 8$ (green curve), considerably improves the DED spectrum with respect to the NRG one: the Kondo peak moves towards the Fermi energy and increases in height (as can be seen in the inset). Also the side peak at $U/2 = 1$ gains more weight and becomes more pronounced. Hence, we expect that by further increasing the number of bath sites better agreement with the NRG spectrum could be achieved.

6.4 Two-orbital Anderson model with Hund's rule coupling: the fully screened case

In the next step we focus on the case where the two orbitals experience a ferromagnetic Hund's coupling. In the atomic limit ($V = 0$) and when there is no Hund's coupling $J_H = 0$, the ground state is six fold degenerate. A finite $J > 0$ leads to the splitting of the sextuplet into a spin triplet ($S = 1$) as the ground state and a spin singlet ($S = 0$). In the two impurity spin-1 system if both impurities being completely screened the situation is known as the fully screened Kondo effect.

In Fig. 21 we show the spectral density per impurity level $\rho_m(\omega) = -\frac{1}{\pi} \text{Im} G_m(\omega)$ for the fully screened two-orbital Anderson model at particle-hole symmetry ($n_d = 2$ and $\epsilon_d = -U/2 - U' + J_H/2$) for $\Gamma = 0.3$, $U = 3.5$, $U' = 2.5$ and $J_H = 0.5$ calculated by DED with $n = 6$ ($n_m = 3$) and $n = 8$ ($n_m = 4$), in comparison to the NRG spectrum. In the inset of Fig. 21 we zoom into the Kondo peak to better resolve the spectra at low energies. Comparing the current spectrum with the case of no Hund's rule coupling (Fig. 19), clearly indicates that the presence of the Hund's rule coupling leads to stronger correlations: the width of the Kondo peak strongly shrinks and the side peaks become more pronounced for $J_H > 0$. For this reason the DED spectrum only agrees qualitatively with the NRG spectrum, as can be seen. The quantitative agreement especially at low energies is not as good as for the symmetric two-orbital Anderson model with no Hund's coupling or the single orbital Anderson model: the half width of the Kondo peak is overestimated by an order of magnitude. Comparing the half width of the Kondo peak in the NRG spectra for the fully screened two-orbital Anderson model ($\Gamma_K = 0.0003$) and the single orbital Anderson model ($\Gamma_K = 0.024$) indicates that the Kondo temperature is much lower here (two orders of magnitude), so that the number of bath sites necessary to correctly describe the Kondo screening cloud is much larger, due to the greater spatial extent of the Kondo screening cloud $\xi_K \propto 1/T_K$ (see Sec. 4.1). In spite of this less bath sites per subsystem ($n_m = 4$) is actually been used compared to the case of the SAIM ($n = 8$), thus leading to the strong overestimation of the Kondo peak's half-width in the DED result. In the inset of Fig. 21, it can be seen that the width of the Kondo peak decreases with adding one more bath site to each subsystem, $n_m = 4$ ($n = 8$). On the other hand at higher energies around $2J_H = 1$, the DED spectrum is wavy and its side peaks are below the NRG side peaks. Those features only slightly improve by adding more bath sites. One can relate them to either not having sufficient bath sites in DED to get smooth spectra, or to less accuracy of the NRG results at higher energies, or both.

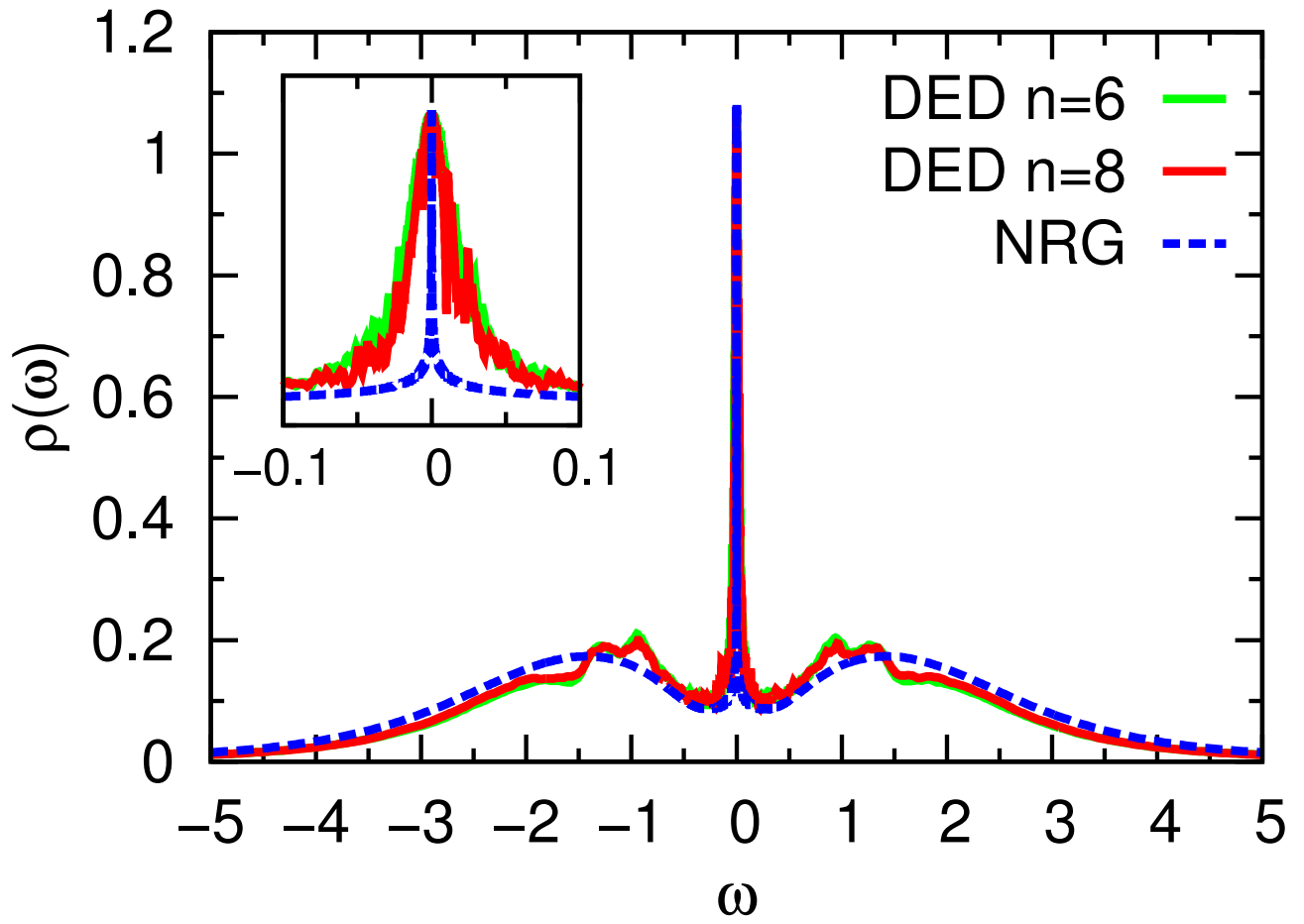


Figure 21: Comparison of DED $n = 8$ and NRG spectra for the two-orbital Anderson model including Hund's rule coupling ($\epsilon_d = -4.0$, $U = 3.5$, $U' = 2.5$, $J_H = 0.5$, $\Gamma = 0.3$).

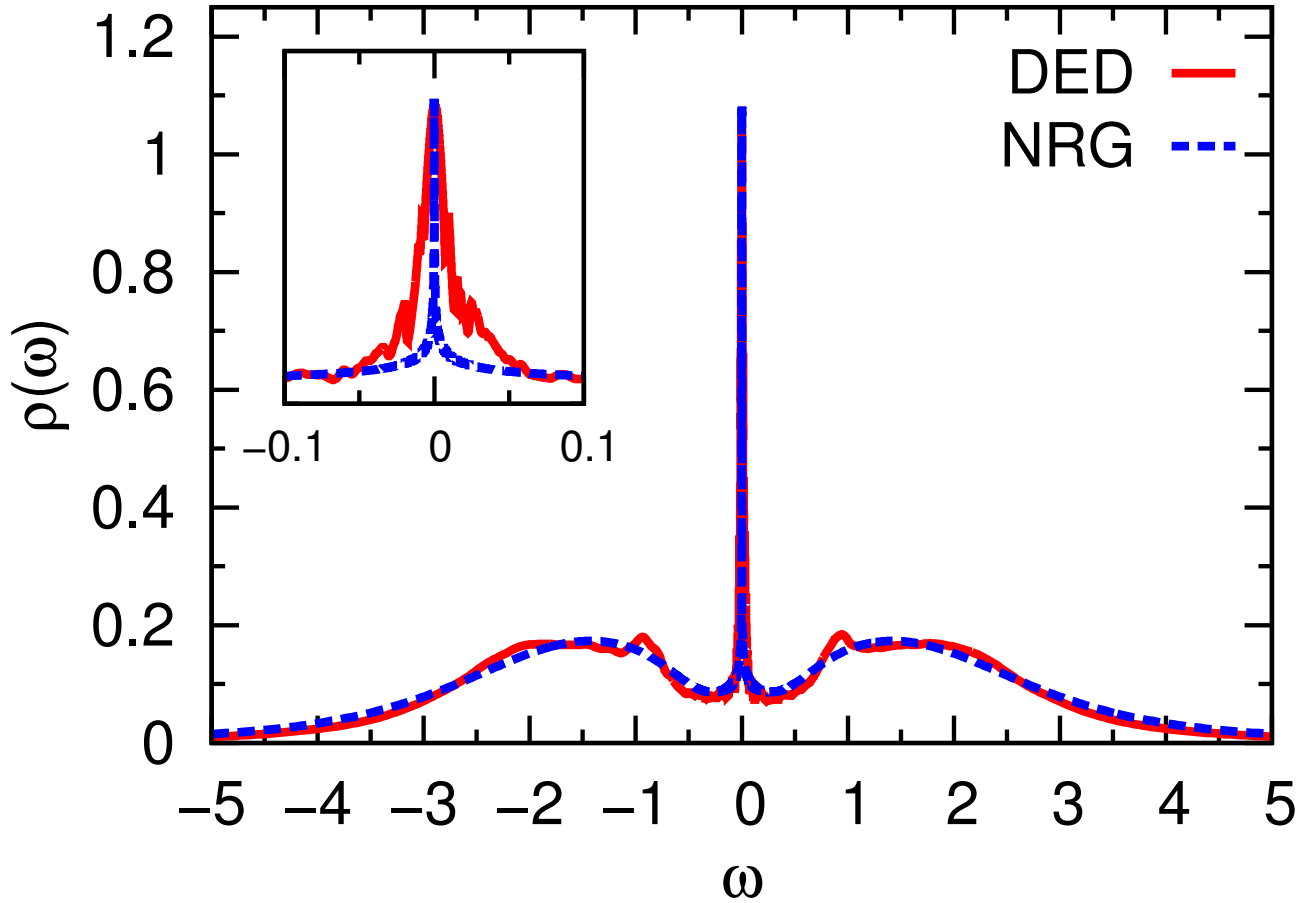


Figure 22: Comparison of DED $n = 8$ and NRG spectra for the two-orbital Anderson model including Hund's rule coupling ($\epsilon_d = -4.0, U = 3.5, U' = 2.5, J_H = 0.5, \Gamma = 0.3$) with selective self-energies as a constraint.

Another reason for the strong overestimation of the Kondo peak by DED, might also lie in the constraint. A too strong constraint might assign too large weight to the Kondo peak in the spectra. In order to somehow relax the constraint in the fully screened two-orbital Anderson model, we now do the DED calculations a bit differently, by doing sampling for each subsystem 1 and 2 independently, so that subsystems can have different energies and hoppings and additionally allowing self-energies to contribute to the ensemble-average individually. More precisely, if for instance in subsystem 1 the particle constraint is fulfilled, $N_1' = N_{01}'$, the self-energy of subsystem 1 will contribute to the ensemble average of level 1 and the self-energy of the other level remains unchanged, or the other way round. This results in the spectral density $\rho_m(\omega) = -\frac{1}{\pi} \text{Im} G_m(\omega)$ for the fully screened two-orbital Anderson model at particle-hole symmetry ($n_d = 2$ and $\epsilon_d = -U/2 - U' + J_H/2$) with the same set of parameters as before with $n = 8$ ($n_m = 4$) shown in Fig. 22. For better comparison in the inset we also present a close-up of the Kondo peak. The overall agreement between the DED and NRG spectrum improves. The width of the Kondo peak is reduced by a factor of 2 but is still quite overestimated compared to NRG. The side peaks are now in very good agreement with NRG, apart from the two bumps at the excitation energies corresponding to $\pm 2J_H$ which are exaggerated by DED, possibly due to the finite number of bath sites. The justification for this way of relaxing the constraint is not yet clear to us. Now somehow also “underscreened situations” (see following section) contribute to the self-energy average. These are doublet states where only the impurity level is screened which fulfills the particle constraint, while the other impurity which does not fulfill the constraint is not screened, but will not contribute to the self-energy average of that level either.

6.5 Two-orbital Anderson model with Hund’s rule coupling: the underscreened case

Finally, we study the underscreened Kondo effect. In the case where the two orbitals experience a strong ferromagnetic Hund’s rule, the triplet configuration constitutes the ground state of the isolated impurity. This can result in the spin $S = 1$ underscreened Kondo effect if only a single screening channel is active, as initially proposed by Nozieres and Blandin,¹⁰² and only recently experimentally observed.^{103–105} This rather exotic Kondo effect describes the partial screening of a local moment from spin S to spin $S - 1/2$ and to so-called singular Fermi liquid behaviour.¹⁰⁶

In order to model the underscreened situation within DED, the subsystem 1 is considered as a single impurity Anderson model, consisting of an impurity level which interacts with its surrounding bath like before, while subsystem 2 is only an impurity level which does not couple to the bath directly but only indirectly via impurity level 1 inter-orbital Coulomb interaction U' and Hund’s rule coupling J_H . We extract the parameters of subsystem 1 via the DED formalism for the single Anderson model and then to guarantee the screening of the impurity level 1 we enforce the particle constraint to the subsystem 1. In addition, in subsystem 2 we fix the impurity level to be always half-filled at a fixed on-site energy given by, $\epsilon_d = -U/2 - U' + J_H/2$.

We show the spectral density $\rho_1(\omega) = -\frac{1}{\pi} \text{Im} G_1(\omega)$ for the screened impurity at particle-hole symmetry ($n_d = 2$ and $\epsilon_d = -U/2 - U' + J_H/2$) for $\Gamma = 0.3$, $U = 3.5$, $U' = 2.5$ and $J_H = 0.5$ with $n = 5$ ($n_1 = 4, n_2 = 1$), $n = 7$ ($n_1 = 6, n_2 = 1$) calculated by DED, in comparison to the NRG spectrum. The DED spectrum for $n = 8$ is in very good agreement with the NRG spectrum

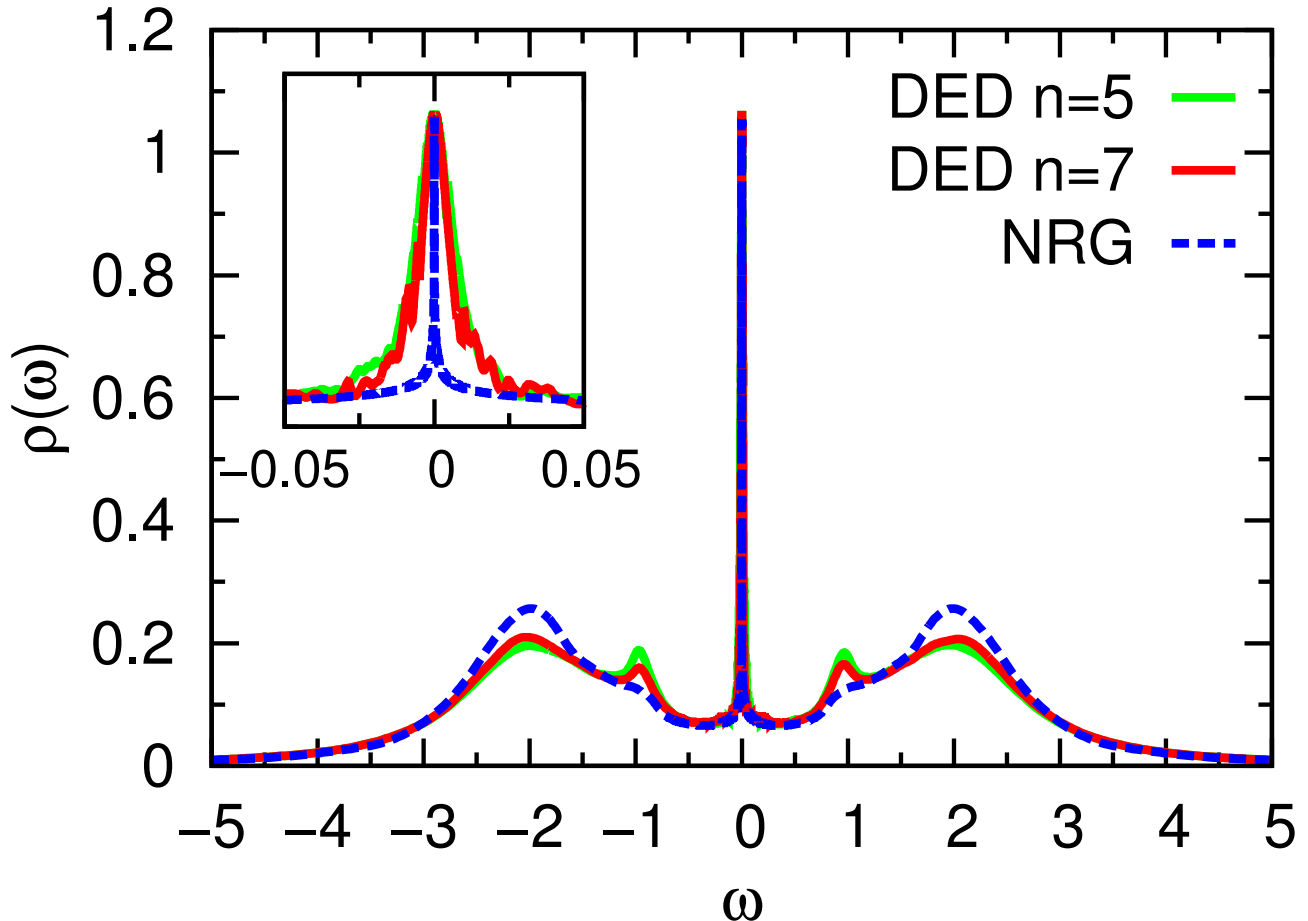


Figure 23: Comparison of DED (with $n = 7$, $n = 5$) and NRG spectra for the underscreened two-orbital Anderson model including Hund's rule coupling ($\epsilon_d = -4.0$, $U = 3.5$, $U' = 2.5$, $J_H = 0.5$, $\Gamma = 0.3$).

especially at high energies i.e. side peaks. At energies $\pm 2J_H$ in the DED spectra, two bumps can be seen while they are more shoulder like in the NRG spectrum. However, at low energies, the width of the Kondo peak is again strongly overestimated: The half-width of the DED Kondo peak for $n = 8$ is approximately 10^{-2} while it is 10^{-4} for NRG. In this case the Kondo peak (according to NRG result) is very narrow, hence the size of the Kondo screening cloud should be rather huge. Thus, in order to obtain the correct width of the Kondo peak we would need to take into account a much bigger number of bath sites. The improvement of the DED spectrum with increasing the number of bath sites i.e. the side peaks are approaching NRG's and the Kondo peak slightly shrinks in width (see inset), further vouches that.

6.6 Discussion

To summarize, in the absence of Hund's coupling, DED yields an excellent description of the symmetric two-orbital Anderson model already for a small number of bath sites, although for the asymmetric case with the impurity occupancy of almost 1, there is room for improvement. In this case small number of sites per subsystem (4) is not enough to achieve quantitative agreement with NRG. This is also the case when the two impurity orbitals experience Hund's coupling, the width of the Kondo peak becomes very

narrow in both fully screened and underscreened situations, meaning that due to the strong correlation strength the corresponding Kondo temperature is very low for both cases. Consequently, the number of bath sites necessary to achieve a good quantitative description becomes too big to be computationally feasible (with the direct diagonalization), due to the growth of the Kondo screening cloud according to $\xi_K \propto 1/T_K \propto e^{\Gamma/U}$. Direct diagonalization only allows to deal with a finite size Anderson model of size $n = 8$, which is already enough to accurately describe the single AIM inside and outside the Kondo regime, but it is too small to achieve accurate results for the two-orbital AIM, as it is equivalent to the size of $n_m = 4$ per subsystem. Thus, adoption of the Lanczos diagonalization scheme or similar approaches in the DED seems necessary and would possibly allow to treat multi-orbital Anderson models with a sufficient number of bath sites per impurity level.⁶⁴

On the other hand, inasmuch as the particle constraint has an essential role in the DED method for the description of Kondo physics (this has been extensively discussed in the single impurity Anderson model), it may need to be adapted for multi-orbital Anderson models. As the particle constraint by construction assigns more spectral weight to the Kondo peak, finding a way to somehow relax or adapt the particle constraint (e.g. like the finite temperature calculations) may lead to achieve more accurate results even with currently accessible number of bath sites. The constraint adaptation is even more crucial for cases where non Fermi liquid behaviour emerges, possibly also important for the underscreened case which shows “singular Fermi liquid behaviour“, since the particle constraint imposes Fermi liquid behaviour.

7 Conclusions and perspectives

In this thesis we have implemented the distributional exact diagonalization (DED) scheme, which is based on mapping the infinite Anderson problem onto a stochastic ensemble of finite Anderson models. We find that the DED method generally yields an excellent description of the single orbital Anderson model, inside as well as outside the Kondo regime. The spectra obtained by DED are in good qualitative agreement with NRG spectra already for a small number of bath sites. In the regime of moderate correlation strength, excellent quantitative agreement with NRG can be achieved by including 5-7 bath sites. However, increasing the correlation strength, the number of bath sites necessary to achieve a good quantitative description becomes too big to be computationally feasible due to the exponential growth of the Kondo screening cloud.

We also find that the particle constraint plays an essential role in the DED method for the description of Kondo physics. It basically ensures that individual finite Anderson model samples contributing to the self-energy average, comply with Nozieres' Fermi liquid picture of the strong coupling regime, thereby imposing Fermi liquid behavior on the sample averaged self-energy. This leads to the recovery of the Kondo peak in the spectrum, which is absent in the DED procedure without constraint.

Since the particle constraint enforces Fermi liquid behaviour, imposing it to cases where Fermi liquid behavior is not obeyed, for example, at finite temperatures above T_K , gives rise to too much spectral weight at the Fermi level. Hence, the role of the particle constraint needs to be reconsidered when DED is applied to non Fermi liquid situations. To achieve the correct temperature evolution of spectra the particle constraint needs to be relaxed, in order to reduce the Kondo peak's weight in the spectral density. To this end, we introduce a Boltzmann factor associated with the energy scale for breaking the Kondo singlet, which determines the weight of a sample contributing to the ensemble-average quantities. Relaxing the constraint in this way allows to capture the correct evolution of the Kondo peak by DED, when the temperature is raised: from below to not much far above the Kondo temperature the agreement between DED and NRG becomes very good already for a small number of bath sites ($n = 4$). However, at very high temperatures the quality of the DED spectra considerably degrades for such a small number of bath sites. Apparently, the number of sites needs to be increased further in order to achieve a faithful description of the spectra at high temperatures.

Using this relaxation mechanism for the particle constraint, we also investigated the thermodynamic properties, specifically the impurity contribution to the entropy of the symmetric Anderson model. We find that with the current feasible number of bath sites, agreement between the DED sample-averaged impurity entropy and the NRG impurity entropy remains only qualitative. The DED failure to achieve good quantitative agreement with NRG (in the impurity entropy calculations) is possibly related to our direct sample averaging of the impurity entropy: as the DED formalism is constructed to acquire a good approximation to the self-energy, other quantities should actually be calculated via the self-energy (like the Green's function). For example, the free energy could be calculated as a functional of the self-energy, from which other thermodynamic quantities could then be derived.

A big advantage of DED is that it can be parallelized very efficiently. As the randomly generated finite Anderson model samples are independent from each other, they can be distributed over an arbitrary large number of nodes. This makes the DED formalism very desirable to be applied to the multi-orbital Anderson models. As a first choice of the multi-orbital calculations we studied the two-

orbital Anderson model. To ensure screening of each impurity level or equivalently the Fermi liquid behaviour the particle constraint is imposed to each subsystem (which includes single impurity level and the coupled bath). We find that in the absence of Hund's rule coupling DED yields very good agreement with NRG for the two-orbital Anderson model as long as the correlation strength is not too strong. However, switching on the Hund's rule coupling leads to a strong increase in the correlation strength as is indicated by the very narrow Kondo peak in the NRG spectrum for the fully screened Kondo effect. Hence the size of the Kondo correlation cloud becomes too big to be treated with the currently accessible number of bath sites. The DED spectrum is in overall good qualitative agreement with the NRG spectrum but the width of the Kondo peak is strongly overestimated in DED by orders of magnitude.

Thus in the presence of strong correlations, e.g. the single orbital Anderson model with $U/\Gamma \gg 10$ and in the two-orbital Anderson model including Hund's rule coupling, the number of bath sites in the finite Anderson model samples needs to be increased in order to enable the DED method to achieve good quantitative agreement with NRG. Therefore the adoption of other algorithms such as the Lanczos diagonalization scheme instead of the direct diagonalization seems necessary. This should then allow to treat multi-orbital Anderson models with a sufficient number of bath sites per impurity level. Also the constraint as a crucial ingredient of DED may need to be generalized in the multi-orbital case, especially for non Fermi liquid situations. As in the case of relaxing the constraint in the fully screened Kondo effect, generalizing the constraint might even allow to obtain more accurate results in Fermi liquid systems with few bath sites.

Adoption of the Lanczos algorithm and/or generalizing the particle constraint should enable the DED approach, which can be easily implemented and efficiently parallelized, to treat multi-orbital Anderson models. Using NRG to solve Anderson models with 2-3 impurity levels is computationally very demanding and not accessible for more than three impurity levels. Other impurity solvers have also problems in dealing with multi-orbital Anderson models: NCA and OCA are burdened with some artifacts in the spectra due to the involved approximations, and CTQMC which can also be parallelized efficiently has the disadvantage of working on the imaginary axis. Thus, a properly generalized DED scheme should allow to produce reliable spectra for multi-orbital systems which can be exploited for the description of real materials by DMFT.

A Derivation of Hund's rule coupling

The Hund's rule coupling between electrons in the same atomic shell stems from the exchange interaction that tries to align the spins of electrons in different levels of the same atomic shell. The exchange part of the Coulomb interaction is given by:

$$\begin{aligned}
\hat{V}_{ex} &= \frac{1}{2} \sum_{m \neq m' \sigma \sigma'} U_{mm'm'm} c_{m\sigma}^\dagger c_{m'\sigma'}^\dagger c_{m\sigma'} c_{m'\sigma} \\
&= -\frac{1}{2} \sum_{m \neq m' \sigma \sigma'} U_{mm'm'm} c_{m\sigma}^\dagger c_{m\sigma'} c_{m'\sigma'}^\dagger c_{m'\sigma} \\
&= -\frac{1}{2} \sum_{m \neq m'} U_{mm'm'm} (c_{m\uparrow}^\dagger c_{m\uparrow} c_{m'\uparrow}^\dagger c_{m'\uparrow} + c_{m\downarrow}^\dagger c_{m\downarrow} c_{m'\downarrow}^\dagger c_{m'\downarrow} \\
&\quad + c_{m\downarrow}^\dagger c_{m\uparrow} c_{m'\uparrow}^\dagger c_{m'\downarrow} + c_{m\uparrow}^\dagger c_{m\downarrow} c_{m'\downarrow}^\dagger c_{m'\uparrow})
\end{aligned} \tag{163}$$

By use of these identities, $\hat{S}_m^+ = c_{m\uparrow}^\dagger c_{m\downarrow}$, $\hat{S}_m^- = c_{m\downarrow}^\dagger c_{m\uparrow}$ we get:

$$\hat{V}_{ex} = \frac{1}{2} \sum_{m \neq m'} U_{mm'm'm} (\hat{n}_{m\uparrow} \hat{n}_{m'\uparrow} + \hat{n}_{m\downarrow} \hat{n}_{m'\downarrow}) \tag{164}$$

by making further use of $\hat{S}_m \cdot \hat{S}_{m'} = \hat{S}_m^z \hat{S}_{m'}^z + \frac{1}{2} S_m^+ S_{m'}^- + \frac{1}{2} S_m^- S_{m'}^+$, we can rewrite the exchange term as:

$$\hat{V}_{ex} = - \sum_{m \neq m'} U_{mm'm'm} (\hat{S}_m \cdot \hat{S}_{m'} + \hat{S}_m^z \hat{S}_{m'}^z - \frac{1}{2} (\hat{n}_{m\uparrow} \hat{n}_{m'\uparrow} + \hat{n}_{m\downarrow} \hat{n}_{m'\downarrow})) \tag{165}$$

The first term is the Hund's rule coupling term: since the exchange matrix element $U_{mm'm'm}$ is usually positive this term leads to energy lowering if spins in different levels m and m' align parallel. The last term gives a negative contribution to the inter-orbital Coulomb interaction (i.e. it lowers the repulsion between electrons in different orbitals):

$$\hat{S}_m^z \hat{S}_{m'}^z - \frac{1}{2} (\hat{n}_{m\uparrow} \hat{n}_{m'\uparrow} + \hat{n}_{m\downarrow} \hat{n}_{m'\downarrow}) = \frac{1}{4} (\hat{n}_{m\uparrow} - \hat{n}_{m\downarrow}) (\hat{n}_{m'\uparrow} - \hat{n}_{m'\downarrow}) - \frac{1}{2} (\hat{n}_{m\uparrow} \hat{n}_{m'\uparrow} + \hat{n}_{m\downarrow} \hat{n}_{m'\downarrow}) = -\frac{1}{4} N_m N_{m'} \tag{166}$$

where $N_m = n_{m\uparrow} + n_{m\downarrow}$ is the total occupation of atomic level m . If the exchange matrix element is the same for all orbitals in the atomic shell (often approximately true in bulk systems), i.e. $U_{mm'm'm} \equiv J_H$, we obtain the standard form of the Hund's rule coupling:

$$\hat{V}_{ex} = -J_H \sum_{m \neq m'} \hat{S}_m \cdot \hat{S}_{m'} - \frac{J_H}{4} \sum_{m \neq m'} N_m N_{m'} \tag{167}$$

References

- [1] Gabriel Kotliar and Dieter Vollhardt. Strongly correlated materials: Insights from dynamical mean-field theory. *Physics Today*, 57(3):53–60, 2004.
- [2] Masatoshi Imada, Atsushi Fujimori, and Yoshinori Tokura. Metal-insulator transitions. *Rev. Mod. Phys.*, 70:1039–1263, Oct 1998.
- [3] Antoine Georges, Gabriel Kotliar, Werner Krauth, and Marcelo J. Rozenberg. Dynamical mean-field theory of strongly correlated fermion systems and the limit of infinite dimensions. *Rev. Mod. Phys.*, 68:13–125, Jan 1996.
- [4] M. Amusia, K. Popov, V. Shaginyan, and W. Stefanowicz. *Theory of Heavy-Fermion Compounds: Theory of Strongly Correlated Fermi-Systems*. Springer Series in Solid-State Sciences. Springer International Publishing, 2014.
- [5] Gabriel Kotliar and Jialin Liu. Superexchange mechanism and d -wave superconductivity. *Phys. Rev. B*, 38:5142–5145, Sep 1988.
- [6] P W Anderson, P A Lee, M Randeria, T M Rice, N Trivedi, and F C Zhang. The physics behind high-temperature superconducting cuprates: the 'plain vanilla' version of rvb. *Journal of Physics: Condensed Matter*, 16(24):R755, 2004.
- [7] Arti Garg, Mohit Randeria, and Nandini Trivedi. Strong correlations make high-temperature superconductors robust against disorder. *Nature Physics*, 4(10):762–765, 2008.
- [8] A. C. Hewson. *The Kondo problem to heavy fermions*. Cambr. Univ. Press, Cambridge, 1997.
- [9] Leo Kouwenhoven and Leonid Glazman. Revival of the kondo effect. *Physics World*, 14(1):33, 2001.
- [10] Steffen Wirth and Frank Steglich. Exploring heavy fermions from macroscopic to microscopic length scales. *Nature Reviews Materials*, 1:16051, 2016.
- [11] P.J. Ford and G.A. Saunders. *The Rise of the Superconductors*. CRC Press, 2004.
- [12] Peter Fulde. *Electron correlations in molecules and solids*, volume 100. Springer Science & Business Media, 2012.
- [13] A Schilling, M Cantoni, JD Guo, and HR Ott. Superconductivity above 130 k in the hg-ba-ca-cu-o system. *Nature*, 363(6424):56–58, 1993.
- [14] P. W. ANDERSON. The resonating valence bond state in La_2CuO_4 and superconductivity. *Science*, 235(4793):1196–1198, 1987.
- [15] J. Kondo. Resistance minimum in dilute magnetic alloys. *Prog. Theor. Phys.*, 32:37, 1964.
- [16] V Yu Irkhin and Yu P Irkhin. Hybridization and kondo effect in systems with degenerate d and f shells. *Soviet Journal of Experimental and Theoretical Physics*, 80:334–340, 1995.

- [17] WJ De Haas, J De Boer, and GJ Van den Berg. The electrical resistance of gold, copper and lead at low temperatures. *Physica*, 1(7-12):1115–1124, 1934.
- [18] GJ Van Den Berg. Chapter iv anomalies in dilute metallic solutions of transition elements. *Progress in Low Temperature Physics*, 4:194–264, 1964.
- [19] David Goldhaber-Gordon, Hadas Shtrikman, D Mahalu, David Abusch-Magder, U Meirav, and MA Kastner. Kondo effect in a single-electron transistor. *Nature*, 391(6663):156–159, 1998.
- [20] David E. Logan, Christopher J. Wright, and Martin R. Galpin. Correlated electron physics in two-level quantum dots: Phase transitions, transport, and experiment. *Phys. Rev. B*, 80:125117, Sep 2009.
- [21] LI Glazman and ME Raikh. Resonant kondo transparency of a barrier with quasilocal impurity states. *ZhETF Pisma Redaktsiu*, 47:378, 1988.
- [22] Tai Kai Ng and Patrick A Lee. On-site coulomb repulsion and resonant tunneling. *Physical review letters*, 61(15):1768, 1988.
- [23] Arisato Kawabata. On the electron transport through a quantum dot. *Journal of the Physical Society of Japan*, 60(10):3222–3225, 1991.
- [24] Nicolas Roch, Serge Florens, Vincent Bouchiat, Wolfgang Wernsdorfer, and Franck Balestro. Quantum phase transition in a single-molecule quantum dot. *Nature*, 453(7195):633–637, 2008.
- [25] JJ Parks, AR Champagne, TA Costi, WW Shum, AN Pasupathy, E Neuscamman, S Flores-Torres, PS Cornaglia, AA Aligia, CA Balseiro, et al. Mechanical control of spin states in spin-1 molecules and the underscreened kondo effect. *Science*, 328(5984):1370–1373, 2010.
- [26] K. Andres, J. E. Graebner, and H. R. Ott. $4f$ -virtual-bound-state formation in CeAl_3 at low temperatures. *Phys. Rev. Lett.*, 35:1779–1782, Dec 1975.
- [27] Frithjof B Anders. 11 the kondo effect.
- [28] J. Hubbard. Electron correlations in narrow energy bands. *Proceedings of the Royal Society of London A: Mathematical, Physical and Engineering Sciences*, 276(1365):238–257, 1963.
- [29] Ferdinando Mancini, Evgeny Plekhanov, and Gerardo Sica. Exact solution of the 1d hubbard model in the atomic limit with inter-site magnetic coupling. *The European Physical Journal B*, 86(5):1–17, 2013.
- [30] Martin C Gutzwiller. Effect of correlation on the ferromagnetism of transition metals. *Physical Review Letters*, 10(5):159, 1963.
- [31] W. Metzner and D. Vollhardt. *Phys. Rev. Lett.*, 62:324, 1989.
- [32] Antoine Georges and Gabriel Kotliar. Hubbard model in infinite dimensions. *Phys. Rev. B*, 45:6479–6483, Mar 1992.

- [33] Antoine Georges, Gabriel Kotliar, Werner Krauth, and Marcelo J. Rozenberg. Dynamical mean-field theory of strongly correlated fermion systems and the limit of infinite dimensions. *Rev. Mod. Phys.*, 68:13, 1996.
- [34] G. Kotliar, S. Y. Savrasov, K. Haule, V. S. Oudovenko, O. Parcollet, and C. A. Marianetti. Electronic structure calculations with dynamical mean-field theory: A spectral density functional approach. *Rev. Mod. Phys.*, 78:865, 2006.
- [35] Ansgar Liebsch and Hiroshi Ishida. Temperature and bath size in exact diagonalization dynamical mean field theory. *Journal of Physics: Condensed Matter*, 24(5):053201, 2012.
- [36] P. W. Anderson. Localized magnetic states in metals. *Phys. Rev.*, 124:41, 1961.
- [37] R. Bulla, T. A. Costi, and Th. Pruschke. Numerical renormalization group method for quantum impurity systems. *Rev. Mod. Phys.*, 80:3950, 2008.
- [38] N. Grewe and H. Keiter. Diagrammatic approach to the intermediate-valence compounds. *Phys. Rev. B*, 24:4420, 1981.
- [39] P. Coleman. New approach to the mixed-valence problem. *Phys. Rev. B*, 29:3035, 1984.
- [40] T. Pruschke and N. Grewe. The anderson model with finite coulomb repulsion. *Z. Phys. B*, 74:439, 1989.
- [41] K. Haule, S. Kirchner, J. Kroha, and P. Wölfle. Anderson impurity model at finite coulomb interaction u: Generalized noncrossing approximation. *Phys. Rev. B*, 64:155111, 2001.
- [42] T. A. Costi, J. Kroha, and P. Wölfle. Spectral properties of the anderson impurity model: Comparison of numerical-renormalization-group and noncrossing-approximation results. *Phys. Rev. B*, 53:1850, 1996.
- [43] Norbert Grewe, Sebastian Schmitt, Torben Jabben, and Frithjof B Anders. Conserving approximations in direct perturbation theory: new semianalytical impurity solvers and their application to general lattice problems. *Journal of Physics: Condensed Matter*, 20:365217, 2008.
- [44] K. Yosida and K. Yamada. Perturbation expansion for the anderson hamiltonian. *Progress of Theoretical Physics*, 46:244, 1970.
- [45] N. Read and D. M. Newns. A new functional integral formalism for the degenerate anderson model. *J. Phys. C*, 16:L1055, 1983.
- [46] D. E. Logan, M. P. Eastwood, and M. A. Tusch. A local moment approach to the anderson model. *Journal of Physics: Condensed Matter*, 10:2673, 1998.
- [47] A. C. Hewson. Renormalized perturbation calculations for the single-impurity anderson model. *J. Phys. Condens. Matter*, 13:10011, 2001.
- [48] Q. Feng and P. M. Oppeneer. Fast multi-orbital equation of motion impurity solver for dynamical mean field theory. *Journal of Physics: Condensed Matter*, 23(42):425601, 2011.

- [49] E. Gull, A. J. Millis, A. I. Lichtenstein, A. N. Rubtsov, M. Troyer, and P. Werner. Continuous-time monte carlo methods for quantum impurity models. *Rev. Mod. Phys.*, 83:349, 2011.
- [50] Michel Caffarel and Werner Krauth. Exact diagonalization approach to correlated fermions in infinite dimensions: Mott transition and superconductivity. *Phys. Rev. Lett.*, 72:1545–1548, 1994.
- [51] A. Liebsch and H. Ishida. *J. Phys.: Condens. Matter*, 24:053201, 2012.
- [52] Y. Lu, M. Höppner, O. Gunnarsson, and M. W. Haverkort. Efficient real-frequency solver for dynamical mean-field theory. *Phys. Rev. B*, 90:085102, 2014.
- [53] M. Schüler, C. Renk, and T. O. Wehling. Variational exact diagonalization method for anderson impurity models. *Phys. Rev. B*, 91:235142, 2015.
- [54] M. Granath and H. U. R. Strand. Distributional exact diagonalization formalism for quantum impurity models. *Phys. Rev B*, 86:115111, 2012.
- [55] Mats Granath and Johan Schött. Signatures of coherent electronic quasiparticles in the paramagnetic mott insulator. *Phys. Rev. B*, 90:235129, Dec 2014.
- [56] J. Friedel. mettalic alloys. *Nuovo cimento suppl*, 7:287, 1958.
- [57] P. Phillips. *Advanced Solid State Physics*. Advanced Solid State Physics. Cambridge University Press, 2012.
- [58] P. Coleman. *Introduction to Many-Body Physics*. Cambridge University Press, 2015.
- [59] P. Fazekas. *Lecture Notes on Electron Correlation and Magnetism*. Series in modern condensed matter physics. World Scientific, 1999.
- [60] G. Grüner and A. Zawadowski. Semiphenomenological model for the resonances and charge neutrality in dilute magnetic alloys. *Solid State Communications*, 11(5):663 – 667, 1972.
- [61] Henrik Bruus and Karsten Flensberg. *Many-body quantum theory in condensed matter physics - an introduction*. Oxford University Press, 2004.
- [62] R Bulla, A C Hewson, and Th Pruschke. Numerical renormalization group calculations for the self-energy of the impurity anderson model. *Journal of Physics: Condensed Matter*, 10(37):8365, 1998.
- [63] A. Liebsch. Novel mott transitions in a nonisotropic two-band hubbard model. *Phys. Rev. Lett.*, 95:116402, Sep 2005.
- [64] Massimo Capone, Luca de’ Medici, and Antoine Georges. Solving the dynamical mean-field theory at very low temperatures using the lanczos exact diagonalization. *Phys. Rev. B*, 76:245116, Dec 2007.
- [65] Hiroshi Ishida and Ansgar Liebsch. Fermi-liquid, non-fermi-liquid, and mott phases in iron pnictides and cuprates. *Phys. Rev. B*, 81:054513, Feb 2010.

- [66] Philippe Nozieres. A “fermi-liquid” description of the kondo problem at low temperatures. *Journal of Low Temperature Physics*, 17(1-2):31–42, 1974.
- [67] T. A. Costi, A. C. Hewson, and V. Zlatic. Transport coefficients of the anderson model via the numerical renormalization group. *Journal of Physics: Condensed Matter*, 6(13):2519, 1994.
- [68] Ian Affleck. *The Kondo Screening Cloud*, pages 1–12. Springer Netherlands, Dordrecht, 2002.
- [69] H. O. Frota. Shape of the kondo resonance. *Phys. Rev. B*, 45:1096–1099, Jan 1992.
- [70] Richard J Warburton. Single spins in self-assembled quantum dots. *Nature materials*, 12(6):483–493, 2013.
- [71] K. Nagaoka, T. Jamneala, M. Grobis, and M. F. Crommie. Temperature dependence of a single kondo impurity. *Phys. Rev. Lett.*, 88:077205, Feb 2002.
- [72] Yong-hui Zhang, Steffen Kahle, Tobias Herden, Christophe Stroh, Marcel Mayor, Uta Schlickum, Markus Ternes, Peter Wahl, and Klaus Kern. Temperature and magnetic field dependence of a kondo system in the weak coupling regime. *Nature communications*, 4, 2013.
- [73] TA Costi, AC Hewson, and V Zlatic. Transport coefficients of the anderson model via the numerical renormalization group. *Journal of Physics: Condensed Matter*, 6(13):2519, 1994.
- [74] B. Horvatić, D. Sokcević, and V. Zlatic. Finite-temperature spectral density for the anderson model. *Phys. Rev. B*, 36:675–683, Jul 1987.
- [75] R. N. Silver, J. E. Gubernatis, D. S. Sivia, and M. Jarrell. Spectral densities of the symmetric anderson model. *Phys. Rev. Lett.*, 65:496–499, Jul 1990.
- [76] L. Merker and T. A. Costi. Numerical renormalization group calculation of impurity internal energy and specific heat of quantum impurity models. *Phys. Rev. B*, 86:075150, Aug 2012.
- [77] Hilbert v. Löhneysen, Achim Rosch, Matthias Vojta, and Peter Wölfle. Fermi-liquid instabilities at magnetic quantum phase transitions. *Rev. Mod. Phys.*, 79:1015–1075, Aug 2007.
- [78] Rok Žitko and Thomas Pruschke. Energy resolution and discretization artifacts in the numerical renormalization group. *Phys. Rev. B*, 79:085106, Feb 2009.
- [79] G. Kotliar, S. Y. Savrasov, K. Haule, V. S. Oudovenko, O. Parcollet, and C. A. Marianetti. Electronic structure calculations with dynamical mean-field theory. *Rev. Mod. Phys.*, 78:865–951, Aug 2006.
- [80] JJ Deisz, DW Hess, and JW Serene. Improved treatment of frequency sums in propagator-renormalized perturbation theories. In *Recent Progress in Many-Body Theories*, pages 433–441. Springer, 1995.
- [81] Andrew K. Mitchell, Michael Becker, and Ralf Bulla. Real-space renormalization group flow in quantum impurity systems: Local moment formation and the kondo screening cloud. *Phys. Rev. B*, 84:115120, Sep 2011.

- [82] Lorenzo De Leo and Michele Fabrizio. Spectral properties of a two-orbital anderson impurity model across a non-fermi-liquid fixed point. *Phys. Rev. B*, 69:245114, Jun 2004.
- [83] Matthias Vojta. Orbital-selective mott transitions: Heavy fermions and beyond. *Journal of Low Temperature Physics*, 161(1):203–232, 2010.
- [84] Gavin David Scott and Douglas Natelson. Kondo resonances in molecular devices. *ACS nano*, 4(7):3560–3579, 2010.
- [85] Qiushi Zhang, Guowen Kuang, Rui Pang, Xingqiang Shi, and Nian Lin. Switching molecular kondo effect via supramolecular interaction. *ACS nano*, 9(12):12521–12528, 2015.
- [86] J. Li, W.-D. Schneider, R. Berndt, and B. Delley. Kondo scattering observed at a single magnetic impurity. *Phys. Rev. Lett.*, 80:2893, 1998.
- [87] V. Madhavan, W. Chen, T. Jamneala, M. F. Crommie, and N. S. Wingreen. Tunneling into a Single Magnetic Atom: Spectroscopic Evidence of the Kondo Resonance. *Science*, 280:567, 1998.
- [88] H. C. Manoharan, C. P. Lutz, and D. M. Eigler. Quantum mirages formed by coherent projection of electronic structure. *Nature*, 403:512–515, 2000.
- [89] N. Knorr, M. A. Schneider, L. Diekhöner, P. Wahl, and K. Kern. Kondo effect of single co adatoms on cu surfaces. *Phys. Rev. Lett.*, 88:096804, 2002.
- [90] P. Wahl, L. Diekhöner, M. A. Schneider, L. Vitali, G. Wittich, and K. Kern. Kondo temperature of magnetic impurities at surfaces. *Phys. Rev. Lett.*, 93:176603, 2004.
- [91] N. Néel, J. Kröger, L. Limot, K. Palotas, W. A. Hofer, and R. Berndt. Conductance and kondo effect in a controlled single-atom contact. *Phys. Rev. Lett.*, 98:016801, 2007.
- [92] L. Vitali, R. Ohmann, S. Stepanow, P. Gambardella, K. Tao, R. Huang, V. Stepanyuk, P. Bruno, and K. Kern. Kondo effect in single atom contacts: The importance of the atomic geometry. *Phys. Rev. Lett.*, 101:216802, 2008.
- [93] B. Surer, M. Troyer, Ph. Werner, T. O. Wehling, A. M. Läuchli, A. Wilhelm, and A. I. Lichtenstein. Multiorbital kondo physics of co in cu hosts. *Phys. Rev. B*, 85:085114, Feb 2012.
- [94] D. Jacob. Towards a full ab initio theory of strong electronic correlations in nanoscale devices. *J. Phys. Condens. Mat.*, 27:245606, 2015.
- [95] P. P. Baruselli, R. Requist, A. Smogunov, M. Fabrizio, and E. Tosatti. Co adatoms on cu surfaces: Ballistic conductance and kondo temperature. *Phys. Rev. B*, 92:045119, 2015.
- [96] S. Frank and D. Jacob. Orbital signatures of fano-kondo lineshapes in stm adatom spectroscopy. *Phys. Rev. B*, 92:235127, 2015.
- [97] Jun-ichi Okamoto, Ludwig Mathey, and Rainer Härtle. Hierarchical equations of motion approach to transport through an anderson impurity coupled to interacting luttinger liquid leads. *Phys. Rev. B*, 94:235411, Dec 2016.

- [98] Axel Thielmann, Matthias H. Hettler, Jürgen König, and Gerd Schön. Shot noise in tunneling transport through molecules and quantum dots. *Phys. Rev. B*, 68:115105, Sep 2003.
- [99] JP Bergfield and Charles A Stafford. Many-body theory of electronic transport in single-molecule heterojunctions. *Physical Review B*, 79(24):245125, 2009.
- [100] Freidrich Hund. Zur deutung verwickelter spektren, insbesondere der elemente scandium bis nickel. *Zeitschrift für Physik*, 33(1):345–371, 1925.
- [101] Antoine Georges, Luca de’ Medici, and Jernej Mravlje. Strong correlations from hund’s coupling. *Annual Review of Condensed Matter Physics*, 4(1):137–178, 2013.
- [102] Ph. Nozières and A. Blandin. Kondo effect in real metals. *J. Physique*, 41:193, 1980.
- [103] N. Roch, S. Florens, T. A. Costi, W. Wernsdorfer, and F. Balestro. Observation of the underscreened kondo effect in a molecular transistor. *Phys. Rev. Lett.*, 103:197202, 2009.
- [104] J. J. Parks, A. R. Champagne, T. A. Costi, W. W. Shum, A. N. Pasupathy, E. Neuscamman, S. Flores-Torres, P. S. Cornaglia, A. A. Aligia, C. A. Balseiro, G. K.-L. Chan, H. D. Abruña, and D. C. Ralph. Mechanical control of spin states in spin-1 molecules and the underscreened kondo effect. *Science*, 328:1370, 2010.
- [105] Serge Florens, Axel Freyn, Nicolas Roch, Wolfgang Wernsdorfer, Franck Balestro, Pablo Roura-Bas, and AA Aligia. Universal transport signatures in two-electron molecular quantum dots: gate-tunable hund’s rule, underscreened kondo effect and quantum phase transitions. *Journal of Physics: Condensed Matter*, 23(24):243202, 2011.
- [106] P. Coleman and C. Pépin. Singular fermi liquid behavior in the underscreened kondo model. *Phys. Rev. B*, 68:220405, Dec 2003.

Eidesstattliche Erklärung

Hiermit erkläre ich, dass ich meine Dissertation selbstständig und ohne fremde Hilfe verfasst und keine anderen als die von mir angegebenen Quellen und Hilfsmittel zur Erstellung meiner Dissertation verwendet habe. Den benutzten Werken wörtlich oder inhaltlich entnommene Stellen sind als solche gekennzeichnet.

Ort, Datum _____

Sareh Motahari

Acknowledgments

The work presented in this thesis would not have been possible without the guidance and the help of several individuals who in one way or another contributed and extended their valuable assistance in the preparation and completion of this study. I take this opportunity to extend my sincere gratitude and appreciation to all those who made this Ph.D. thesis possible.

First and foremost, I would like to extend my sincere gratitude to my supervisor, Dr. David Jacob for his dedicated help, advice, inspiration, encouragement and continuous support, throughout my Ph.D. The discussions on physical problems were always enjoyable and enlightening. I also would like to thank Prof. Dr. Eberhard Gross for providing a friendly and scientifically enriching atmosphere in the theory department of the Max Planck institute and also his support from the beginning to the end of my Ph.D. I am extremely grateful to my colleague, Dr. Ryan Tyler Requist for the useful and enjoyable discussions. I feel grateful to all my colleagues in the theory department in MPI for sharing a lot of unforgettable memories during last five years. I would like to further thank my officemate, Sebastian for his continuous help and Ina for her kind and valuable tips.

Finally, my deep and sincere gratitude to my family for their continuous and unparalleled love, help and support. I am forever indebted to my parents, for their constant encouragement and permanent support throughout my studies. They selflessly encouraged me to explore new directions in life and seek my own destiny. I am also grateful to my sisters for always being there for me as good friends. But most importantly, I am forever thankful to my husband, Ahmad for his unfailing love, support and patience and also my son, Kiarad for his patience and understanding.

Curriculum Vitae

Personal Information

Name Sareh
Last Name Motahari
Date of birth 11 June 1982
Place of birth Saveh, Iran

Education

10/2012 – Now **Max-Planck-Institut für Mikrostrukturphysik and Martin Luther Universität Halle-Wittenberg**, Halle(Saale), Germany, Ph.D. candidate in Physics

- Ph.D. Dissertation Title: Kondo physics and thermodynamics of the Anderson impurity model by distributional exact diagonalization
- Supervisors: Dr. David Jacob, Prof. Dr. Eberhard Gross

10/2008 – 10/2010 **Shahid Rajaei Teacher Training University(SRTTU)**, Tehran, Iran, Master of Science Physics

- GPA: 17.58/20.00
- Titel of Master Thesis: Properties of Helium-3 in bounded geometries by variational method
- Supervisors: Prof. Dr. Majid Modarres and Dr. Mehdi Neekamal

10/2001 – 07/2005 **K. N. Toosi University of Technology**, Tehran, Iran, Bachelor of Science Physics

- GPA: 15.41/20.00

List of Publications

1. Kondo physics of the Anderson impurity model by Distributional Exact Diagonalization, *Physical Review B* 94 (2016) 235133.
2. The helium 3 droplet energy and density profile calculations using the (E) LOCV formalism, *Journal of Computational and Theoretical Nanoscience*, Vol. 10 (2013) 1278.
3. The (E) LOCV study of liquid ^3He atoms in a nanometer tube, *Journal of Computational and Theoretical Nanoscience*, Vol. 10 (2013) 1080.
4. The ground state energy of ^3He droplet in the LOCV framework, *Iranian Journal of Physics Research*, Vol. 12 (2012) 16.
5. Van der Waals energy surface of carbon nanotubes sheet, *Solid State Communications*, Vol. 152(2012) 225.